INVESTIGATION OF THE UNDERLYING PHENOMENA OF PRECIPITATION IN

SUPERCRITICAL ANTISOLVENT PROCESSES

Except where reference is made to the work of others, the work described in this dissertation is my own or was done in collaboration with my advisory committee. This dissertation does not include proprietary or classified information.

_____
Daniel Lawrence Obrzut

Certificate of Approval:

_____   _____
Steve R. Duke, Co-Chair   Christopher B. Roberts, Co-Chair
Associate Professor   Uthlaut Professor
Chemical Engineering   Chemical Engineering

_____   _____
Ram B. Gupta   Jeffrey Fergus
Alumni Professor   Associate Professor
Chemical Engineering   Materials Engineering

_____
George T. Flowers
Interim Dean
Graduate School

INVESTIGATION OF THE UNDERLYING PHENOMENA OF PRECIPITATION IN

SUPERCRITICAL ANTISOLVENT PROCESSES

Daniel Lawrence Obrzut

A Dissertation

Submitted to

the Graduate Faculty of

Auburn University

in Partial Fulfillment of the

Requirements for the

Degree of Doctor

of Philosophy

Auburn, Alabama
August 9, 2008

INVESTIGATION OF THE UNDERLYING PHENOMENA OF PRECIPITATION IN

SUPERCRITICAL ANTISOLVENT PROCESSES

Daniel Lawrence Obrzut

_____
Signature of Author

_____
Date of Graduation

VITA

Daniel Lawrence Obrzut was born just outside of Chicago in Evergreen Park, IL to Richard Francis Obrzut and Nancy Ellen Obrzut. In 1993 he graduated from St. Mary Nativity Elementary School. He graduated with honors from Lockport Township High School in 1997. Daniel graduated with a Bachelors of Science majoring in chemical engineering from Illinois Institute of Technology in 2001. He graduated with a Masters of Science from Auburn University in 2003 under the direction of Dr. James Guin. The title of his thesis is "Modifying SAPO-34 molecular sieves to improve the performance of the methanol to olefins reaction and explore alternate applications". He returned to Auburn University in January of 2004 to pursue his Doctorate of Philosophy under the direction of Dr. Steve R. Duke and Dr. Christopher B. Roberts.

DISSERTATION ABSTRACT

INVESTIGATION OF THE UNDERLYING PHENOMENA OF PRECIPITATION IN

SUPERCRITICAL ANTISOLVENT PROCESSES

Daniel Lawrence Obrzut

Doctor of Philosophy, August 9, 2008
(M.S., Auburn University, 2003)
(B.S., Illinois Institute of Technology, 2001)

213 Typed Pages

Directed by Steve R. Duke and Christopher B. Roberts

There is significant industrial interest in the ability to effectively produce organic and polymeric microparticles of controllable size and size distribution for numerous applications including certain pharmaceutical formulations. One method to produce microparticles is the supercritical antisolvent precipitation process. This method is performed by spraying a solution through a nozzle into a supercritical antisolvent, typically carbon dioxide. The solution consists of a solute which is insoluble in the antisolvent and an organic solvent which is soluble in the antisolvent. The organic solvent and the antisolvent mix as the solution is sprayed into the supercritical antisolvent. As the concentration of antisolvent increases the affinity of the solute for the solvent/antisolvent mixture decreases which leads to supersaturation and precipitation of the solute.

Studies were performed to probe the underlying phenomena of the supercritical antisolvent (SAS) precipitation process. To study the relationship between operating conditions, spray characteristics, and the resulting particles, sprays of solutions into supercritical carbon dioxide were characterized by visualizing the sprays at various distances from the nozzle outlet to measure jet break up lengths and droplet diameters using a high magnification visualization setup. A 1 wt% solution of poly(L-lactic) acid in methylene chloride was sprayed into carbon dioxide to study the effect of pressure, temperature, and density. Despite very different spray characteristics, performing the SAS precipitation process on poly(L-lactic) acid produced particles within a similar size range at most conditions. The effect of the affinity of the solute for the solvent on the SAS precipitation process was evaluated by processing polyvinyl pyrrolidone, polymethyl methacrylate, and poly(methyl methacrylate-vinyl pyrrolidone) which have different solubilities in the solvent ethanol. The different polymer solutes had a negligible effect on the spray characteristics, so the diffusion of ethanol and carbon dioxide was similar regardless of the solute used at a particular operating condition. The smallest polymer particles were obtained when operating near the transition from atomization to break up as gaseous plume. By changing the affinity between the polymer solute and the organic solvent, the tendency to form microballoons was altered. Also, a new particle precipitation process which utilizes the tendency for buoyant forces to induce flow in variable density fluids and the relation between supercritical fluid density and saturation concentration of a solute in the fluid was developed. This thermosyphon process was successfully demonstrated when naphthalene dissolved in a cold zone, was transported by the buoyant flow of carbon dioxide, and precipitated in a hot zone.

ACKNOWLEDGEMENTS

I would like to thank many individuals who have provided assistance throughout my doctoral research. The guidance that Dr. Steve R. Duke and Dr. Christopher B. Roberts provided has led me to a greater understanding of imaging scientific phenomena, fluid dynamics, and supercritical fluid. The research groups of Dr. Duke and Dr. Roberts have assisted me by providing input on innumerable technical and conceptual issues. I would also like to thank Dr. Jeffrey Fergus, Dr. Ram Gupta, Dr. Mario Eden, and Dr. William Ravis for assisting with my defense.

On a personal note, I would like to send my appreciation to the many friends that I have made while pursuing graduate degrees. Their friendship has made my time at Auburn memorable. Finally, I would like to thank my family for their constant and unwavering support. At times when my studies were difficult, I knew that I could look to them for encouragement.

The bibliography was prepared in the style of The Journal of Supercritical Fluids.

Microsoft Word, Microsoft Excel, and Open Office were used to prepare this manuscript.

TABLE OF CONTENTS

LIST OF FIGURES

LIST OF TABLES

1. Introduction

The micronization of active pharmaceutical ingredients (API) is an important step in the production of pharmaceutical products. Micronization can be used to improve and control several characteristics of drug particles including bioavailability and possible delivery methods. In many cases, the API is sparingly soluble in water which results in a low bioavailability. Decreasing the particle size of the API may decrease the time necessary for it to dissolve in the body and, therefore, increase the bioavailability (Liversidge and Cundy 1995). The size of the API particles can also be used to control the delivery of pharmaceutics to the body, for example through the size selection inherent to the lungs (Sinko 2006).

Several methods have been developed to obtain microparticles of active pharmaceutical ingredients. These methods can be grouped into either comminution (size reduction) or controlled growth (Rasenack and Müller 2004). Methods of mechanical comminution or milling reduce the size of large API particles through pressure, attrition, impact, or shearing. These techniques include jet milling, ball milling, and high-pressure homogenization. Common disadvantages of these milling methods are a limited control of the resulting particle characteristics and a chemically unstable product. Controlled growth to form API microparticles is carried out through nucleation into small particles and prevention of particle growth. These techniques include spray drying, supersaturation with a stabilizing agent, and supercritical fluid based methods.

Using supercritical fluids to create microparticles has been an active area of research in recent years. These supercritical fluid processes have been developed to create microparticles, often pharmaceuticals, with limited separation steps and without the need for surfactants. The most common supercritical fluid used in these processes is carbon dioxide which has a critical temperature of 31.1°C and a critical pressure of 73.8 bar. Carbon dioxide is used either as an antisolvent or solvent for the solute that will be made into microparticles. When CO_2 is an antisolvent, an organic solvent such as methylene chloride or ethanol is used to dissolve the solute. By mixing the organic solvent and CO_2, the solute becomes supersaturated and precipitates. The supercritical antisolvent (SAS) precipitation process and derivatives of it utilize this concept by spraying a solution of organic solvent and solute through a nozzle into supercritical carbon dioxide (Dixon et al. 1993). When carbon dioxide is used as a solvent, the solvent strength of carbon dioxide is adjusted by changing the pressure and/or temperature of the CO_2/solute solution. In rapid expansion of a supercritical solvent (RESS), supercritical carbon dioxide dissolves a solute, and precipitation is induced by expanding the carbon dioxide to atmospheric conditions by spraying through a nozzle (Matson et al. 1987). These and similar processes have been performed successfully on many solutes at various operating conditions to obtain micro- and nano-particles. However, the underlying phenomena of the processes are not fully understood which results in poor control of the particle formation. The work presented in this dissertation provides a more in-depth understanding of the SAS precipitation process.

2. Background

The Supercritical Antisolvent Precipitation Process

The supercritical antisolvent (SAS) precipitation process is a spray process used to produce small particles (Dixon et al. 1993). The SAS precipitation process involves three distinct materials: antisolvent, solute, and solvent. To perform the SAS precipitation process, a solution of the solvent and solute is sprayed into compressed antisolvent through a nozzle with a small diameter, typically 50 to 200 microns. For a continuous process the antisolvent is pumped into the vessel concurrently with the solution while there is a constant outflow of fluid. Particles are collected at the exit of the vessel using a filter which is at the same process conditions as the bulk fluid. The antisolvent is typically supercritical carbon dioxide due to the tunability of its strength as a solvent, relatively mild supercritical conditions, and approval for use by the FDA (Beckman 2004). The solute, which will precipitate as particles, is insoluble in supercritical carbon dioxide and may be one or several of a variety of substances including pharmaceuticals (Randolph et al. 1993), polymers (Mawson et al. 1997), proteins (Yeo et al. 1993), and dyes (Wu et al. 2005). The solvent must dissolve the solute and be miscible with supercritical carbon dioxide. Solvents which have been used in the SAS precipitation process include toluene, acetone, methylene chloride, ethanol, dimethyl sulfoxide (DMSO), and dimethyl formamide (DMF). Several important phenomena of SAS have been studied, but the process is yet to be fully understood.

Key Studies in the Development of the SAS Precipitation Process

The first paper to report spraying a solution into a compressed fluid antisolvent to obtain microparticles was Dixon et al. (1993). A solution of polystyrene and toluene was sprayed into carbon dioxide at subcritical and supercritical conditions. Polystyrene microparticles were formed when the initial solution had a low concentration of polystyrene. High concentrations of polystyrene in the initial solution resulted in precipitation as polystyrene fibers instead of particles. An increase in particle size was observed as the temperature was increased from 10°C to 40°C at 0.86 g/mL. This set of experiments included operating conditions above and below the critical point of carbon dioxide. The increase in particle size was suggested to depend on the size of droplets breaking off the solution jet. This work showed microparticles can be formed in the SAS spray process by having a low solute concentration in the solution.

Poly(L-lactic) acid (PLA) is an important polymer for pharmaceutical and industrial purposes that can be processed using SAS. Randolph et al. (1993) used the SAS precipitation process to form microparticles of PLA with the intention of developing particles for timed release delivery of pharmaceuticals. At conditions slightly above the critical point of carbon dioxide, spherical PLA microparticles were obtained. Operating at 304 K and pressures of 75.8 bar, 82.7 bar, and 96.5 bar, the average size of collected particles was seen to increase from 0.61 μm to 1.4 μm. It was speculated that the change in particle size with pressure can be related to the rate of mass transfer rather than the initial size of droplets.

To understand the mechanisms of the SAS precipitation process Lengsfeld et al. (2000) studied the jet break up of solutions and organic solvents sprayed into carbon

dioxide. They estimated that at 85 bar and 308 K the surface tension between a

methylene chloride jet and carbon dioxide is near 0.01 mN/m at 1 μm from the nozzle

outlet at a jet velocity 10 cm/s. If the characteristic jet break up length was shorter than 1

μm, the jet was predicted and shown to break up into a gas-like plume instead of

atomizing into droplets due to the low surface tension. Particles formed in the core of the

gas-like plume were predicted to be larger than particles formed in the carbon dioxide

rich perimeter because it takes longer for carbon dioxide to diffuse into the core of the

gas-like plume. When the jet breaks up as a gas-like plume, the size of particles was

predicted to be controlled by diffusion rather than droplet characteristics.

Dukhin et al. (2003) visualized the spray of ethanol into carbon dioxide and

related the behavior to dynamic interfacial tension. The interfacial tension, γ, was

estimated through the Parachor parameter equation

$$\gamma^{1/4} = \sum_i P_i \left(C^L x_i - C^V y_i \right) \tag{2.1}$$

where P_i is the Parachor parameter of species i, C^L is the molar density of the liquid

phase, C^V is the molar density of the gas phase, x_i and y_i are the mole fractions of species

i in the liquid and gas phases, respectively. The surface tension was calculated for each

condition assuming equilibrium and at time zero where the liquid and vapor were pure

phases. The jet breakup mechanism was also related to the mixture critical point. Below

and slightly above the mixture critical point, the jet was observed to break up through the

traditional jet break up regimes (e.g. atomization). Slightly above the mixture critical

point the jet break up regime was attributed to a dynamic interfacial surface tension.

Thus the jet break up time was shorter than the diffusion time. Well above the mixture

critical point, the jet broke up as a gas-like plume. At these conditions while diffusion

was not complete before the jet broke up, it was sufficient to reduce the surface tension to zero.

Solvent Solubility

Gokhale et al. (2007) performed SAS on polyvinylpyrrolidone (PVP) to study the effect of dissolving a solute in a mixture of a good solvent, methylene chloride, and a poor solvent, acetone, on the resulting particle size. Imaging the spray of pure solvent, acetone/methylene chloride mixture, and PVP/acetone/methylene chloride solution into carbon dioxide demonstrated that the jet break up transitions from dripping to atomization to break up as a gas-like plume. This transition occurred by decreasing the nozzle diameter and increasing the solution flow rate. In a series of SAS experiments with several solutions of methylene chloride, acetone, and PVP at various concentrations, the average particle size of PVP decreased as the acetone concentration in the original solution was increased. As the jet break up transitioned from dripping to atomization, the dependence of the average particle size on the acetone concentration in the sprayed solution decreased. PVP with molecular weights of 1,300,000 and 360,000 were studied at 35°C. The 1,300,000 molecular weight particles were slightly larger than the 360,000 molecular weight particles during dripping experiments. The smallest particle distribution was obtained just above the mixture critical point.

Ho Kim and Shing (2008) micronized ipratropium bromide via the SAS precipitation process to produce inhalable drug particles. Three solvents for ipratropium bromide were studied: ethanol, ethanol/acetone, and dimethyl formamide (DMF). Ethanol resulted in 4-15 μm "very irregular, flaky particles." Acetone was added to

ethanol to decrease the solubility of ipratropium bromide in the solution. Performing

SAS with ipratropium bromide/ethanol/acetone solutions resulted in smaller, more

spherical particles than using pure ethanol as the solvent, but the particles were too large

for inhalation. Using DMF, the particle size distribution ranged from 1 μm to 5 μm

which is ideal for inhalation. In further studies, Ho Kim et al. (2008) performed the SAS

precipitation process on terbutaline sulphate and ipratropium bromide with albumin.

Adding albumin resulted in significantly more uniform spherical particles. By decreasing

the solubility of the solute in the solution, a greater supersaturation was reached in the

precipitation chamber which resulted in smaller particles.

Theoretical Studies

One of the earliest models of SAS was developed by Lora, Bertucco, and Kikic

(Lora et al. 2000). The system was modeled as mass transfer between a droplet and the

bulk fluid then the model was expanded to a full section of the spray. This model

assumed that the mass transfer into the droplet was driven by molecular diffusion and the

core of the droplet was fully mixed. The solute was assumed to precipitate when the

solid state fugacity was lower than the liquid state fugacity. The mass transfer of the

process was modeled by the following equations:

$$N_{AL} = x_A^e(N_{AL} + N_{BL}) - k_L(x_A^e - x_A) = y_A^e(N_{AG} + N_{BG}) - k_G(y_A - y_A^e) = N_{AG} \quad (2.2)$$

$$N_{BL} = x_B^e(N_{AL} + N_{BL}) + k_L(x_B - x_B^e) = y_B^e(N_{AG} + N_{BG}) - k_G(y_B^e - y_B) = N_{BG} \quad (2.3)$$

where N is molar flux, x is mole fraction in the droplet, y is mole fraction in the bulk

fluid, k is mass transfer coefficient, L represents the liquid droplet, G represents the bulk

gaseous fluid, A represents the solvent, and B represents the antisolvent. This model was

evaluated by examining a carbon dioxide-toluene system at 315.15 K and 83.4 bar with naphthalene and phenanthrene as solutes. Several conclusions were drawn from this study. Since carbon dioxide was much more soluble in the solvent than the solvent was in the bulk phase, the carbon dioxide was predicted to rapidly diffuse into the droplet until equilibrium was reached. Increasing the initial droplet diameter decreased the time needed to reach equilibrium, but it decreased the time for a solute to be supersaturated.

Another key SAS model dealing with mass transfer between the droplets and bulk fluid in subcritical conditions was published by Werling and Debenedetti (1999) and was later extended to miscible conditions (Werling and Debenedetti 2000). This model examined the mass flux between a single droplet of organic solvent and a bulk fluid of carbon dioxide antisolvent. Mixing inside the droplet was assumed to be due to convective motion. The model was set up by assuming the flux of carbon dioxide follows Fick's Law and the diffusion coefficient was related to the chemical potential gradient. The CO_2 mole fraction profile inside the droplet was represented by

$$\frac{d}{dt}(\rho_L x_A) + \nabla \bullet (-\rho_L D_L' \nabla x_A + x_A N_L) = 0. \tag{2.4}$$

Interfacial flux calculations used the assumption that the phase interface was at equilibrium conditions. For mixture supercritical conditions (Werling and Debenedetti 2000), there is no phase interface, so the mass transfer was defined in one equation. To define the concentration profile, only one mass balance and the continuity equation were necessary. The carbon dioxide initially dominated the mass transfer by diffusing into the droplet. The interfacial flux approached zero when the rate of mass transfer into the droplet approached the rate of mass transfer out of the droplet. Then, the rate of mass transfer out of the droplet became the controlling mass transfer. Raising the pressure

increased the maximum size of the droplet but decreased the time for the droplet to be indistinguishable from the bulk fluid. The lifetime of the droplet reached a maximum slightly above the mixture critical temperature. When the SAS precipitation process was operated above the mixture critical point, droplets were predicted to shrink when the solvent density was below the bulk fluid density and swell when the density was greater in the droplet.

Mukhopadhyay and Dalvi (2004) introduced a nonisothermal model of the SAS precipitation process. A droplet was modeled as having a well mixed core surrounded by a film at the phase interface. Mass transfer between the droplet core and the bulk fluid occurred at the interface which is at equilibrium. Heat transfer into the droplet was considered to occur from the evaporation of solvent and dissolution of carbon dioxide at the interface. The driving force of carbon dioxide transport was the concentration of carbon dioxide in the core of the droplet compared to the equilibrium interface concentration. Heat transfer was added in this model to calculate how heat produced by dissolution and evaporation affects the supersaturation conditions. The temperature of the droplet was predicted to initially reduce by 1 to 3 K before stabilizing when operating at subcritical conditions. The proximity of operating conditions to the mixture critical point was the determining factor of the change in droplet diameter, shrinking or swelling after initial swelling.

Another model of SAS was pursued by Pérez de Diego et al. (2006) to study the droplet size and evaporation time. Mass transfer was modeled using the Maxwell-Stefan equation by a finite-difference approximation instead of diffusion by Fick's Law. The droplets were assumed to follow a core-shell model with equilibrium at the interface

assumed. Increasing the carbon dioxide to solvent ratio and decreasing the initial droplet diameter were shown to decrease the droplet lifetime. The droplet evaporation time was shown to increase when the carbon dioxide had a high solubility in the solvent droplet or when the bulk fluid had a very low density.

Chávez et al. (2003) modeled jet break up, mass transfer, and nucleation to determine the dominant process based on analysis of the time scales for each to occur. The jet break up time was calculated for Weber numbers ranging from 1 to 40 at different temperatures. The maximum jet break up time was on the order of 10^{-3}s. The time for diffusion to occur was 2 orders of magnitude larger than jet breakup time. Nucleation was modeled using classical nucleation theory. Diffusion time was usually several orders of magnitude larger than the nucleation time. These calculations showed that a diffusion-limited system may result from a low desolvation energy, low interfacial tension, and large supersaturation levels. A nucleation-limited system may result from small droplets, high interfacial tension, high desolvation energy, low solute concentration, and low supersaturation levels.

A model of the solvent and solute concentration throughout a single phase spray was developed by Martín and Cocero (2004). This model considered the spray of solution as a gas-like plume instead of droplets to improve the understanding of SAS in a supercritical regime. One of the goals of this work was to predict what size particles may form depending on their location in the spray. The size of particles was modeled as a function of nucleation, coagulation, and condensation. This method of calculation predicted that particle size depended on the location within the jet where nucleation

occurs. The results from this model suggest that modifying temperature and pressure to induce supersaturation faster will produce smaller particles.

Microballoon Formation

Further work on polystyrene studied the effect of a two phase system on the particle size and morphology (Dixon et al. 1994). By spraying a polystyrene and toluene solution into subcritical carbon dioxide, microspheres and microballoons were formed. It was proposed that droplets form in the gas phase carbon dioxide then dry and vitrify in the liquid phase when microballoons form. The thickness of the shell increased and interior core size decreased with increasing concentration of polystyrene in the solution until porous microspheres were formed instead of microballoons. It was proposed that the formation of microballoons is due to the bursting of pore walls as solvent is replaced with carbon dioxide. As the interior pore walls burst, the polystyrene concentration near the exterior of the particles increases. At higher concentration of polystyrene, thicker and thus stronger pore walls which will not burst are formed. This study showed that microparticles can be formed at subcritical conditions near the critical point, and the solute concentration in the initial solution can have a large effect on the microballoon morphology.

Reverchon et al. (2003) studied the effect of operating conditions on processing yttrium acetate (YAc) in solution with dimethyl sulfoxide (DMSO) using the SAS precipitation process. To study phase behavior, CO_2 and DMSO were sprayed continuously into a vessel at a CO_2 mole fraction of 0.98. At increasing temperatures a higher pressure was necessary to reach the mixture critical point and, therefore, the

transition from atomization to break up as a gas-like plume. When this experiment was performed with a 1.38 wt% YAc/DMSO solution, the mixture critical point was the same, but as the concentration of YAc increased (4.5 wt%) the pressure required to reach the mixture critical point also increased. Increasing the diameter of the nozzle was shown to result in a small increase in the particle size. The particle size was also shown to increase with increasing concentration of YAc in solution. The effect of phase behavior on particle size and morphology was studied by increasing the pressure at several temperatures to induce a transition from a two phase subcritical system to a one phase supercritical system. In the subcritical system, nano-scale particles were shown to slightly decrease in size with increasing pressure. Near the transition from a two phase subcritical system to a one phase supercritical system, small particles coalesced to form large microballoon structures. When a one phase supercritical system was reached, smaller particle were obtained than those collected from a two phase subcritical system. This study showed that the relation between the operating conditions and the mixture critical point is very important when performing the SAS precipitation process.

De Marco and Reverchon (2008) micronized α- and β-cyclodextrins using the SAS precipitation process. The cyclodextrins were precipitated from dimethyl sulfoxide (DMSO) solutions at solution concentration of 5-200 mg/mL and operating conditions of 40-60°C and 90-180 bar. The resulting particles ranged from submicron particles to large microballoons. In the transition region between subcritical and supercritical conditions, solutions with small cyclodextrins concentrations produced microparticles while large concentrations produced microballoons. This change in particle morphology may be due to a slight change in the mixture critical point due to the presence of the solute.

Poly(L-lactic) Acid

Carretier et al. (2003) examined the effect on flow rate of 1 wt% PLA in methylene chloride solution on particle production in SAS. The experiments were performed at 100 bar, 308 K, and solution flow rates of 0.25, 0.5, 0.75, 1, 1.5, and 3 mL/min through a 150 μm I.D. capillary tube. When the solution flow rate was 0.25 and 0.5 mL/min, fibers and nearly spherical particles were collected. At faster solution flow rates spherical particles with increasing diameters, 1 to 3 μm, were produced. A decreasing jet break up length was observed for solution flow rates from 0.25 to 1 mL/min. The fibers collected at 0.25 and 0.5 mL/min were attributed to precipitation occurring before the jet break up.

Mawson et al. (1997) looked at various methods to control the particle production during SAS for different solute/solvent systems. In this study SAS was performed with and without CO_2 coflow to make microparticles from polystyrene, poly(L-lactic) acid, insulin, and polycarbonate/poly(styrene-co-acrylonitrile). Flow rates, temperature, pressure, and solute concentration were varied to study the controlling factors in SAS. The studied conditions allowed for the system to be single phase at equilibrium. When comparing a coflow and a standard, non-coflow nozzle, droplets and collected particles were seen to be larger with the coflow nozzle. PLA particles obtained using a standard nozzle were less agglomerated than polystyrene particles since PLA is plasticized by CO_2 to a lesser degree than polystyrene. Using the coflow nozzle, the particle size distribution exhibited a bimodal distribution, which may be due to particles precipitating inside as well as outside of droplets. Flocculation and agglomeration of particles was attributed to slow drying of particles. Using the coflow nozzle reduced the level of flocculation and

agglomeration possibly due to faster drying of particles. By performing SAS at temperatures below the critical point of carbon dioxide, the effect of density was explored. At increasing density, smaller particles were produced which was attributed to atomization of the jet into smaller droplets. A decrease in particle size was also observed by using a poorer solvent for a selected solute.

Vega-Gonzalez et al. (2008) performed the SAS precipitation process on polymer blends to produce fibrous networks for tissue engineering. The polymers processed in this study were poly(L-lactic acid) and polymethyl methacrylate. Blends of polymethyl methacrylate and polycaprolactone were also processed. By performing SAS with a highly concentrated solution of these polymers and blends, fibrous networks of polymer microparticles were formed rather than individual particles. These fibers have a large surface area and may be useful as solvent-free fibrous scaffolds.

Additional Experimental Studies

Adami et al. (2008) utilized the SAS precipitation process to micronize nalmefene hydrochloride. Experiments were performed with a 1.9 wt% nalmefene hydrochloride in ethanol solution being sprayed into carbon dioxide at 120-150 bar and 40-80°C on laboratory and pilot plant scales. Nalmefene hydrochloride particles produced were in the size range of 0.3-5.7 μm using the laboratory scale setup. At similar operating conditions on the pilot plant scale, particles were obtained in the range of 0.9-12.2 μm. The crystallinity of the particles increased with temperature possibly due to temperature dependent crystallization kinetics. Interestingly at 80°C, 10°C above any laboratory scale experiments, and 130 bar, microballoons of the nalmefene hydrochloride were formed.

From VLE data it was shown that at this operating condition the system may have been subcritical.

Reverchon et al. (2002) created microparticles of rifampicin, an antibiotic used to treat tuberculosis, using the SAS precipitation process. A solution of rifampicin and dimethyl sulfoxide (DMSO) was sprayed into carbon dioxide at 40°C and pressures of 90-180 bar. At and above 120 bar networks of 0.4 to 1 μm microparticles were obtained. Operating conditions below 120 bar resulted in microparticles with mean diameters of 2.5 to 5 μm. Increasing the solute concentration in the solution caused an increase in the mean diameter of the collected particles.

The micronization of insulin was performed using the SAS precipitation process by Yeo et al. (1993). Processing of insulin was undertaken since SAS would have several advantages over other methods to make microparticles of proteins. Spray drying and milling can denature proteins. Fluid energy grinding can electrostatically charge particles. Lypholization gives a broad particle size distribution and is difficult to predict the results for a variety of proteins. Controlled precipitation from aqueous processes uses harmful organic solvents which need to be removed in an extra step, and the particle size is difficult to control in this process. Using a solution of insulin and DMSO, chemically active insulin microparticles with a small size distribution were obtained through the SAS precipitation process. Micronizing proteins in this manner did not result in protein denaturing while still providing desired particle characteristics.

Wu et al. (2005) precipitated nanoparticles of pigment red 177 through the SAS precipitation process. A solution of pigment red 177 and DMSO was sprayed into carbon dioxide at various supercritical conditions. Operating conditions included temperatures

from 308.15 K to 338.15 K and pressures from 80 bar to 250 bar. A series of experiments with increasing nozzle diameter resulted in an increase in particle size at a fixed volumetric flow rate. Increasing the concentration of pigment red 177 in the initial solution also resulted in an increase of particle size. The smallest particle size from SAS was obtained by processing red 177 in the supercritical phase.

Visualization of the Solution Spray

Bell et al. (2005) developed an imaging system to obtain in situ images of the SAS precipitation process. High magnification visualizations of solutions being sprayed into supercritical carbon dioxide were obtained at several distances from the nozzle outlet. Solutions included pure acetone, pure methylene chloride, 1 wt% poly(L-lactic) acid in methylene chloride, saturated poly(L-lactic) acid in methylene chloride, and 1 wt% budesonide in methylene chloride. The visualization technique was used to obtain images of the jet break up length, the distance from the nozzle outlet where the exit stream is no longer a straight jet, and the size of droplets at various distances from the nozzle outlet. Distinct differences of the average droplet diameter were observed at different distances from the nozzle outlet. The visualization system developed by Stephens (2003) was used in the studies presented in this dissertation.

Robustness of Operating Conditions

Several studies have shown that it is difficult to alter characteristics of particles produced in SAS by altering the operating conditions. Bleich et al. (1994) used the aerosol solvent extraction system (ASES), another name for SAS, to make microparticles

of PLA and hyoscine butylbromide. Pressure, temperature, and carbon dioxide density were varied to alter the particle characteristics. Operating conditions above the critical point of carbon dioxide were chosen. Pressure and carbon dioxide density did not appear to have a large effect on the particle size. Increasing temperature was shown to increase the size of collected particles.

Griffith et al. (1999) looked at making nylon into microparticles through SAS. The nylon collected from carpet recycling was dissolved into formic acid at 2.31 wt% and 0.63 wt%. Particles were formed by spraying these solutions into carbon dioxide at 40°C and pressures ranging from 84 bar to 125 bar. The process conditions were observed to have little influence on the particle size and morphology.

Further research into nylon, specifically nylon 6/6, was reported by Park et al. (2002). Again, a solution of nylon and formic acid was sprayed into carbon dioxide. The effect of the concentration of solute in the solvent was examined in this study. At low concentrations of the nylon, nozzle diameter and the solution flow rate were observed to have no discernable effect on the produced particles. At high concentrations of nylon in the solution, the morphology of the precipitant was observed to change from microparticles to fibers. This study reinforces the concept that operating conditions have little effect on the produced particles when performing SAS above the mixture critical point.

Similar Processes

There are several modifications which have been made to the SAS precipitation process to alter the collected particles. Variations of the supercritical antisolvent

precipitation process include SAS with coflow, SAS with enhanced mass transfer (SAS-EM) , solution-enhanced dispersion by supercritical fluids (SEDS), and atomized rapid injection for solvent extraction (ARISE). These variations were developed to increase control of the resulting particle size and morphology.

SAS with coflow is the steady-state equivalent of the supercritical antisolvent precipitation process. This process allows for two flow rates to be changed: carbon dioxide flow rate and solution flow rate. Due to the change of jet break up related with a coflow jet, the droplet morphology is also altered. Liquid is more likely to come off in sheets or "splinters" rather than drops (Mawson et al. 1997). SAS with coflow has been used to produce many types of particles including budesonide and poly(L-lactic) acid particles (Martin et al. 2002).

Supercritical antisolvent precipitation with enhanced mass transfer (SAS-EM) uses ultrasound to produce smaller droplets and, therefore, smaller particles. A titanium horn delivers constant-amplitude vibrations near the nozzle tip. The ultrasonic vibration causes a rapid mixing of the solution and antisolvent. The jet also breaks up into smaller initial droplets. When compared to SAS, the particle size is greatly reduced. Tetracycline nanoparticles have been produced with an average diameter down to 125 nm (Chattopadhyay and Gupta 2001).

Yeng Lee et al. (2008) performed SAS-EM on co-solutes of paclitaxel and poly(L-lactic acid) to improve the dissolution in water and sustained release of paclitaxel. By performing SAS-EM, submicron paclitaxel/poly(L-lactic acid) particles were obtained. *In vitro* studies in phosphate buffered saline were performed on the resulting paclitaxel/poly(L-lactic acid) particles. In these studies, paclitaxel was released within 1

month at drug loading up to 3%. At higher loadings about half the drug was released after one month, which may be due to the presence of paclitaxel crystals within the polymer.

Solution-enhanced dispersion by supercritical fluids (SEDS) is performed by having a premixing section in the nozzle. This variation involves premixing of carbon dioxide and the solution before spraying into the bulk carbon dioxide. Adding CO_2 decreases the rate at which the droplets are supersaturated by decreasing the amount of CO_2 which needs to diffuse. By altering the time after spraying for the droplet to be saturated, the particle morphology can be controlled (Shekunov et al. 2001). Further research has shown that by using a length of pipe as the premixing section, particle sizes scale with the pipe length (Chang et al. 2005). These processes alter the SAS precipitation process to optimize particle characteristics.

Atomized rapid injection for solvent extraction (ARISE) is a method similar to the SAS precipitation process (Sih and Foster 2007). In this method the solution is mixed with the carbon dioxide as rapidly as possible. Initially there are two chambers which are filled with either CO_2 or the solution. A piece of tubing and a valve connects the two chambers. To operate the process the valve is opened and an inert gas forces the solution to rapidly transfer to the CO_2 filled chamber. The solute is then rapidly supersaturated and precipitates as microparticles.

Nucleation Theory

A basic comprehension of classical nucleation theory is necessary to understand the SAS precipitation process. Nucleation occurs when a solute becomes supersaturated

(Randolph and Larson 1988). Mathematical expressions define supersaturation by comparing the solute concentration to its saturation concentration in several ways including

$$\Delta c = c - c^*$$ (2.5)

$$S = \frac{c}{c^*}$$ (2.6)

$$\gamma = \frac{\Delta c}{c} = S - 1$$ (2.7)

where c is solute concentration, c^* is the saturated solute concentration, and S and γ represent supersaturation (Mullin 2004). When Δc is positive, S is greater than one, and γ is positive, the system is supersaturated. It is important to note that c^* is dependent on the temperature, pressure, and composition of the solvent. Typically supersaturation can be induced by decreasing temperature, increasing the concentration of an antisolvent, or increasing the concentration of the solute.

A solution is supersaturated when the Gibbs free energy of the solute is lower in the solid phase than in solution. The change in free energy due to the precipitation of a nucleus of a particular size is represented by

$$\Delta G = \Delta G_s + \Delta G_V = 4 * \pi * r^2 * \sigma + \frac{4}{3} * \pi * r^3 * \Delta G_v$$ (2.8)

where ΔG_s is the free energy to form the particle surface, ΔG_V is the free energy change due to the solute phase change, r is the nucleus radius, σ is the surface tension, and ΔG_v is the free energy change due to the solute phase change per volume. When nucleation occurs a critical nucleus radius must be attained for particles to grow. For a nucleus to grow spontaneously the Gibbs free energy gained from the liquid to solid phase change

must be greater than the energy necessary to form the surface of the particle. As the size of the nucleus increases, ΔG_s increases and ΔG_v decreases. Below the critical nucleus radius the free energy necessary to form a surface dominates and the nucleus is thermodynamically inclined to dissipate. Above the critical nucleus radius the free energy gained from the phase change dominates and the nucleus is thermodynamically inclined to grow and precipitate (Randolph and Larson 1988). Another way to understand nucleation is to look at the minimum work necessary for nucleus formation. For an incompressible nucleus the minimum work, W_{min}, to form a nucleus is defined as

$$W_{min} = \sigma * A + n * \Delta \mu \tag{2.9}$$

where n is the number of solute particles that form a nucleus, A is the surface area of the nucleus, and $\Delta \mu$ is the change in chemical potential due to the phase change. Since the solid phase chemical potential is equal to the liquid phase chemical potential at equilibrium, $\Delta \mu$ can be represented by

$$\Delta \mu = \mu[T,P,y^*] - \mu[T,P,y] = k*T\ln(y^* * \exp(-K*y^*)) - k*T\ln(y*\exp(-K*y)) \tag{2.10}$$

where y* is the equilibrium mole fraction, k is the Boltzmann constant, and K is a function of T and P. This method of calculating the change in chemical potential allows for nonideal systems to be examined (Debenedetti 1990).

Assuming a spherical nucleus, the critical nucleus radius, r_c, can be obtained by taking the derivative of ΔG (Equation 2.8) and solving it for dΔG/dr=0 to obtain

$$r_c = \frac{-2 * \sigma}{\Delta G_v} \tag{2.11}$$

(Randolph and Larson 1988). The critical radius can then be estimated using supersaturation through the Gibbs-Thompson equation and equation 2.11 to get

21

$$r_c = \frac{2 * \sigma * \upsilon}{k * T * \ln(S)} \qquad (2.12)$$

where v is the molecular volume, k is the Boltzmann constant, and r is the particle radius (Mullin 2004). From equations 2.11 and 2.12 it can be seen that the critical nucleus radius decreases with increasing supersaturation because the free energy gained from the phase transition increases. A reaction rate can be estimated by assuming an Arrhenius reaction velocity equation of

$$J = A * \exp\left(\frac{-\Delta G}{k * T}\right) \qquad (2.13)$$

where J is nuclei formed per time per volume, A is a constant, and k is the Boltzmann constant (Mullin 2004).

Once a critical nucleus has formed, secondary nucleation and growth begins. Particle growth may either be dominated by the rate of integration of molecules onto the surface of the nucleus or the rate of diffusion of molecules to the surface of the nucleus. For a diffusion controlled system, the growth rate is

$$\frac{dM}{dt} = \frac{D}{x} A * (c - c^*) \qquad (2.14)$$

where M mass of the particle, D is the diffusion coefficient, x is film thickness, and A is the particle surface area. Film thickness is the distance that a molecule will travel to reach the surface of the nucleus. The growth rate increases with enhanced mass transfer (e.g. agitation which decreases film thickness) until the integration of molecules onto the nucleus becomes the controlling mechanism. The models for surface integration depend on the method of integration (Randolph and Larson 1988), but may be estimated by splitting the above equation into

$$\frac{dM}{dt} = k_d A*(c - c_i) \qquad (2.15)$$

$$\frac{dM}{dt} = k_r A*(c_i - c^*) \qquad (2.16)$$

where k_d is mass transfer coefficient (D/x), k_r is the rate constant of integration, and c_i is the solute concentration at the nucleus-solute interface. Since c_i is difficult to obtain, another option is to incorporate both equations into

$$\frac{dM}{dt} = K_G A*(c - c^*)^g \qquad (2.17)$$

where K_G is an overall growth coefficient and g is an empirical value (Mullin 2004). K_G and g can then be estimated through experimental methods.

Summary

Many studies have been performed to further the understanding of the underlying phenomena of the SAS precipitation process. Early studies concentrated on changing the operating conditions to control the particle characteristics. These experiments led to the assumption that spray characteristics, specifically initial droplet size, may control the resulting particle characteristics. While initial droplet size has some effect on the particle characteristics, the effect was not as dramatic as originally predicted. The effect of diffusion was studied to determine its effect on SAS. Several models were developed to understand the counterdiffusion between droplets and the bulk fluid. These models were developed to help understand how operating conditions control dynamic droplet behavior and relate mass transfer during the SAS precipitation process to the resulting particle characteristics. Experimental studies looked at how spray and diffusion properties affected the particle characteristics.

The experiments described in this dissertation use a high magnification imaging system to image the spray characteristics at several points from the nozzle outlet while performing the SAS precipitation process. This visualization method provides information on spray characteristics including initial droplet diameter, droplet growth/dissipation, and jet break up regime. The particles formed by the SAS precipitation process were characterized by using scanning election microscope (SEM). By characterizing the spray of solution and resulting particles, the experiments described in this dissertation further the understanding of the effect spray characteristics have on the SAS precipitation process.

Thermosyphons

Background of Thermosyphons

The defining mechanism of a thermosyphon is fluid flow driven by buoyant forces. Thermosyphons can be designed for many purposes, and this is reflected in the plethora of variations in thermosyphon design. A thermosyphon may be a fluid-filled pipe or loop which can be sealed or open to the atmosphere. The fluid inside the pipes can be selected to maximize either heating or cooling. Depending on the application the fluid can operate as one or two phase. These variations have lead to thermosyphons being applied to many applications.

Historically, thermosyphons have been used to transfer heat. The Perkins tube, patented in 1831, is the first industrial application of a thermosyphon. The system consisted of hermetically sealed tubes filled with a small amount of liquid. These tubes could rapidly and efficiently transport heat from a furnace to a remote heat sink.

Applications for the thermosyphons were expanded to include steam generation, house heating, window defogging, and engine cooling. Turbines are cooled using internal voids filled with fluid. Thermosyphons are also used to stabilize the ground underneath buildings which are located in and near the Arctic Circle by drawing heat away from the foundation during the winter to reduce thawing. Numerous heat exchanger designs employ thermosyphons to increase efficiency (Lock 1992). To understand the intricacies of buoyant flow, several studies on thermosyphons for various potential applications have been undertaken.

For example, one proposal is to use a closed loop thermosyphon to cool electronics (Chu et al. 1999). Electronics are typically cooled using air. As electronic devices become smaller, the volume for air flow decreases. By using a thermosyphon, the air to dissipate heat is divorced from the internal arrangement of the device. Two types of thermosyphons for cooling were tested: heat pipes and heat loops. Since evaporation and condensation allow the fluid to adsorb and expel the most heat, both methods use two phase systems. The heat loop had several advantages. Cooling is similar to direct cooling. Heat can be "remotely" dissipated. No pump is in the system, so no extra energy needs to be added. The heat loop volume is relatively small. When compared to forced water cooling, the thermosyphon does not produce as low of a chip temperature, but no external energy is used.

Modeling of Thermosyphons

Modeling of thermosyphons gives an estimate of the flow stability and rate. Traditionally the models for closed loop thermosyphons use a simple loop geometry such

as a circle or square. A general model was proposed by Zvirin (1981). There are various

theoretical assumptions when dealing with thermosyphon models. A plug-flow

temperature profile is assumed. A common assumption is the Boussinesq approximation

which assumes fluid density is constant except when considering the effect of density on

buoyancy. Fluids are also considered incompressible since pressure change is neglected.

The momentum equation was represented by

$$\rho_o \frac{\partial u}{\partial t} = \frac{\partial P}{\partial s} - \rho * g * \hat{e}_z \bullet \hat{e}_s - 4\frac{\tau_w}{d_H} \qquad (2.18)$$

where ρ_o is the reference density, u is velocity, s is the direction of flow, g is the

acceleration due to gravity, $\hat{e}_z$ and $\hat{e}_s$ are unit vectors, τ_w is wall shear stress, and d_H is

hydraulic diameter. The wall shear stress was represented by

$$\tau_w = 0.5*f*\rho_o*u^2 = 0.5*(a/Re^b)*\rho_o*u^2. \qquad (2.19)$$

For a fully developed forced flow in a circular pipe $a=16$ and $b=1$. Typically f, the

friction coefficient, is higher than

$$f=16/Re \qquad (2.20)$$

for a natural convection loop where Re is the Reynolds number. These factors change

with the geometry of the loop and need to be determined experimentally. The energy

transfer equation was written as

$$\rho_o * c * \left(\frac{\partial T}{\partial t} + u\frac{\partial T}{\partial s} \right) - k * \frac{\partial^2 T}{\partial s^2} = 4\frac{q}{d_H} - 4\frac{h}{d_H}(T - T_o) + \frac{1}{A}\int \Phi dA \qquad (2.21)$$

where c is specific heat, k is thermal conductivity, q is heat flux, d_h is the hydraulic

diameter, h is heat transfer coefficient, T_o is a reference temperature, A is the cross

sectional area, and Φ is the dissipation function which is usually neglected. The heat

transfer coefficient was assumed from forced flow. By eliminating P and integrating

throughout s, the distance around the loop, the momentum equation was written as

$$\rho_o * \gamma * \frac{\partial Q}{\partial t} = -g \oint \rho dz - 2 * \rho_o \oint f * u^2 * \frac{ds}{d_H}, \gamma = \oint \frac{ds}{A} \qquad (2.22)$$

where Q is the volumetric flow rate, γ is a geometric parameter, and f is the friction

factor. Assuming the cross sectional area was uniform, the last term was

$$-2 * \rho_o \oint f * u^2 * \frac{ds}{d_H} = -0.5 * \rho_o * R * Q^2, \ R = 4 \oint \frac{f * ds}{d_H A^2}. \qquad (2.23)$$

Typically, the density is assumed to change linearly with respect to temperature, so

density was represented as

$$\rho = \rho_o * (1 - \beta * (T - T_o)) \qquad (2.24)$$

where β as the thermal expansion coefficient and subscript o represents a standard state

such as the hot or cold conditions. Common boundary conditions include continuous

temperature profile around the loop and complete mixing reached in a short length.

There are two commonly used initial conditions. At t=0, the temperature throughout the

loop is at T_o. Natural circulation begins when forced flow is shut off, so the

thermosyphon is at a steady state flow rate. If the loop is completely symmetric, flow

may start after a lag period.

The model can be simplified by assuming a steady state system where time

dependent terms equal zero. By neglecting axial conduction and viscous dissipation the

momentum and energy equations can be simplified to

$$\frac{1}{2} * \rho_o * R * Q^2 = \beta * g * \rho_o * \oint T dz \qquad (2.25)$$

$$\rho_o * c * u * \frac{dT}{ds} = 4 * \frac{q}{d_H} - 4 * \frac{h}{d_H} (T - T_o). \qquad (2.26)$$

If it is assumed that the axial temperature distribution in the hot and cold sections is linear, the flow rate can be defined as

$$Q = \left(\frac{2 * \beta * g * \Delta z * P}{\rho_o * c * R} \right)^{\frac{1}{3}}$$ (2.27)

where P is total input power and Δz is the height difference between the center of the hot and cold zones.

The flow in thermosyphons may be stable or unstable. Modeling has shown three possible unstable states: start of motion, growth of flow and temperature oscillations leading to flow reversal, and multiple steady state solutions. The start of motion can be observed when a dense layer builds up on top of a hot layer. Oscillations may occur when the temperature profile changes due to a rapid flow rate (Zvirin 1981). Using equations 2.18-2.27 the rate and stability of flow in time dependent and steady state flows can be estimated.

A commonly studied thermosyphon configuration has a cold section at the top of a rectangular loop and a hot section at the bottom. The temperature zones are then connected by two vertical insulated pipes. Models for this system and systems with a similar hot to cold zone orientation, such as circular loops, are typically developed to estimate stable operating regimes. Maiani et al. (2003) used point sources for the hot and cold sections along the horizontal axis with adiabatic sides in the z-direction. Heat transfer was modeled to occur due to a constant wall temperature since this is easier to accomplish experimentally than a constant heat transfer rate. The flow in the system was modeled with differential equations for momentum and energy. Possible steady-state conditions for this system included clockwise, counter clockwise, and zero flow.

Mousavian et al. (2004) modeled a rectangular loop which was at the University of Genoa with a similar configuration. The loop had a cooling heat exchanger at the top and a heater on the bottom. Experimental data from this loop was obtained to evaluate the validity of the model. The model is based off the general form of the mass, momentum, and energy equations. By using the Boussinesq assumption, the "s" coordinate system, "W" as the mass flow rate, and three energy transfer section these equations were simplified to

$$\frac{\partial W}{\partial s} = 0 \tag{2.28}$$

$$\left(\frac{L_t}{A}\right)\frac{dW}{dt} + g\oint \rho_o[1 + \beta(T_0 - T)]dz + \bar{f}\left(\frac{L_t}{DA^2}\right)\frac{W^2}{2*\rho_o} = 0 \tag{2.29}$$

where L_t is length. The energy equation was split up into three distinct regions:

$$\rho_o * C_p * \left(\frac{\partial T}{\partial t} + \frac{W}{\rho_o * A}\frac{\partial T}{\partial s}\right) = \frac{4*q'''}{D} \text{ [hot zone]} \tag{2.30}$$

$$\rho_o * C_p * \left(\frac{\partial T}{\partial t} + \frac{W}{\rho_o * A}\frac{\partial T}{\partial s}\right) = \frac{4*u*(T_s - T)}{D} \text{ [cold zone]} \tag{2.31}$$

$$\rho_o * C_p * \left(\frac{\partial T}{\partial t} + \frac{W}{\rho_o * A}\frac{\partial T}{\partial s}\right) = 0 \text{ [adiabatic vertical zones]} \tag{2.32}$$

where C_p is the heat capacity. The stability of this loop was evaluated using the Grashof number

$$Gr = \frac{g\beta D^3 \rho_o^2 Q_h H}{A\mu^3 C_p} \tag{2.33}$$

where Q_h is the heat source power, D is the diameter of the loop, and H is the height of the loop. The Grashof number varies with how much heat is brought into the system and the height difference of hot and cold zones by the heat capacity of the system. A lower

Grashof number results in an unstable system. When the Grashof number is plotted vs. the Stanton number,

$$St=(U*A)/(W*C_p), \qquad\qquad (2.34)$$

on a log scale an increase in the Stanton number decreases the operating conditions which result in instability. This model shows that heat transfer rate and height are important to consider when designing a thermosyphon (Mousavian et al. 2004).

Thermosyphons with Supercritical Working Fluids

Thermosyphons which have working fluids in the supercritical phase have been investigated by several researchers. Chatoorgoon (2001) simulated the flow of supercritical water in an open thermosyphon loop for cooling a nuclear reactor core. The system was well defined with a known inlet temperature and pressure, and the outlet pressure was set to equal the inlet pressure. The system was modeled using a point heat source and sink along the horizontal portions of a rectangular open loop with the inlet and outlet of the system at the bottom of the loop before the heat source. The inlet flow rate was predicted to reach a maximum as the inlet temperature increased. The stability of the system was best near and below the maximum inlet flow rate. The stability decreased when an increased temperature resulted in a decrease of inlet flow rate. The area, friction, and inlet temperature all have an effect on the maximum energy which can be transferred in a stable process using this system.

Using supercritical carbon dioxide as the working fluid in thermosyphons has also been explored. The buoyancy effects on carbon dioxide were studied by van der Kraan et al. (2005) to assist with heat exchanger design. They assert that for pressures of 120 bar,

buoyant flow is negligible in heat exchanger design. To study this effect, carbon dioxide flow in vertical pipes was simulated. To perform this simulation, the overall mass transfer coefficient was calculated. Heat transfer to the fluid was controlled by several factors. With an increased pressure, the heat transfer coefficient decreased. At a constant pressure, the heat transfer coefficient went through a maximum while increasing the wall temperature at a pseudo-critical temperature. At high wall temperature the carbon dioxide at the wall was gas-like so the thermal transport efficiency was low. This effect was most evident at pressures near the critical point. As pressure increased the heat transfer coefficient showed a lower temperature dependence (van der Kraan, et al. 2005). This study suggests that thermosyphon flow will be best at supercritical conditions near the critical pressure, below 100 bar.

A study on a closed-loop thermosyphon with supercritical carbon dioxide as the working fluid was performed by Yoshikawa et al. (2005). Experimental and theoretical data was examined to characterize the system. This study was performed to develop a supercritical carbon dioxide extraction system driven by buoyant flow. This system was tested at 78 to 150 bar, 15 to 55°C, and 0.55 to 0.80 g/mL. The flow of carbon dioxide was measured using a flow meter and time-related UV detection of an acetone tracer. The flow rates of carbon dioxide between 0.8 to 4 m/min were produced by altering the pressure, temperature, and the mass of carbon dioxide loaded into the system. The system was predicted to have an increased velocity with an increasing density change between the hot and cold zones (Yoshikawa et al. 2005).

Summary

Thermosyphon systems have been studied experimentally and theoretically to estimate the rate and stability of buoyancy driven flow for a wide variety of applications. There have been several studies on thermosyphons with supercritical fluids as the working fluid. The experiments described in this dissertation use a thermosyphon system with supercritical carbon dioxide as the working fluid to micronize a solute. This supercritical thermosyphon process utilizes buoyancy to induce flow of a supercritical fluid. The dependence of supercritical carbon dioxide solvent strength on the fluid density was used to dissolve and precipitate a solute within the system.

3. Effect of Process Conditions on the Spray Characteristics of a PLA+Methylene Chloride Solution in the Supercritical Antisolvent Precipitation Process

Introduction

The supercritical antisolvent (SAS) precipitation process is an effective method to produce particles of a variety of materials. The SAS process is performed by spraying a solution into an antisolvent, typically supercritical carbon dioxide ($scCO_2$). The solution is made up of a solvent which is miscible with the antisolvent and a solute which is immiscible with the antisolvent. The solution exits a nozzle as a jet which breaks up in a precipitation chamber that is filled with $scCO_2$. The solvent mixes with the CO_2 antisolvent to induce supersaturation of the solute. The solute then precipitates as particles, typically micron-sized (Dixon et al. 1993). Depending on the process conditions, nozzle configuration, and species involved, particles with different characteristics, e.g. size and morphology, can be obtained (Martin et al. 2002, Reverchon et al. 2002, Randolph et al. 1993, Chattopadhyay and Gupta 2000, Yeo and Kiran 2005, Reverchon and Adami 2006).

In SAS, jet break up may occur as a two phase spray or a gas-like plume (Lengsfeld et al. 2000). When the jet break up occurs as a two phase spray, the jet will break into droplets. A link between the droplet characteristics and the produced particles has previously been proposed (Dixon et al. 1993, Mawson et al. 1997). There are several two phase jet break up regimes with the limits being Rayleigh jet break up and atomization. Rayleigh jet break up produces drops from jet segments, while atomization

results in a cone of small droplets which have broken off the jet (Lin and Reitz 1998). The properties, e.g. density and viscosity, of both the bulk phase ($scCO_2$) and the sprayed liquid phase can be used to define the break up regime (Kerst et al. 2000, Ohnesorge 1936). These properties can also be used to predict spray characteristics. Theoretical models have used these properties to predict the jet break up length (Lengsfeld et al. 2000, Chávez et al. 2003) and initial droplet diameter (Chávez et al. 2003, Rantakylä et al. 2002, Mukhopadhyay and Dalvi 2004) which occur during the SAS process. The estimates of the jet break up length and initial droplet diameter in SAS can be improved using a high resolution camera system which has been shown to provide visual data of the spray characteristics (Bell et al. 2005).

Modeling work by various groups has shown results which provide insight into the SAS process. Most models have dealt with the two phase jet break up regime. Droplets have been predicted to initially swell due to an initial rapid influx of $scCO_2$ which may be sufficient to induce nucleation (Lora et al. 2000). After initially swelling, droplets either shrink or continue swelling due to solvent mass transfer out of the droplet and $scCO_2$ mass transfer into or out of the droplet, depending on the proximity to the mixture critical point (Werling and Debenedetti 1999). A few models have looked at gas-like plume jet break up. Bounding a droplet by a concentration gradient instead of a phase interface, Werling and Debenedetti (2000) extended their model to include miscible conditions. This model showed a decrease in the droplet lifetime, which indicates faster mixing, when compared to the phase interface bounded droplet. By mapping the solution concentration throughout the spray, supersaturation was predicted to occur at different rates depending on the proximity to the nozzle outlet and the center

34

axis of the nozzle. These differing rates may lead to a distribution of particle sizes (Martín and Cocero 2004).

The underlying phenomena that control the particle formation are not fully understood. Three scenarios of precipitation were considered by Lengsfeld et al. (2000): (1) One particle results from one droplet, so the particle morphology would need to be controlled by the droplet characteristics. (2) Several particles result from one droplet with several nucleation sites. (3) Nucleation occurs in the bulk fluid when supersaturation is reached through gas-like mixing. Chávez et al. (2003) proposed that the dominant phenomena will be determined by the relative time scales of nucleation and diffusion. Moreover, it has been reported that proximity to the mixture critical point and phase behavior of the system can influence particle formation in the SAS precipitation process (Reverchon et al. 2003). Reverchon et al. (2003) have shown that a variation in yttrium acetate particle size resulted when SAS was performed at operating conditions below, near, and above the mixture critical point.

By imaging the spray process, a comparison of spray characteristics and particle characteristics can be obtained to further understand the controlling mechanism of SAS. Sun et al. (2003) have shown that there is a significant difference between refractive indices of carbon dioxide and a carbon dioxide/organic solvent mixture. Therefore the interface between a solvent rich droplet and carbon dioxide will be visible. The spray of solution into supercritical carbon dioxide has been imaged by several groups (Lengsfeld et al. 2000, Mawson et al. 1997, Shekunov et al. 2001, Dukhin et al. 2005, Bristow et al. 2001, Carretier et al. 2003). In previous studies, Bell et al. (2005) developed a high resolution camera setup to visualize SAS. Images of individual droplets, gas-like plumes,

and jet break up lengths were obtained. This visualization system was also used in this study.

In this study, a variety of spray characteristics were imaged using a high-magnification camera setup by performing two sets of experiments: fixed density with select pressure and temperature combinations and fixed temperature with select pressure and density combinations. Visualizations of the spray characteristics and SEM images of the collected particles were analyzed and compared. The system chosen for this investigation is the precipitation of poly(L-lactic) acid (PLA) from a methylene chloride solution by spraying into compressed carbon dioxide. This system is well documented (Lee and Kuk 2002, Kalogiannis and Panayiotou 2005, Tsivintzelis et al. 2004, Reaves et al. 1998, Lazzaroni et al. 2005), has previously been studied in our laboratory (Martin et al. 2002, Bell et al. 2005), and, in general, has been shown to result in small particle size variations over a wide range of operating conditions (Martin et al. 2002, Randolph et al. 1993, Mawson et al. 1997). Also, a wide range of spray characteristics has been observed over a small range of operating conditions (Bell et al. 2005).

Experimental

Materials

Poly(L-lactic) acid was obtained from Birmingham Polymers. The PLA had an inherent viscosity of 1.09 dL/g in $CHCl_3$ at 313 K which coincides with a molecular weight of ~120,000 Daltons. Methylene chloride (MC) was obtained from Fisher Scientific. Carbon dioxide, grade 5.5, was obtained from Airgas. All materials were used as received.

Supercritical Antisolvent Precipitation Apparatus

The apparatus used to perform the SAS process (Figure 3.1) was modified from the system used by Martin et al. (2002). The precipitation chamber is a Jerguson gage, model 19TM40, with a volume of 80 cm^3, a height of 48 cm, and two opposing vertical windows that allow illumination and imaging within the vessel. An Isco 500D syringe pump delivers CO_2 and maintains the vessel pressure within ± 1.3 bar before the spray process. The liquid solution is delivered by an Acuflow Series II HPLC pump with a pulse dampener, Scientific Systems, Inc. model 12-0625. The solution is fed through 0.16 cm O.D. stainless steel tubing to 100 μm I.D. fused silica capillary tubing, Alltech part no. 1900331. The capillary tubing goes through the interior of 0.32 cm O.D. stainless steel tubing and into the CO_2 filled precipitation chamber. The solution is sprayed from the 100 μm nozzle outlet into the precipitation chamber. The nozzle was made by cutting capillary tubing with wire cutters and examining the ends with an optical microscope to achieve a flat tip (as shown in the 0 mm row of Figures 3.2 and 3.3). Using a T-connector it is possible to flow carbon dioxide around the fused silica capillary tubing. The bottom of the precipitation chamber has 0.32 cm O.D. stainless steel tubing for outflow. An inline filter separates the precipitated particles from the vessel effluent. The membrane filter, Millipore FGLP02500, has a pore size of 0.22 μm and is mounted in a 25 mm stainless steel filter holder, Millipore XX4502500. To safely operate the pressurized system a pressure gage, McDaniel Controls, and blowout plug, HiP 16-63AF1, are attached to the precipitation chamber. A thermocouple in the pressure vessel is used as the input device for a temperature controller, Omega CSC32. The temperature controller powers a heating element, strip heaters during the fixed density experiments

and heating tape during the fixed temperature experiments, to maintain the temperature of the precipitation chamber.

Imaging System

A Questar QM 100 MK III long distance microscope lens from the Astro-Optics Division of Company Seven was used to obtain a high magnification. The lens has a working distance of 8 to 35 cm. The magnification of the camera system can be as high as 0.90 μm/pixel (Bell et al. 2005). Attached to the lens is a monochrome CCD camera, Cohu 2122. The camera has a chip size of 768 x 494 pixels with a pixel size of 8.4 x 9.8 μm^2. The shutter speed is 60 frames per second. A strobe light, Monarch Nova Strobe DA Plus 115, with a pulse duration of 30 μs was used to shorten the effective exposure time. The camera and lens are mounted on a tripod with an X-Y stage to allow mobility in the X, Y, and Z direction. The output of the camera is digitized by an analog to digital video converter, Dazzle Digital Video Creator. The video is collected on a computer in .mpg format using Dazzle Moviestar software. The frames of the video are separated into individual .bmp images using JASC Animation Shop 3.

The droplets are sized from the individual images using ImageJ, available from the National Institutes of Health at http://rsb.info.nih.gov/ij/. Jet break up length is the distance measured using the straight line tool from the edge of the capillary tubing to the point where the jet edge exhibits rippling. The diameter of a droplet is obtained by using the straight line tool in the fixed temperature experiments and the oval tool in the fixed density experiments. The diameter of a droplet in the fixed density experiments is estimated using the equation for the area of a circle. The μm/pixel scale for each set of

images is determined from an *in situ* image of the 400 μm O.D. capillary tubing obtained before each experiment.

Images of the precipitated particles collected during the SAS process are obtained using a scanning electron microscope, Zeiss DSM 940. Samples for the scanning electron microscope are prepared by transferring particles from the filter holder to a stub with double-sided carbon tape on the surface. The stub is sputter-coated for 4 minutes with gold. Images of the particles are obtained in .tif format. The particles are analyzed using ImageJ by measuring the diameter using the straight line tool.

Procedure

For these experiments, the SAS apparatus (Figure 3.1) was operated as a batch process. The system is charged with carbon dioxide through the Isco syringe pump, which is then set to maintain the operating pressure in the precipitation chamber. The temperature controller is set to the operating temperature. The bulk fluid temperature and pressure are allowed to stabilize at the selected set points before spraying the solution. A 1 wt% PLA in MC solution is pumped by the HPLC pump with all valves closed. When the pressure downstream of the HPLC pump is above that of the precipitation chamber, valve 1 is opened. The solution is sprayed at a fixed flow rate of 0.9 or 1.6 cm^3/min for 30 sec to 2 min. The pulse dampener reduces fluctuations in the pressure drop to a ±4 bar oscillation with a period of 1.6 s . The HPLC pump is shut off, and valve 1 is closed. Valve 2 is opened to resume pressure control by the Isco syringe pump. Valve 3 is opened fully and valve 4 is adjusted to control the vessel outflow, which is monitored through the change in volume of the Isco syringe pump. Two vessel volumes of carbon

dioxide are used to purge the system of solvent. Precipitated PLA particles are collected and dried in the filter holder while the system is purging. Valve 3 is closed after purging the system. The filter holder is removed from the system when fluid stops exiting valve 4. The filter membrane and particles that can be brushed from the filter holder are placed in a glass bottle. MC is pumped through the nozzle to remove residual PLA and prevent clogging of the nozzle. Valve 3 is opened to reduce the pressure in the precipitation chamber. The system is then dried by purging with $scCO_2$.

The imaging process occurs simultaneously with the batch spray process. The camera and lens are positioned at the selected axial distance from the nozzle. Recording is started when valve 1 is opened to start the spray. Recording is stopped when the HPLC pump is stopped and valve 1 is closed.

Approximately 2 minutes of video are obtained for each experiment. Only images from the first 10 to 30 seconds are used as data due to a slight pressure reduction during the spray. Images were typically obtained with the center of the spray in frame. In several instances, the camera was turned 90° to take greater advantage of the aspect ratio while imaging the solution at the nozzle exit (0 mm). The video data file is separated into discrete images. Jet breakup length and droplet sizes are analyzed from these images.

Experimental Conditions

Experimental conditions are listed in Table 3.1, grouped as three fixed density conditions and three fixed temperature conditions. The experimental conditions are plotted along with isothermal lines in Figure 3.4. The operating conditions were chosen to allow for characterization of the spray near the transition from two phase to one phase

jet break up. The carbon dioxide density was determined from the NIST chemistry webbook (Lemmon et al. 2005). Pressures of 83.8 bar, 89.1 bar, and 94.3 bar were used in the density calculations.

Experiments with a fixed initial carbon dioxide density of 0.33 ± 0.02 g/cm^3 were performed at pressure and temperature combinations of 84 bar and 313 K, 89 bar and 318 K, and 94 bar and 323 K (Table 3.1). A 1 wt% PLA/MC solution was sprayed at a flow rate of 0.9 cm^3/min which resulted in a pressure drop of ~90 bar across the nozzle. Binary VLE data of methylene chloride and carbon dioxide (Tsivintzelis et al. 2004, Reaves et al. 1998) indicates that after spraying the solution into carbon dioxide a supercritical mixture will be present at these three conditions. Videos were taken of the spray at five distances from the nozzle outlet (0 mm, 7 mm, 13 mm, 23 mm, and 43 mm) for each condition. The jet breakup length was measured from images taken at the nozzle outlet (0 mm). Images from the next four positions (7 mm, 13 mm, 23 mm, and 43 mm) were used to observe and measure droplet characteristics.

Fixed temperature experiments at 323 K were performed at three pressure and density combinations: 84 bar and 0.24 g/cm^3, 89 bar and 0.28 g/cm^3, and 94 bar and 0.32 g/cm^3 (Table 3.1). The pressure values were selected to correspond to those of the fixed density experiments. Videos were taken at six distances from the nozzle (0 mm, 3 mm, 7 mm, 14 mm, 24 mm, and 34 mm). In addition to the distances similar to those visualized in the fixed density experiments, the 3 mm distance was added to visualize the initial droplet diameter. The spray at 84 bar and 0.24 g/cm^3 was additionally visualized at 44 mm from the nozzle outlet. The flow rate of 1 wt% PLA/MC solution for these experiments was 1.6 cm^3/min which resulted in a pressure drop of ~20 bar across the

41

nozzle. Binary VLE data for carbon dioxide and methylene chloride indicates that after spraying the solution into the precipitation chamber for 45 seconds the mixture will be supercritical at 89 bar, 0.28 g/cm^3 and 94 bar, 0.32 g/cm^3 but subcritical at 84 bar, 0.24 g/cm^3 (Tsivintzelis et al. 2004, Reaves et al. 1998). The difference between pressure drops from the fixed temperature and fixed density experiments is attributed to the use of separate strands of capillary tubing for the two sets of experiments, therefore the data sets have been evaluated separately.

Results

Representative images from the visualizations of the fixed density experiments are presented in Figure 3.2 and fixed temperature experiments are presented in Figure 3.3. Each image is a representative still frame from a video obtained at the experimental conditions (figure column headings) and the distance from the nozzle outlet (figure row headings). Data obtained from images collected at each experimental condition is presented in Table 3.2. The jet break up length measurements are plotted in Figures 3.5 and 3.6. Measurements of the average droplet diameters are plotted versus distance from the nozzle outlet in Figures 3.7 and 3.8. Error bars in Figures 3.5-8 represent the standard deviation and are in a large part due to changes in the measured lengths rather than measurement error. SEM images of particles obtained from the fixed density experiments are shown in Figure 3.9 and from the fixed temperature experiments are presented in Figure 3.10.

Fixed Density Experiments

Column (a) of Figure 3.2 shows images of a 1 wt% PLA/MC solution sprayed at a flow rate of 0.9 cm^3/min into carbon dioxide at 84 bar and 313 K. For these conditions, the spray is clearly in the atomization regime as evidenced by the coherent jet and the presence of distinct droplets. The average jet break up length was measured as 545 μm. Droplets with various diameters are visible at 7 mm, 13 mm, 23 mm, and 43 mm from the nozzle outlet. The average droplet diameter increases from 90 μm at 7 mm to 130 μm at 13 mm and then decreases with increasing distance from the nozzle (Figure 3.7). The number of droplets in each image (droplet number density) decreases with increasing distance from the nozzle outlet. SEM images show the PLA particles for these process conditions have diameters between 0.5 μm and 2 μm and many of them are agglomerated (Figure 3.9a).

Column (b) of Figure 3.2 presents images of a 1 wt% PLA/MC solution being sprayed into carbon dioxide at 89 bar and 318 K. The jet breaks up through atomization at a length of 500 μm. The average droplet diameter at 7 mm from the nozzle is 60 μm; it increases to 80 μm at 13 mm and then decreases to 44 μm at 23 mm (Figure 3.7). The droplet number density decreases as distance from the nozzle increases. At 23 mm, only 4 droplets were seen in the images, and there are no visible droplets at 43 mm from the nozzle. The particles collected at 89 bar and 318 K are slightly agglomerated with particle diameters ranging from 0.2 μm to 2.5 μm (Figure 3.9b).

Images of the spray from carbon dioxide conditions of 94 bar and 323 K are presented in column (c) of Figure 3.2. The average jet break up length is 315 μm (Figure 3.5). Unlike the two previous conditions the jet breaks up as a gas-like plume: No

distinct droplets were visualized. At 7 mm from the nozzle outlet there are large refractive index variations; in the video these variations appear as waves oriented in various directions. The refractive index variations are attributed to density variations in the bulk fluid. Refractive index variations in the fluid continue 13 mm and 23 mm from the nozzle. The refractive index variations are weak or not visible at 43 mm. Particles obtained at 94 bar and 323 K have diameters of 0.5 μm to 1.5 μm and exhibit little agglomeration (Figure 3.9c).

Fixed Temperature Experiments

Column (a) of Figure 3.3 shows images of the spray of a 1 wt% PLA/MC solution at a flow rate of 1.6 cm^3/min into carbon dioxide at 84 bar and 0.24 g/cm^3 with a temperature of 323 K. The jet break up is in the atomization regime and begins at 1100 μm from the nozzle outlet (measured on images with lower magnification than those at other conditions). The average droplet diameter shows an initial increase until reaching a maximum value that it holds through 44 mm from the nozzle outlet (Figure 3.8). Visualizations taken at 3 mm from the nozzle outlet show a section of the spray with the jet unbroken and droplets present. The average initial droplet diameter at 3 mm from the nozzle outlet is 40 μm. At 7 mm from the nozzle outlet, the average droplet diameter increased to 80 μm. The average droplet diameter and standard deviation were, respectively, calculated as 100 μm and 50 μm at 14 mm, 120 μm and 70 μm at 24 mm, and 120 μm and 70 μm at both 34 mm and 44 mm from the nozzle outlet. . The droplet number densities are 0.6, 6.6, and 7.5 droplets/image at 3 mm, 7 mm, and 14 mm from the nozzle outlet, respectively. Unagglomerated PLA particles were collected at 84 bar

and 0.24 g/cm^3 with diameters ranging from less than 0.1 μm to 5.5 μm (Figure 3.10a) with what appears to be a bimodal distribution.

Column (b) of Figure 3.3 shows the spray of 1 wt% PLA/MC solution into carbon dioxide at 89 bar and 0.28 g/cm^3. The jet break up length was measured as 920 μm. The average droplet diameter was measured as 40 μm at 3 mm from the nozzle outlet (Figure 3.8). The average droplet diameter was measured as 75 μm at 7 mm, 100 μm at 14 mm, and 110 μm at 24 mm. At 34 mm from the nozzle outlet the average droplet diameter decreased to 80 μm. Standard deviations at 3 mm, 7 mm, and 14 mm are 10 μm, 28 μm, and 49 μm, respectively. The droplet number densities are 1.9, 1.7, and 2.8 droplets/image at 3 mm, 7 mm, and 14 mm from the nozzle outlet, respectively. The PLA particles collected from SAS at 89 bar and 0.28 g/cm^3 have diameters ranging from 0.4 μm to 1.9 μm (Figure 3.10b).

The spray of 1 wt% PLA/MC solution at 1.6 cm^3/min into carbon dioxide at 94 bar and 0.32 g/cm^3 is shown in column (c) Figure 3.3. The average jet break up length was measured as 630 μm (Figure 3.6). At 3 mm from the nozzle outlet, the jet structure was evident as a faint phase interface and a few distinct droplets (average diameter of 40 μm) were observed. Further from the nozzle, no interface or droplets were observed and the jet break up exhibited gas-like plume features. Refractive index variations (seen as waves passing through the video frame) were observed in visualizations taken at 7 mm, 14 mm, 24 mm, and 34 mm from the nozzle exit. The particles collected at 94 bar and 0.32 g/cm^3 have diameters within the range of 0.2 μm to 2.2 μm (Figure 3.10c).

Discussion

Figure 3.5 shows that the jet break up length decreases as the bulk carbon dioxide temperature is increased at a fixed density. Jet break up length also decreases as pressure is increased at a fixed temperature (Figure 3.6). These decreases in jet break up length with increases in temperature and/or pressure are consistent with the findings of Lengsfeld et al. (2000) where they also report decreased jet break up lengths with increases in pressure for methylene chloride sprayed into CO_2. Lengsfeld et al. reported that an increase in pressure created a more miscible system where they have found that the surface tension rapidly approached zero for a methylene chloride jet at their highest pressure and temperature of 85 bar and 308 K. They describe that the surface tension rapidly diminishes at this condition at a distance shorter than the characteristic breakup length and as such distinct droplets never form. Rather, the jet spreads in a fashion characteristic of gaseous jets as opposed to atomization into distinct droplets. Indeed, we have observed that at our highest temperature and pressure condition, the jet breaks up as a gas-like plume without the formation of liquid droplets (Figure 3.2c and Figure 3.3c). Therefore, the transition of the jet break regime from atomization to a gas-like plume is coincident with a reduction in the surface tension as well as a reduction in the jet break up length.

There are images of two jet break up regimes in both Figures 3.2 and 3.3: atomization and a gas-like plume. In the fixed density experiments, 84 bar and 313 K produces a jet break up through atomization, and droplets persist throughout the images (Figure 3.2a). At 89 bar and 318 K the jet break up occurs closer to the nozzle, and droplets dissipate closer to the nozzle (Figure 3.2b). Jet break up occurs as a gas-like

plume at 94 bar and 323 K (Figure 3.2c). In the fixed temperature experiments, atomization was observed at 84 bar and 0.24 g/cm^3 and also at 89 bar and 0.28 g/cm^3 (Figures 3.3a and 3.3b). A gas-like plume was again observed at 94 bar and 0.32 g/cm^3 at the elevated flow rate used in the fixed temperature experiments (Figure 3.3c).

When the jet breaks up through atomization, droplets were observed to initially swell then shrink as they travel away from the nozzle outlet. This growth and subsequent dissipation has been proposed to be due to the diffusion of carbon dioxide into the droplet and methylene chloride and carbon dioxide out of the droplet (Mukhopadhyay and Dalvi 2004, Werling and Debenedetti 2000). At 84 bar and 313 K the droplets initially swell and begin to shrink as indicated by a maximum measured droplet diameter at 13 mm (Figure 3.7). The droplets were observed to travel past 43 mm, the furthest distance from the nozzle that was measured. At the higher temperature and pressure of 89 bar and 318 K (Figure 3.3b), no droplets were observed in the images obtained 43 mm from the nozzle outlet indicating all droplets dissipated before this distance. These results imply that increased temperature and pressure result in shorter droplet lifetimes. The fixed temperature experiments at 323 K yielded similar results. Droplets are visible at all visualized distances from the nozzle outlet at 84 bar and 0.24 g/cm^3. The droplets were observed to swell in average diameter by a factor of 4 from the initial measurement at 3 mm to the measurement made at 24 mm from the nozzle outlet. Beyond 24 mm the average droplet diameter showed little change. The average droplet diameter remained constant at 120 μm through 44 mm, but with an increasing standard deviation. The data at 89 bar and 0.28 g/cm^3 demonstrates significant droplet swelling from 3 mm to 24 mm from the nozzle outlet. A decrease in average droplet diameter was observed at 34 mm

which again indicates droplet swelling followed by subsequent droplet dissipation like that seen in the fixed density experiments. It should be noted that the maximum average droplet diameter occurs further from the nozzle in the fixed temperature experiments likely due to the elevated solution flow rate employed. Also, the droplet number density decreased with increasing pressure and density in the fixed temperature experiments.

In both the fixed density and fixed temperature experiments, a gas-like plume was observed at 94 bar, 0.32 g/cm^3, 323 K. At this condition, the 1 wt% PLA/MC solution was fed into the system at flow rates of 0.9 cm^3/min and 1.6 cm^3/min. Gas-like plumes were evident at both flow rates with the major observed difference being that the jet break up length was longer at the faster flow rate. The miscibility of methylene chloride and carbon dioxide at this condition is such that a one phase system is reached before complete jet break up occurs. Therefore, droplet formation does not occur to an appreciable extent, and those few droplets that do form dissipate rapidly at this condition.

Despite different spray characteristics, the PLA particle size distributions are very similar at all conditions except 84 bar and 0.24 g/cm^3, the only condition predicted to be subcritical at equilibrium according to binary VLE data (Tsivintzelis et al. 2004, Reaves et al. 1998). While both atomization and a gas-like plume were observed above the mixture critical point, the particles obtained were within the range of 0.2 to 2.5 μm in diameter which indicates the particle size is not solely controlled by the spray characteristics. However, at the condition predicted to be below the mixture critical point, 84 bar and 0.24 g/cm^3, larger particles, up to 5.5 μm in diameter, were obtained. The larger particles obtained at 84 bar and 0.24 g/cm^3 could be attributed to the effect of the thermophysical properties at these subcritical conditions on the spray characteristics,

mass transfer, and nucleation. In general, it was found that spray characteristics had little influence on particle distribution when operating at supercritical conditions.

Conclusions

This paper has investigated the precipitation of poly(L-lactic) acid in the SAS process using high magnification imaging of the spray. Jet break up was observed to occur in two distinct regimes depending on the process conditions. A transition in the jet break up regime from atomization to a gas-like plume coincides with a decrease of jet break up length and the distance from the nozzle at which droplets dissipate. Increases in pressure and temperature in the fixed density experiments and increases in pressure and density in the fixed temperature experiments resulted in a reduction in jet break up length. In the case of atomization, the average droplet diameter increased then decreased with the distance from the nozzle outlet. Particles obtained from both regimes resulted in similar particle size and distribution with the exception of the particles obtained at the lowest CO_2 density. Despite large variations in the spray characteristics there was little variation in the obtained PLA particles.

Tables

Bulk scCO$_2$				1 wt% PLA/MC Solution		Visualizations
Density (g/cm^3)	Temperature (K)	Pressure (bar)	Viscosity (cP)	Flow Rate (cm^3/min)	Nozzle Velocity (m/s)	Distances from the Nozzle (mm)
Fixed Density						
0.33	313	84	0.025	0.9	0.5	0,7,13,23,43
0.33	318	89	0.025	0.9	0.5	0,7,13,23,43
0.33	323	94	0.025	0.9	0.5	0,7,13,23,43
Fixed Temperature						
0.24	323	84	0.021	1.6	0.8	0,3,7,14,24,34,44
0.28	323	89	0.023	1.6	0.8	0,3,7,14,24,34
0.32	323	94	0.025	1.6	0.8	0,3,7,14,24,34

Table 3.1 List of experimental conditions used to perform SAS as well as the distances from the nozzle imaged at each condition. Fixed density experiments were designed to examine the effect of pressure and temperature combinations on the SAS spray process at 0.33 ± 0.02 g/cm^3. Fixed temperature experiments were designed to examine the effect of pressure and density combinations on the SAS spray process at 323 K. The densities were calculated from Lemmon et al. (2005).

Density (g/cm^3)	Temp (°C)	Pressure (bar)	Distance from Nozzle (mm)	Average Droplet Diameter (μm)	Standard Deviation (μm)	Droplets per Image	# of Droplets Measured	Jet Break Up Length (μm)	Measured Jet Images	Standard Deviation of Jet Length (μm)
Fixed Density										
0.33	313	84	0					545	37	26
			7	88	39	N/A	548			
			13	126	37	N/A	151			
			23	105	33	N/A	212			
			43	90	45	N/A	24			
0.33	318	89	0					500	134	82
			7	63	23	N/A	357			
			13	82	27	N/A	45			
			23	44	40	N/A	4			
			43	No Droplets			0			
0.33	323	94	0					315	128	38
			7	No Droplets			0			
			13	No Droplets			0			
			23	No Droplets			0			
			43	No Droplets			0			
Fixed Temperature										
0.24	323	84	0					1100	122	82
			3	35	10	0.6	314			
			7	75	28	6.8	348			
			14	101	49	7.5	1490			
			24	119	68	4.6	1149			
			34	122	75	3.6	938			
			44	119	78	2.6	2496			
0.28	323	89	0					919	27	84
			3	36	12	1.9	607			
			7	75	30	1.7	591			
			14	97	41	2.8	1292			
			24	106	52	0.5	244			
			34	82	175	0.9	217			
0.32	323	94	0					630	27	71
			3	35	13	0.2	54			
			7	No Droplets			0			
			14	No Droplets			0			
			24	No Droplets			0			
			34	No Droplets			0			

Table 3.2 Statistical data of analyzed results for all performed experiments.
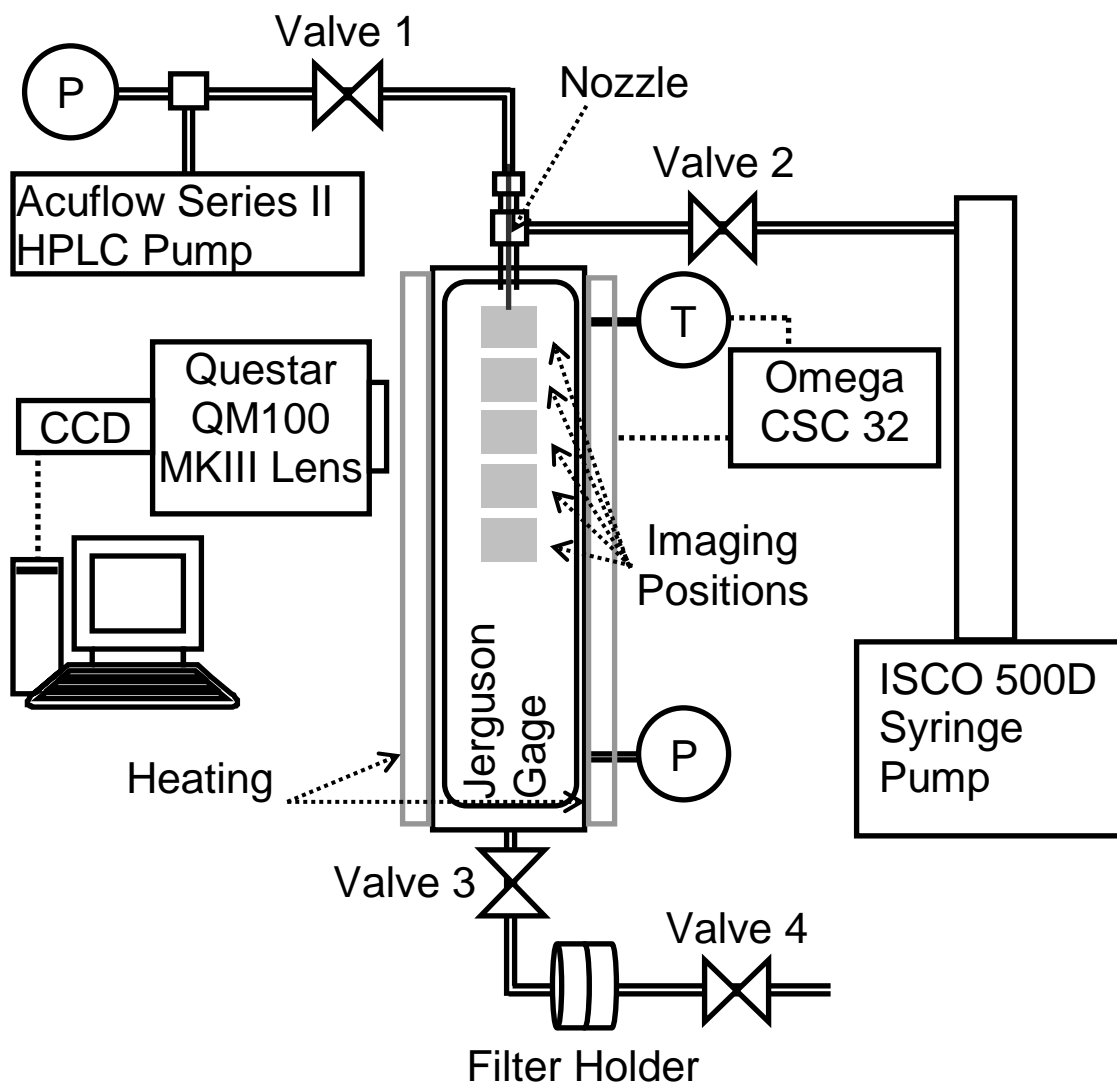
Figure 3.1 Diagram of the imaging system and the apparatus used to perform the supercritical antisolvent precipitation process. The positions imaged in the spray are represented by the shaded boxes inside the Jerguson gage.
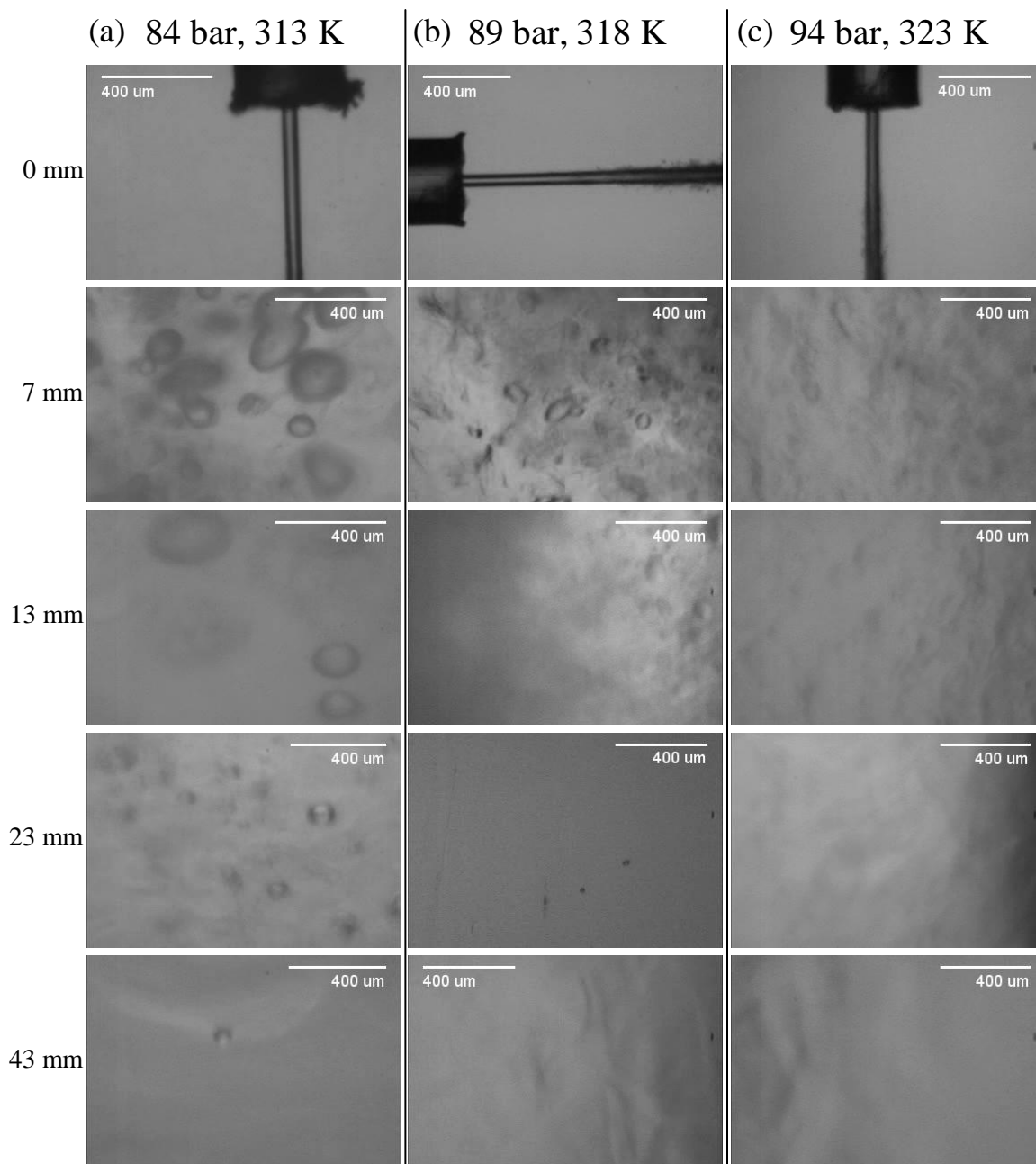
Figure 3.2 Selected frames taken from movies of the spray at given distances from the nozzle in fixed density SAS experiments. These images are taken from a set of experiments performed at a bulk CO_2 density of 0.33 ± 0.02 g/cm^3 and select pressure and temperature combinations with a 1 wt% poly (L-lactic) acid/ methylene chloride solution flow rate of 0.9 cm^3/min.

(a) 84 bar, 0.24 g/cm³   (b) 89 bar, 0.28 g/cm³   (c) 94 bar, 0.32 g/cm³
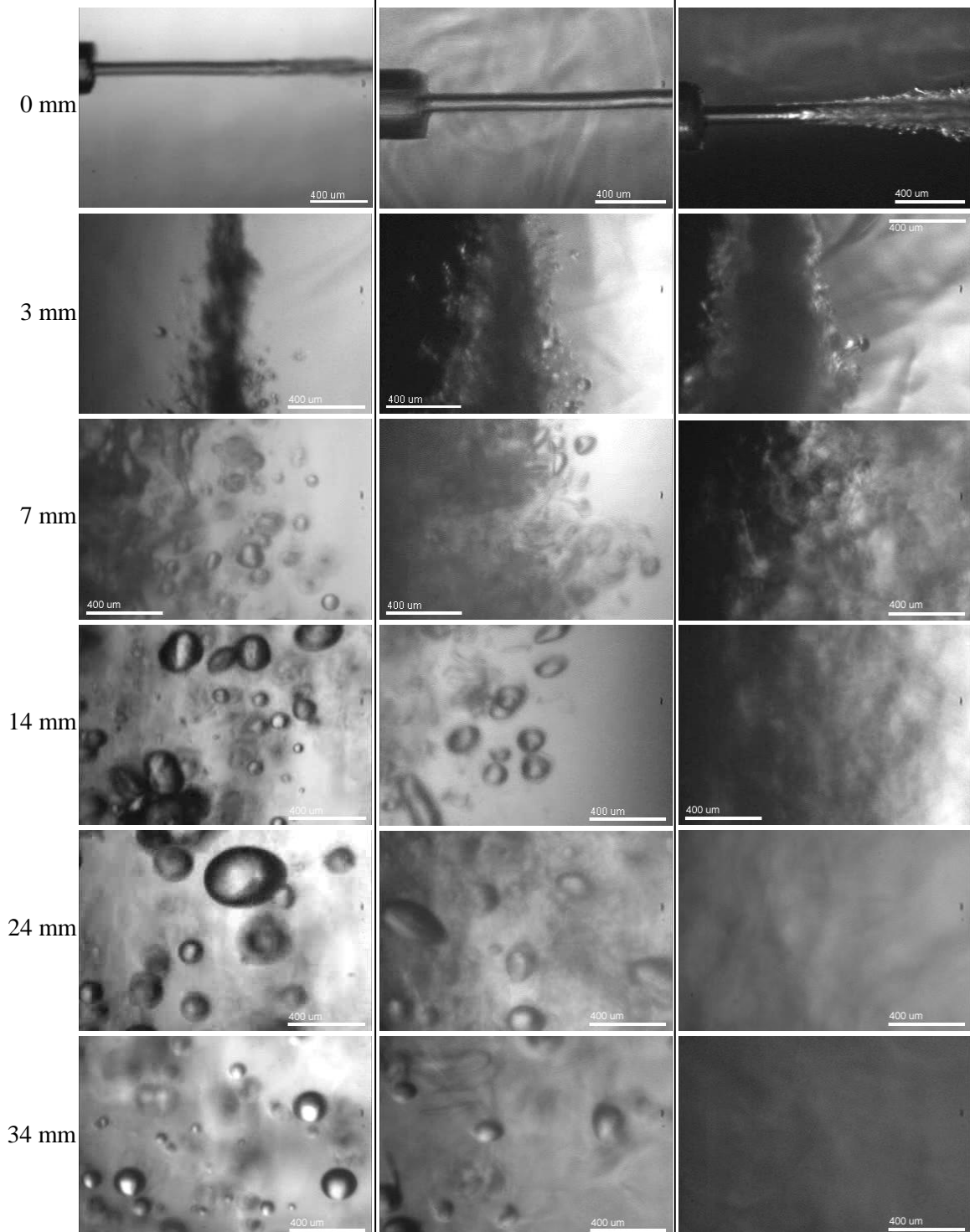
Figure 3.3 Selected frames taken from movies of the spray at given distances from the nozzle in fixed temperature SAS experiments. These images are taken from a set of experiments performed at a bulk CO_2 temperature of 323 K and select pressure and density combinations with a 1 wt% poly (L-lactic) acid/ methylene chloride solution flow rate of 1.6 cm^3/min. (previous page)
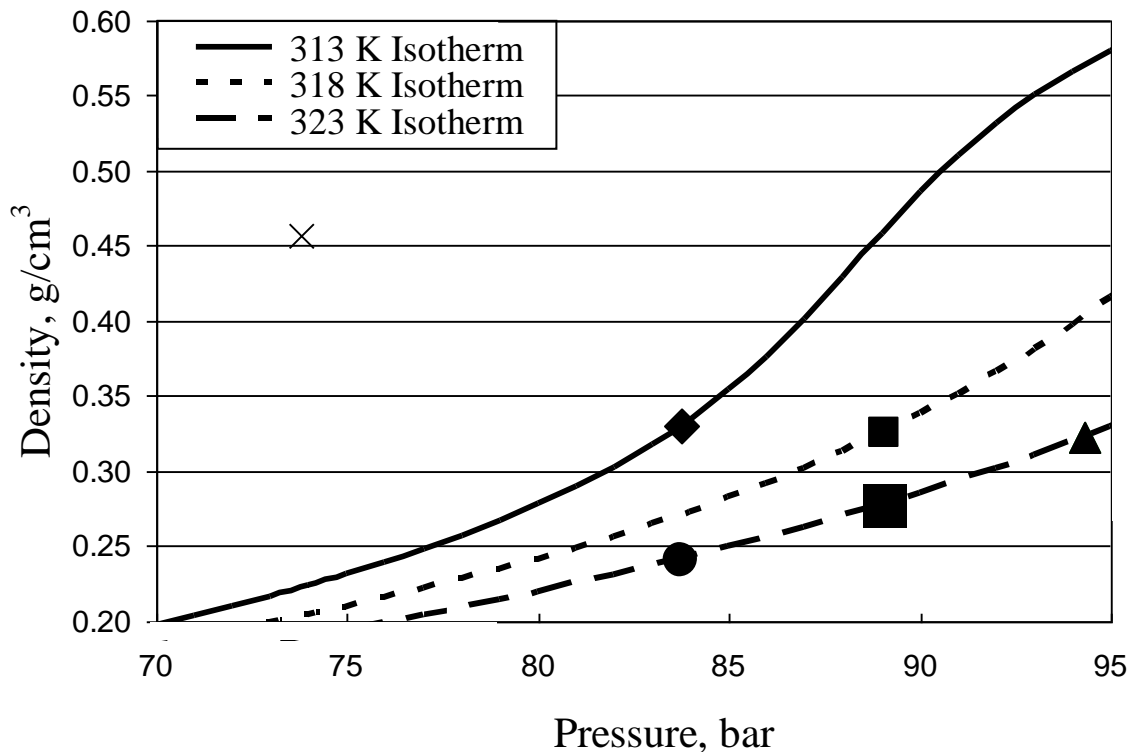
Figure 3.4 Experimental conditions displayed on a density vs. pressure diagram. The

symbols represent the two sets of experimental conditions: fixed density and fixed

temperature. The lines represent isotherms of pure carbon dioxide at the operating

temperatures calculated from the NIST chemistry webbook (Lemmon et al. 2005). The

"x" indicates the location of the critical point of pure CO_2.
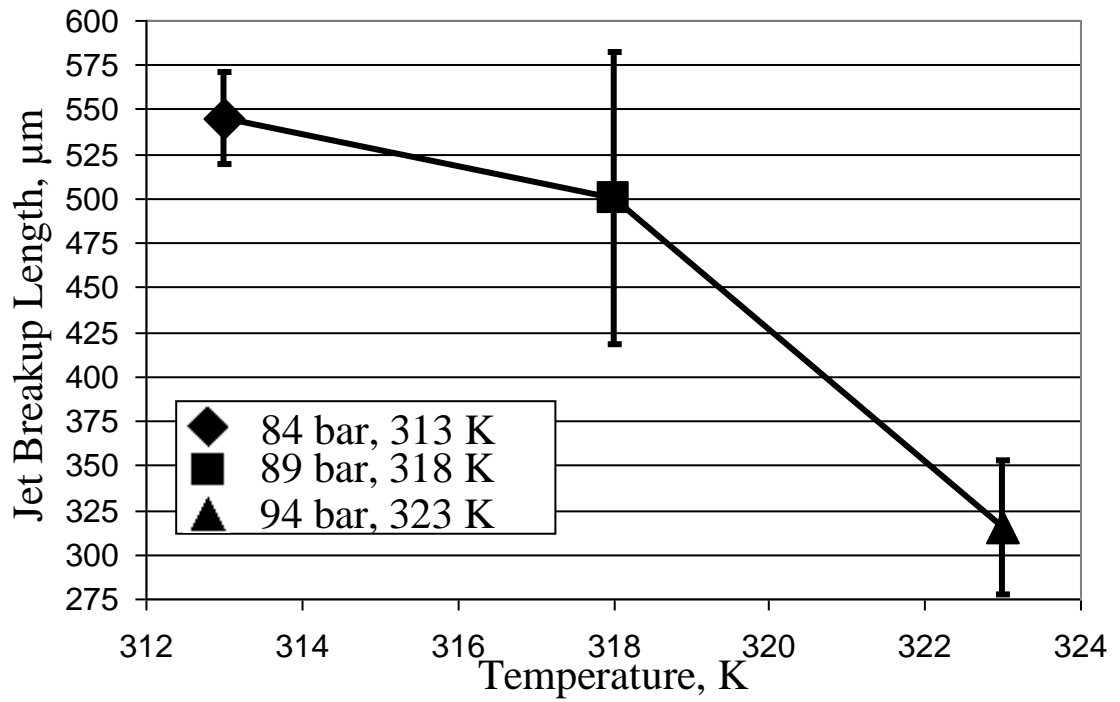
Figure 3.5 Jet breakup lengths from fixed density SAS experiments performed at 0.33 ±

0.02 g/cm^3 and select pressure and temperature combinations with a 1 wt% poly (L-

lactic) acid/ methylene chloride solution flow rate of 0.9 cm^3/min.
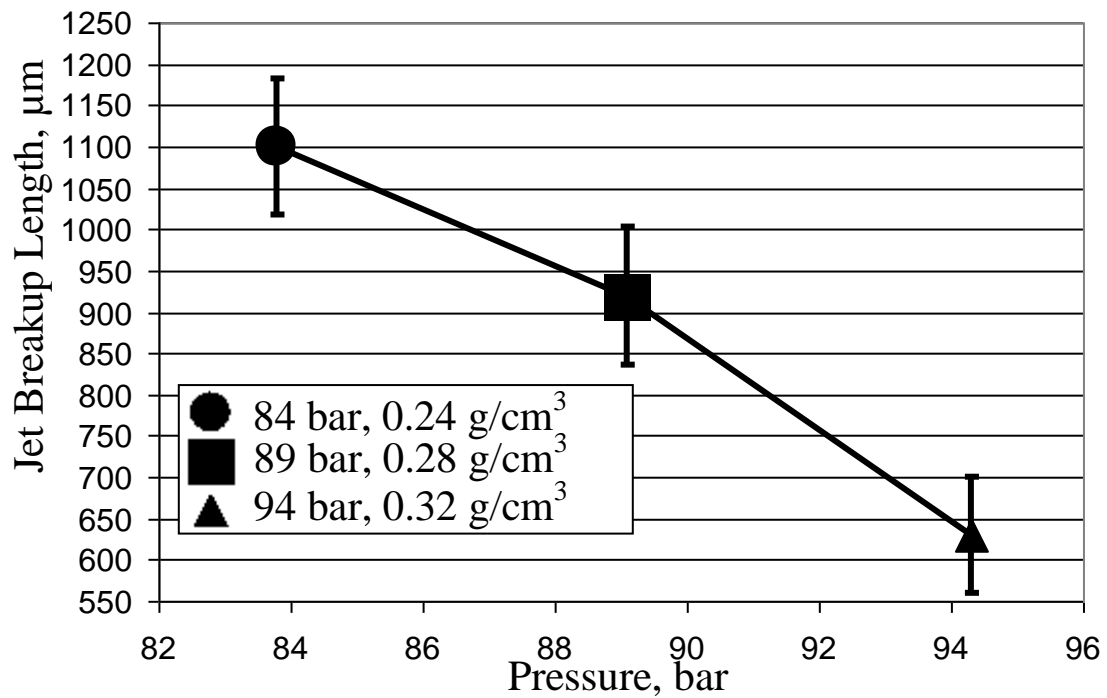
Figure 3.6 Jet breakup lengths from fixed temperature SAS experiments performed at 323

K and select pressure and density combinations with a 1 wt% poly (L-lactic) acid/

methylene chloride solution flow rate of 1.6 cm^3/min.
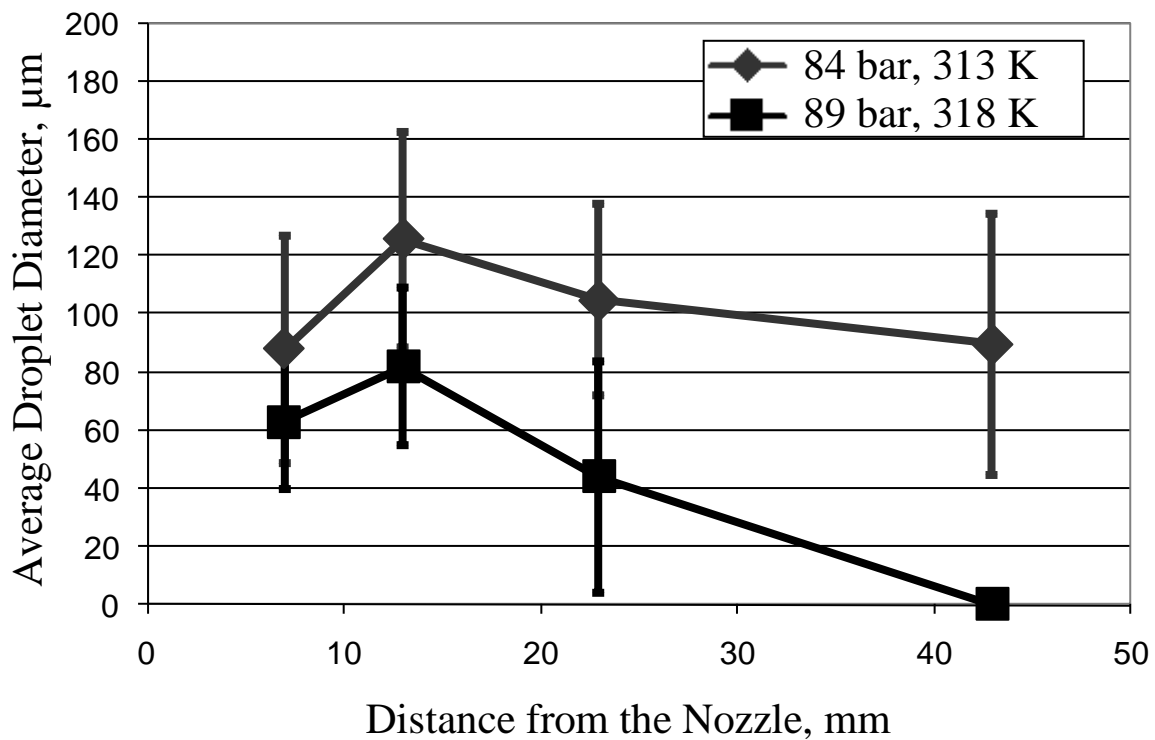
Figure 3.7 The average droplet diameter at four distances in fixed density SAS

experiments performed at 0.33 ± 0.02 g/cm^3 and select pressure and temperature

combinations with a 1 wt% poly (L-lactic) acid/ methylene chloride solution flow rate of
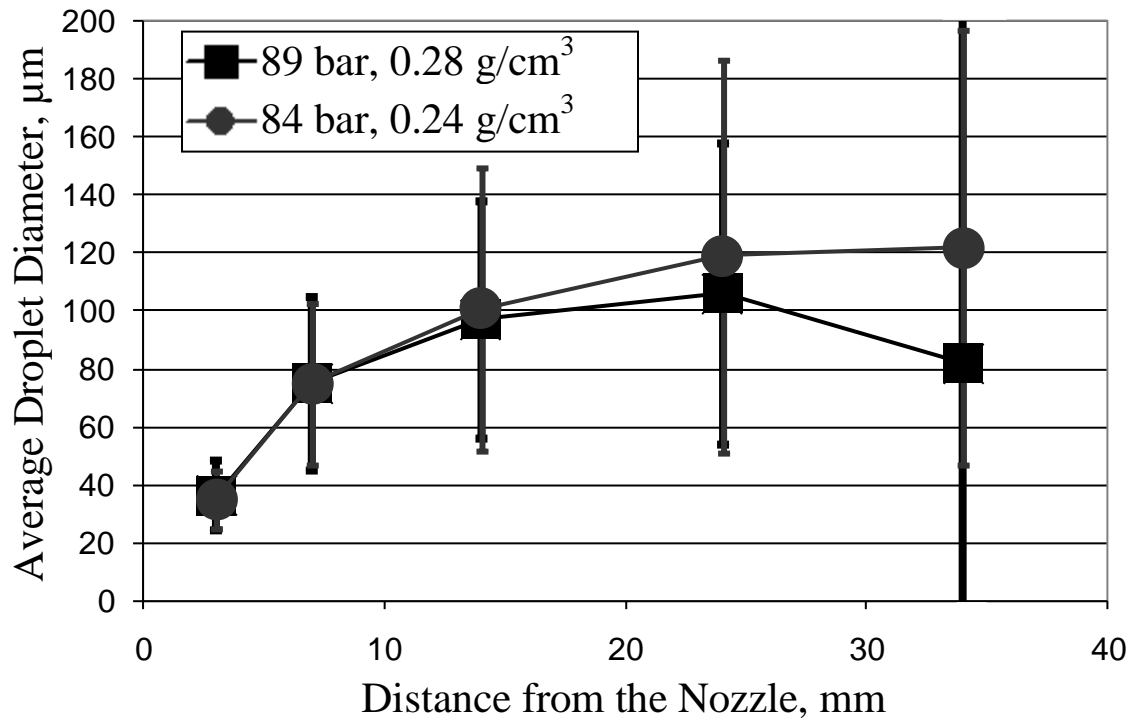
0.9 cm^3/min.

Figure 3.8 The average droplet diameter at five distances in fixed temperature SAS

experiments performed at 323 K and select pressure and density combinations with a 1

wt% poly (L-lactic) acid/ methylene chloride solution flow rate of 1.6 cm^3/min.

(a)

(b)

(c)
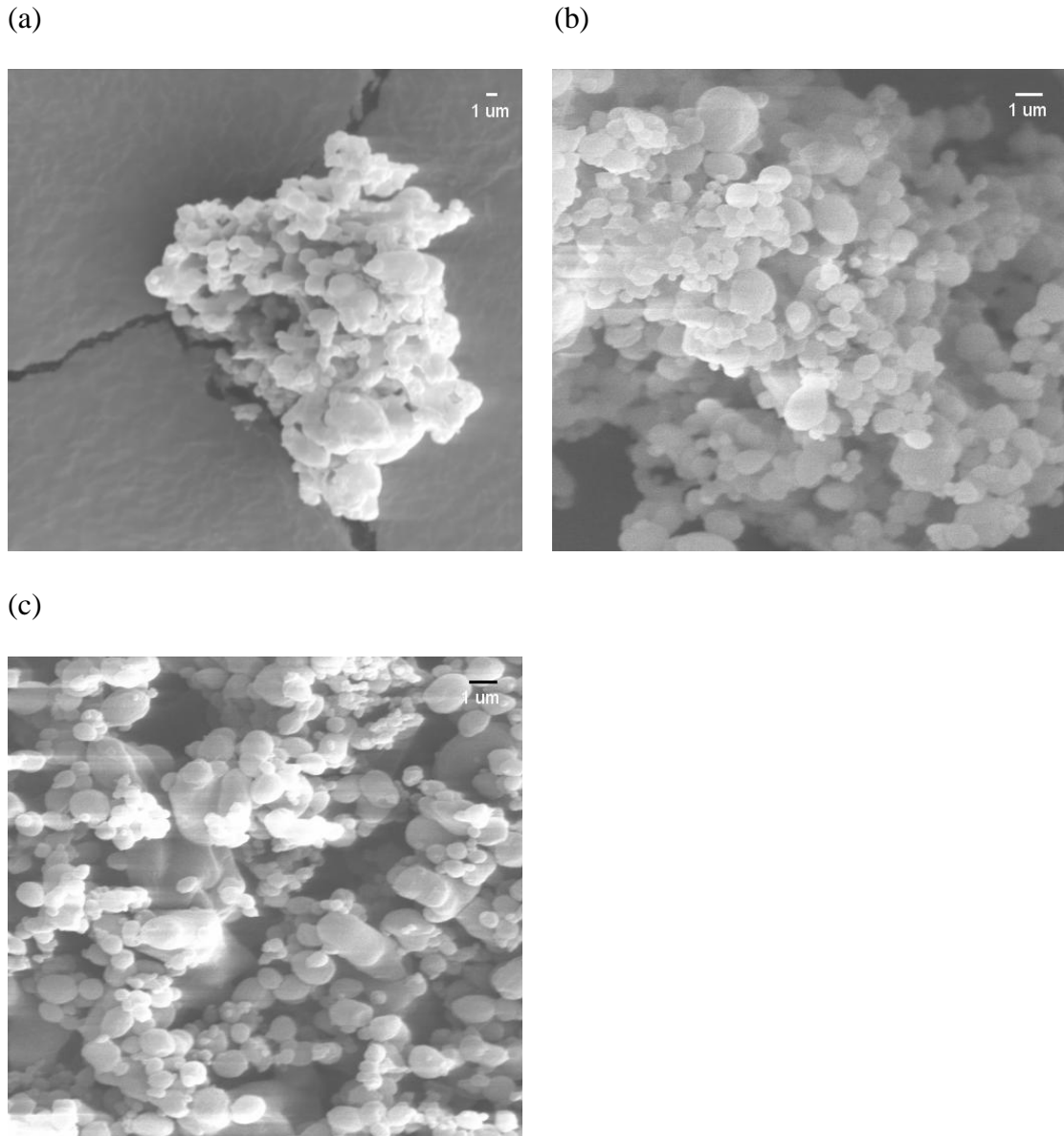
Figure 3.9 Scanning electron microscope images from fixed density SAS experiments performed at 0.33 ± 0.02 g/cm^3, pressure and temperature combinations of (a) 84 bar, 313 K ; (b) 89 bar, 318 K; (c) 94 bar, 323 K, and a 1 wt% poly (L-lactic) acid/ methylene chloride solution flow rate of 0.9 cm^3/min. Poly(L-lactic) acid particles were obtained with the following diameters (a) 0.5 – 2 µm (b) 0.2 - 2.5 µm (c) 0.5 – 1.5 µm.

(a)
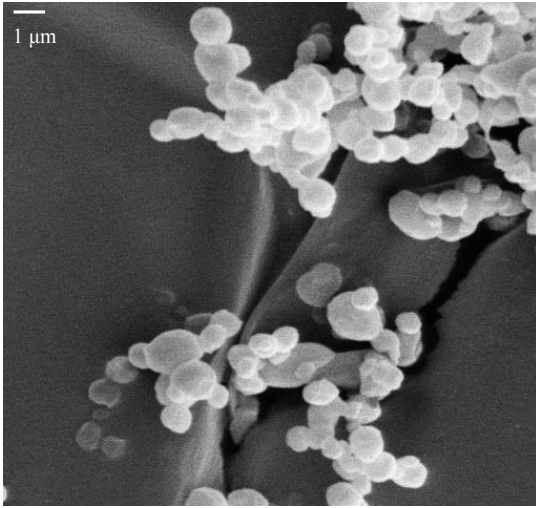
(b)
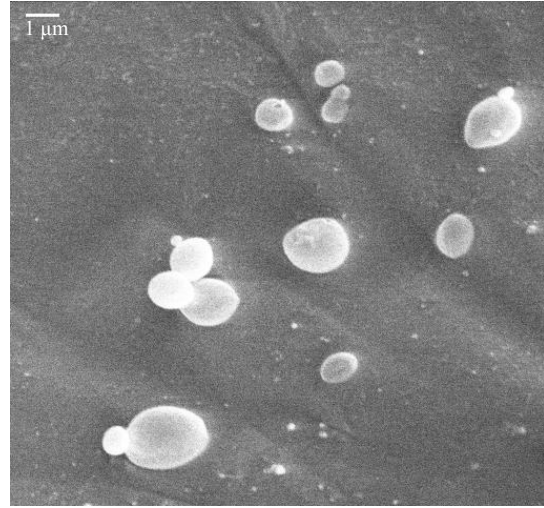
(c)
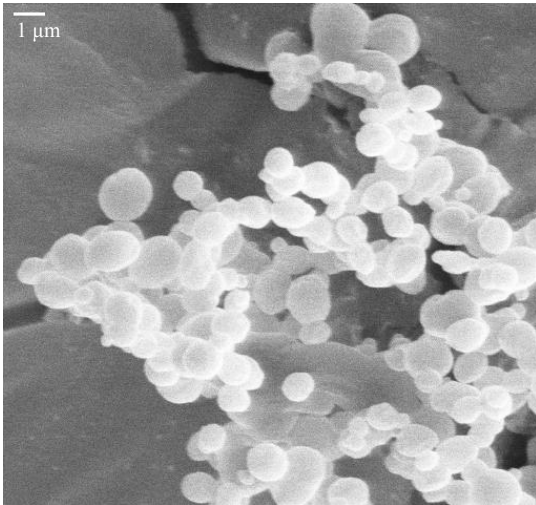
Figure 3.10 Scanning electron microscope images from fixed temperature SAS experiments performed at 323 K, pressure and density combinations of (a) 84 bar, 0.24 g/cm^3; (b) 89 bar, 0.28 g/cm^3; (c) 94 bar, 0.32 g/cm^3, and a 1 wt% poly (L-lactic) acid/ methylene chloride solution flow rate of 1.6 cm3/min. Poly(L-lactic) acid particles were obtained with the following diameters: (a) <0.1 – 5.5 µm, (b) 0.4 - 1.9 µm, (c) 0.2 – 2.2 µm.

4. Investigation of the Influence of Polymer Solute Solubility on the SAS Precipitation Process and Particle Characteristics

Introduction

The supercritical antisolvent (SAS) precipitation process is a method used to produce micron scale particles of a variety of organic and polymeric materials. To perform the SAS precipitation process, a solution is sprayed into a supercritical antisolvent, typically carbon dioxide (Randolph et al. 1993, Johnston et al. 1993). The solution consists of an organic solvent which is miscible with carbon dioxide antisolvent and a solute which is immiscible with carbon dioxide. The solution enters the carbon dioxide as a jet which breaks up into droplets or a gas-like plume depending on the operating conditions as demonstrated by Lengsfeld et al. (2000). The organic solvent and the carbon dioxide antisolvent counterdiffuse as the solution is sprayed into the precipitation chamber as calculated through a thermodynamic model by Werling and Debenedetti (1999). This mixing, which is dependent on process parameters (e.g. temperature, pressure, solution flow rate, nozzle diameter, turbulence level), lowers the solvent strength of the solution due to the influx of carbon dioxide into solvent rich regions as Martín and Cocero (2004) reported for supercritical conditions. Nucleation begins after the solvent strength has been sufficiently reduced for the solute to be supersaturated. The solute then precipitates, typically, as microparticles that can be collected by removing the solvent with excess antisolvent (Johnston et al. 1993).

Whether the solution breaks up into droplets or a gas-like plume may depend on whether the mixture of solvent and the carbon dioxide antisolvent is a supercritical mixture at a given set of operating parameters (Lengsfeld et al. 2000). The mixture critical point is dependent on temperature, pressure, and carbon dioxide concentration as demonstrated by Reaves et al. (1998). While a system may be supercritical according to the bulk operating conditions (temperature, pressure, and CO_2 concentration), the mixture can be locally subcritical in regions where the solvent concentration is high, such as near the solvent jet entry. In a system that would be supercritical at equilibrium, nucleation may occur above or below the mixture critical point due to the local solvent concentration at the position in the spray. The location in the spray at which nucleation begins is affected by a number of factors including the underlying transport phenomena and the relation between the saturation concentration of CO_2 and the mixture critical point within the spray.

The characteristics of the particles obtained from the SAS precipitation process can be affected by the phase regime in which the solute precipitates. Operating above the mixture critical point has been shown to produce small micro or nano particles (Reverchon et al. 2003). When precipitation occurs in a supercritical mixture, mass transfer is very high. Increasing the mass transfer has been shown to decrease the particle size (Chattopadhyay and Gupta 2001). Operating below the critical point, slightly larger particles has been obtained (Reverchon et al. 2003). Microballoons, hollow microspheres, have been shown to be formed through SAS by operating at conditions near the mixture critical point. Dixon et al. (1994) formed microballoons of polystyrene from toluene solutions at subcritical conditions. Reverchon et al. (2003) demonstrated

that microballoons of networked yttrium acetate particles can be formed via SAS at temperatures and pressures just below the transition from a two phase system to a one phase supercritical system.

Studies have been performed to analyze the effect solvent strength has on the particle size when using supercritical fluids. Experiments on the gas antisolvent precipitation process have demonstrated that particle size generally increases with increasing solvent strength (Thiering et al. 2000). Nucleation theory predicts that a stronger solvent should precipitate larger particles because particles stay suspended in the solution longer and continue to grow (Randolph and Larson 1988). By decreasing the initial affinity of the solute for a solvent, the level of supersaturation reached during the SAS precipitation process is increased which should result in smaller particles. Gokhale et al. (2007) showed that utilizing acetone as an antisolvent in a methylene chloride/polyvinyl pyrrolidone solution reduces the resulting particle size when performing SAS with a slow solution flow rate. A nozzle in which carbon dioxide is premixed with the solution prior to injection into the bulk carbon dioxide was developed by Hanna and York (1994) as Solution-Enhanced Dispersion by Supercritical fluids (SEDS). Adding CO_2 before injecting the solution into the precipitation chamber induces supersaturation in the nozzle then the CO_2-expanded solution is sprayed into the bulk fluid to suppress nucleation and growth. This concept was expanded upon by Chang et al. (2005) by increasing the residence time in the nozzle to increase the resulting particle size. The method presented by Gokhale et al. (2007) and SEDS both manipulate the solvent strength before the solution is sprayed into the precipitation chamber to alter the resulting particles.

In the present study the affinity between the solute and the solvent in the SAS precipitation process is investigated using homopolymers and copolymers with different solubilities in a common solvent. By using copolymers made from the monomers of two homopolymers which have different solubilities, the solute solubility can be scaled relative to the monomer ratio without drastically changing the composition of the solute.

The Hildebrand solubility parameters of species are commonly used as a means of predicting the mutual solubility of two molecules. Similar solubility parameters indicate that two molecules are miscible. As such, appropriate solvents for a given polymer can be determined by matching the solubility parameter of the solvent with that of the polymer. The solubility parameter of a copolymer can be roughly estimated by assuming that the copolymer solubility parameter scales between the two homopolymer solubility parameters with the volume fractions of the monomers (Barton 1991). The homopolymers used in the present study were chosen based on their solubility parameters relative to ethanol which has a solubility parameter of 26.0 Mpa$^{1/2}$ (Barton 1991). Poly(methyl methacrylate) (PMMA) has a solubility parameter of 19.0 MPa$^{1/2}$, and polyvinyl pyrrolidone (PVP) has a solubility parameter of 25 MPa$^{1/2}$ (Barton 1990). From these solubility parameters and experimental results, it is known that PMMA is slightly soluble in ethanol while PVP is very soluble in ethanol. Several polymers with different solubilities in ethanol can be synthesized by making poly(methyl methacrylate-co-vinyl pyrrolidone) (PMMAVP) using different monomer ratios, methyl methacrylate: vinyl pyrrolidone. The effect of the solute solubility on SAS can then be investigated by processing several PMMAVP copolymers with different monomer ratios.

Various experimental methods can be employed to determine the solubility of solutes, such as the polymers employed in this study, in the organic solvent and CO_2 mixtures encountered in the SAS precipitation process. For example, cloud point measurements can be performed in the manner described by Martin et al. (1999) to determine the pressure at which the polymer solutes precipitate from a CO_2/organic solvent mixture; the value determined is known as the cloud point pressure. In this case, the system has two fluid phases (a CO_2 rich phase and solvent rich phase) and three components: CO_2, organic solvent, and polymer solute. Increases in CO_2 pressure applied to the organic solution reduces the solvent strength of the solution by addition of CO_2 to the liquid phase. This pressurization progressively reduces the solvent strength of the liquid phase and will result in the solute precipitating from solution when the solute saturation concentration is reached. The pressure at which the solute precipitates is known as the cloud point pressure. The CO_2 concentration in the liquid phase is dependent on the CO_2 pressure applied (Jessop and Subramaniam 2007). Examination of cloud point pressures obtained by this technique can be used to determine relative solubilities of different polymers in a given solvent system.

In the present study, the effect that solute solubility has on the SAS precipitation process was characterized through several experimental techniques. Visualization of the SAS precipitation process was used to characterize the spray of the solutions into compressed CO_2. Cloud point measurements were performed to determine the cloud point pressures of the polymers and, therefore, the relative solubilities of the polymers. Scanning electron microscopy (SEM) was used to characterize the particles produced via the SAS precipitation process. SAS experiments for each copolymer system were

performed at varying operating conditions and were analyzed using the methods described above to investigate the effect of solute solubility in the SAS precipitation process.

Experimental

Materials

Carbon dioxide, grade 5.5, was obtained from Airgas. Ethanol was obtained from AAPER Alcohol and Chemical Company. Poly(methyl methacrylate), MW 15000, was obtained from Sigma-Aldrich. Polyvinyl pyrrolidone, MW 10000, was obtained from Sigma-Aldrich.

Poly(methyl methacrylate-co-vinyl pyrrolidone) was synthesized at several monomer ratios using methyl methacrylate and vinyl pyrrolidone obtained from Sigma-Aldrich. Azobisisobutyronitrile (AIBN) obtained from Sigma-Aldrich was used as the initiator. All chemicals were used as received.

Equipment

Supercritical Antisolvent Precipitation Apparatus

The apparatus used to perform the SAS process (Figure 1) is described elsewhere (Obrzut et al. 2007). In short, the precipitation chamber is a Jerguson gage, model 19TM40, with a volume of 80 cm^3, a height of 48 cm, and two opposing vertical windows that allow illumination and imaging within the vessel. An Isco 500D syringe pump delivers CO_2 and maintains the vessel pressure within ±1.3 bar before the spray process. The liquid solution is delivered by an Acuflow Series II HPLC pump with a

68

pulse dampener, Scientific Systems, Inc. model 12-0625. The solution is fed through

0.16 cm O.D. stainless steel tubing to 100 μm I.D. fused silica capillary tubing, Alltech

part no. 1900331. The capillary tubing goes through the interior of 0.32 cm O.D.

stainless steel tubing and into the CO_2 filled precipitation chamber. The solution is

sprayed from the 100 μm nozzle outlet into the precipitation chamber. Using a T-

connector it is possible to flow carbon dioxide around the fused silica capillary tubing.

The bottom of the precipitation chamber has 0.32 cm O.D. stainless steel tubing for

outflow. An inline filter separates the precipitated particles from the vessel effluent. The

membrane filter, Millipore FGLP02500, has a pore size of 0.22 μm and is mounted in a

25 mm stainless steel filter holder, Millipore XX4502500. To safely operate the

pressurized system a pressure gage, McDaniel Controls, and blowout plug, HiP 16-

63AF1, are attached to the precipitation chamber and outlet line of the HPLC pump. A

thermocouple in the pressure vessel is used as the input device for a temperature

controller, Omega CSC32. The temperature controller powers heating tape to maintain

the temperature of the precipitation chamber.

Imaging System

   A Questar QM 100 MK III long distance microscope lens from the Astro-Optics

Division of Company Seven was used to obtain a high magnification. The lens has a

working distance of 8 to 35 cm. The magnification of the camera system can be as high

as 0.90 μm/pixel (Bell et al. 2007). Attached to the lens is a monochrome CCD camera,

Cohu 2122. The camera has a chip size of 768 x 494 pixels with a pixel size of 8.4 x 9.8

$μm^2$. The shutter speed is 60 frames per second. A strobe light, Monarch Nova Strobe

DA Plus 115, with a pulse duration of 30 µs was used to shorten the effective exposure time. The camera and lens are mounted on a tripod with an X-Y stage to allow mobility in the X, Y, and Z directions. The output of the camera is digitized at 30 frames per second by an analog to digital video converter, Dazzle Digital Video Creator. The video is collected on a computer in .mpg format using Dazzle Moviestar software.

Procedures

Polymerization

Random copolymerization of vinyl pyrrolidone and methyl methacrylate was performed following the procedure presented by Arcos et al. (1997) to synthesize PMMAVP. A mixture of the monomers at the appropriate ratio was placed in an Erlenmeyer flask. The initiator, AIBN, was added and the flask contents were mixed through sonication. The flask was sealed and placed in an oven for 2 hours at 50°C. The resulting polymer was rinsed with petroleum ether to remove residual monomer and initiator. The final theoretical monomer ratio was determined by

$$\frac{n_{MMA}}{n_{VP}} = \frac{dm_{MMA}}{dm_{VP}} = \frac{M_{MMA}(r_{MMA}M_{MMA} + M_{VP})}{M_{VP}(r_{VP}M_{VP} + M_{MMA})}$$
(4.1)

where n_i is the number-average sequence length of monomer i, m_i is the moles of monomer i in the copolymer, M_i is the moles of monomer i in the initial reaction solution, and r_i is the reactivity coefficient of monomer i (Brandrup et al. 1999). The methyl methacrylate reactivity coefficient is 4.04, and the vinyl pyrrolidone reactivity coefficient is 0.15 (Orbay et al. 1982).

While polyvinyl pyrrolidone is readily soluble in ethanol, not all batches of PMMAVP were fully miscible in ethanol due to a high loading of methyl methacrylate

70

which is sparingly soluble in ethanol. Select PMMAVP batches were placed in an excess of ethanol and thoroughly stirred, and then filtered to remove the insoluble portion of the synthesized polymer. The filtered solution was then placed in an evaporation dish where the ethanol was evaporated. The dried PMMAVP was used to make solutions for the investigation on the effect of solute solubility on the SAS precipitation process.

Cloud Point Experiments

Cloud point experiments were performed to determine the cloud point pressure of the polymers in ethanol solutions using the apparatus described by Martin et al. (1999). In the present study, the cloud point pressure is defined as the pressure at a specific temperature and concentration which results in the polymer precipitating from the CO_2 expanded ethanol solution. To perform these experiments, a known volume of a 1 wt% polymer/ethanol solution was placed inside a variable volume high pressure vessel with a view window, and then a known amount of carbon dioxide was added to the vessel. Next, the vessel was heated to the desired temperature, and the vessel volume was decreased, via movement of an internal piston, to increase the pressure above the point at which the polymer precipitates from the solution. After the system reached equilibrium at the elevated pressure, the volume was increased to determine the pressure at which the polymer redissolved. The volume was then repeatedly decreased then increased to accurately determine the cloud point pressure. A higher cloud point pressure indicates a greater solubility of the polymer in the CO_2 expanded ethanol solution hence requiring greater CO_2 concentration in the organic solution to induce precipitation.

For these experiments, the SAS apparatus (Figure 4.1) was operated as a semi-batch process as described in Obrzut et al. (2007). The system was charged with carbon dioxide through the Isco syringe pump, which was then set to maintain the operating pressure in the precipitation chamber. The temperature controller was set to the operating temperature. The bulk fluid temperature and pressure were allowed to stabilize at the selected set points before spraying the solution. The solution was pumped by the HPLC pump with all valves closed. When the pressure downstream of the HPLC pump was above that of the precipitation chamber, valve 1 was opened. The solution was sprayed at a fixed flow rate of 1.6 cm^3/min for 30 sec to 45 sec. The pulse dampener reduces fluctuations in the pressure drop to a ±4 bar oscillation with a period of 1.6 sec. After the allotted spray time, the HPLC pump was shut off, and valve 1 was closed. Valve 2 was opened to resume pressure control by the Isco syringe pump. Valve 3 was opened fully, and valve 4 was adjusted to control the vessel outflow which was monitored through the change in volume of the Isco syringe pump. Two vessel volumes of carbon dioxide were used to purge the system of solvent. Precipitated particles were collected and dried in the filter holder while the system was purging. Valve 3 was closed after purging the system. The filter holder was removed from the system when fluid stopped exiting valve 4. Valve 3 was then opened to reduce the pressure in the precipitation chamber, and the temperature controller was turned off. The filter membrane was collected and placed in a covered Petri dish.

Visualization of the SAS Precipitation Process

Visualization experiments were performed in the method described in Stephens (2003), Bell et al. (2005) and Obrzut et al. (2007). The spray characteristics were imaged at 0, 3, 7, 14, 44, and 74 mm from the nozzle outlet in the direction of the spray (Figure 4.1). Recording was started when the spray began and stopped when the spray ended. The resulting video was saved as a .mpg using the Dazzle Moviestar software. The frames of this video were separated into individual .bmp images using JASC Animation Shop 3. The droplets were manually sized from the individual images using ImageJ, available online from the National Institutes of Health. Jet break up length was the distance measured using the straight line tool from the edge of the capillary tubing to the point where the jet edge exhibits rippling. The diameter of a droplet was obtained by using the straight line tool. The µm/pixel scale for each set of images was determined from an *in situ* image of the 400 µm O.D. capillary tubing obtained before each experiment. The outer diameter of the capillary tubing was confirmed using a micron scale ruler.

Images of the precipitated particles collected during the SAS process were obtained using a scanning electron microscope, Zeiss DSM 940. Samples for the scanning electron microscope were prepared by cutting a portion of the filter membrane and placing it on a stub with double-sided carbon tape. The stub was sputter-coated for 2 minutes with gold. Images of the particles were obtained in .tif format. The particles were analyzed using ImageJ by measuring the diameter using the straight line tool.

The results presented for PMMA were obtained by Sullivan (2007), and some of the results presented for PVP were obtained by Monfort (2006).

Results

Copolymer Production and Characterization

Copolymers of methyl methacrylate and vinyl pyrrolidone were made at several theoretical monomer ratios (Table 1). The polymers synthesized were PMMAVP1 which has a theoretical molar ratio (dm_{MMA}/dm_{VP}) of 0.62, PMMAVP3 which has a theoretical molar ratio of 2.02, and PMMAVP4 which has a theoretical molar ratio of 3.01. PMMAVP1 was readily miscible with ethanol and used in experiments as synthesized. Portions of PMMAVP3 and PMMAVP4 were insoluble in ethanol. The soluble portion was isolated and used in the cloud point and SAS experiments.

The polymers were characterized by determining their cloud point pressures from a 1 wt% ethanol solution being expanded with carbon dioxide at 50°C (Table 1). The concentration of carbon dioxide in the liquid phase varies with the system pressure. PVP has the highest cloud point pressure of 94 bar. PMMAVP1 has a cloud point pressure of 92 bar. PMMAVP3 and PMMAVP4 have significantly lower cloud point pressures of 87 bar and 88 bar, respectively. Attempts to estimate the concentration of carbon dioxide in the liquid phase at the cloud point were unsuccessful. Calculating the mole fractions at the experimental cloud point conditions using equations of state resulted in identical mole fractions for the gas and liquid phase which indicates a single phase system, but the experimental results clearly indicated two phases at the cloud point pressures in the CO_2-expanded ethanol.

74

The spray characteristics of the solutions being sprayed into carbon dioxide were studied using the high magnification visualization setup (Figure 4.1). SAS operating temperature of 323 K and pressures of 84 bar, 94 bar, 101 bar, 104 bar, and 111 bar were chosen to study the transition from two phase subcritical conditions to one phase supercritical conditions (Table 2). SAS was performed on the following solutions: saturated PMMA in ethanol, 1 wt% PVP in ethanol, 1 wt% PMMAVP1 in ethanol, 1 wt% PMMAVP3 in ethanol, and 1 wt% PMMAVP4 in ethanol. Solutions were sprayed into the precipitation chamber from a 100 μm I.D. nozzle at 1.6 mL/min. High magnification video was obtained of the spray at 0 mm, 3 mm, 7 mm, 14 mm, 44 mm, and 74 mm from the nozzle outlet (Figure 4.2). The average jet break up length and average droplet diameter were obtained from the individual frames of the videos (Table 4.2). Overall values for jet break up length and droplet diameter were determined by averaging the individual averages for each polymer processed at an operating condition (Figures 4.3 and 4.4).

The jet break up length was observed to decrease with increasing pressure for all solutions (Figure 4.3). At 84 bar, the average combined jet break up length was determined to be 860 μm. The average combined jet break up length at 94 bar was calculated as 460 μm. At 101 bar, the average combined jet break up length is 310 μm. The average jet break up length for PVP at 104 bar was 260 μm with a standard deviation of 30 μm. At 111 bar the average combined jet break up length from PVP and PMMAVP4 was 205 μm.

The average droplet diameter for the polymers exhibited similar behavior at each operating condition (Table 4.2). At 84 bar (Figure 4.4), the average combined droplet diameter at 3 mm from the nozzle outlet was 57 μm. At 7 mm from the nozzle outlet the average combined droplet diameter ranges increased to 92 μm. The average combined droplet diameter was 130 μm at 14 mm from the nozzle outlet. At 44 μm for the nozzle outlet the average combined droplet diameter increased to 162 μm. Finally at 74 mm from the nozzle outlet the average combined droplet diameter increased to 185 μm. The large standard deviation is due to a significantly smaller average droplet diameter for PVP of 125 μm.

At 94 bar, average droplet diameters were obtained for PMMAVP4, PMMAVP1, and PMMA (Figure 4.4). At 3 mm from the nozzle outlet, the average combined droplet diameter was 66 μm. At 7 mm from the nozzle outlet, the average combined droplet diameter range increased to 91 μm. At 14 mm from the nozzle outlet, the average combined droplet diameter was 108 μm. At 44 mm from the nozzle outlet, the average combined droplet diameter was 153 μm. PMMA exhibited a maximum average droplet diameter of 206 μm at 54 mm from the nozzle outlet then decreased to 180 μm at 64 mm from the nozzle outlet. The average combined droplet diameter at 74 mm from the nozzle outlet was 156 μm.

At 101 bar (Figure 4.4), the system is near single phase operating conditions. At 3 mm from the nozzle outlet, the average combined droplet diameter was 68 μm. PMMA had an average droplet diameter of 78 μm at 3 mm from the nozzle outlet. At 14 mm from the nozzle outlet, the average combined droplet diameter was 109 μm. At 44 mm from the nozzle outlet, the average combined droplet diameter was 119 μm. The average

droplet diameter at 74 mm from the nozzle outlet was 126 μm. PMMA did not exhibit

any droplets at 74 mm from the nozzle outlet possibly due to a small change in the

mixture critical point because there is significantly less polymer in the initial

PMMA/ethanol solution than the other solutions.

<u>SAS Particle Characteristics</u>

Particles were collected for PMMA, PMMAVP4, PMMAVP3, PMMAVP1, and

PVP (Table 4.3). At 84 bar, particles of all five polymers were characterized (Figure

4.5). At 94 bar and 101 bar, particles of PMMA, PMMAVP4, and PVP were analyzed

(Figure 4.6 and 4.7). PVP particles were collected at 104 bar, and PMMAVP4 and PVP

particles were collected at 111 bar. Particles of PVP from 84 bar and PMMA at all

conditions exhibited only small particles. For the other polymers and PVP at operating

conditions other than 84 bar, a bimodal particle size distribution was observed with

particle diameters ranging from 0.14 μm to 242 μm. Histograms were developed to study

the bimodal particle size distribution with 0.5 μm bins below 6.5 μm and 10 μm bins

starting at 10 μm until 100 μm (Figures 4.8-4.10). The average particle diameter and

average particle volume of the smaller mode (<6.5 μm) was considered separately from

the larger mode (Figure 4.11).

Saturated solutions of PMMA were processed via SAS at 84 bar, 94 bar, and 101

bar at 323 K (Figure 4.8). At 84 bar and 323 K, the diameters of particles were in the

range of 0.1 μm-2.2 μm with an average of 0.4 μm (Figure 4.11). At 94 bar at 323 K, an

average particle diameter of 0.8 μm with a range of 0.1 μm-3.0 μm was obtained. At 101

bar, PMMA particles with an average diameter of 0.9 μm with a range of 0.1 μm-3.3 μm were collected.

Ethanol solutions containing 1 wt% PMMAVP4 were processed at 84 bar, 94 bar, 101 bar, and 111 bar at 323 K (Figure 4.9). At 84 bar, particles with diameters between 0.24 μm and 241.78 μm were obtained. The distribution of particles appears to be bimodal with the two modes separated at 6.5 μm throughout these experiments. The average particle diameter of the smaller mode (below 6.5 μm) is 1.93 μm (Figure 4.11). At 94 bar, particles with diameters between 0.18 μm and 175.05 μm were collected. The average particle diameter of the smaller mode is 1.57 μm. At 101 bar, the particle diameter range was 0.18 μm to 16.38 μm with 1.10 μm as average particle diameter of the smaller mode. The particle diameter rage at 111 bar was 0.18 μm to 14.10 μm where the average diameter of the smaller mode is 2.10 μm.

The 1 wt% PVP in ethanol solutions were processed at 323K and pressures of 84 bar, 94 bar, 101 bar, 104 bar, and 111 bar (Figure 4.10). At 84 bar, a unimodal particle size distribution was obtained with an average particle diameter of 2.06 μm (Figure 4.11) with a minimum of 0.18 μm and a maximum of 6.30 μm. Larger particles were obtained in preliminary experiments which may be due to fluctuations in the operating conditions, but this result was not observed in the experimental results presented here. At 94 bar a bimodal distribution was obtained with a minimum of 0.36 μm and a maximum of 68.80 μm. The average particle diameter of the smaller mode, below 6.5 μm, is 2.01 μm. At 101 bar, particles with diameters between 0.14 μm and 31.54 μm were obtained. The average particle diameter of the smaller mode is 0.85 μm. When the pressure is increased to 104 bar, the system is nearing the supercritical regime. A particle size range of 0.25

μm to 8.34 μm was obtained. The overall average particle diameter was calculated at 2.06 μm. For particles below 6.5 μm, an average particle diameter of 1.89 was obtained. At 111 bar, particles with diameters between 0.30 μm and 38.00 μm were obtained. The average particle diameter of the smaller mode was 2.49 μm.

Bimodal distributions of PMMAVP1 particles (Figure 4.12) and PMMAVP3 particles (Figure 4.13) from 1 wt% solutions with ethanol were obtained at 323 K and 84 bar. The diameters of PMMAVP1 particles were within the range of 0.56 μm to 95.25 μm with 1.99 μm as the average particle diameter of the smaller mode. The diameters of PMMAVP3 particles have a minimum of 0.21 μm and a maximum of 118.00 μm. The average particle diameter of the smaller mode is 1.45 μm. Particles of PMMAVP1 were collected at 94 bar and 101 bar but the particles melted due to either glass transition temperature reduction during the spray process or exposure to solvent due to insufficient purging after the spray process.

Discussion

The spray characteristics of ethanol solutions being sprayed into carbon dioxide for the presented operating conditions is indicative of a transition from a two phase subcritical system to one phase supercritical system. The jet break up length was shown to decrease with increasing pressure (Figure 4.3). The average droplet diameter initially rapidly increased at all conditions which indicated the initial influx of carbon dioxide (Figure 4.4). As pressure was increased from 84 bar to 101 bar, there was a decrease in the average droplet diameter at 14 mm, 44 mm, and 74 mm from the nozzle outlet (Figure 4.4) indicating that droplets are dissipating closer to the nozzle outlet at the higher

pressure. The average droplet diameters measured for each solution at a given location and operating condition were very similar which illustrates the small difference between each of the solutions. These results show that the different solute in each of the solutions had little effect on the spray characteristics.

Large, hollow microparticles of polyvinyl pyrrolidone (PVP) and poly(methyl methacrylate-co-vinyl pyrrolidone) were obtained when processing these polymers just below the transition from a two phase to a one phase system. These large, hollow microparticles are also known as microballoons. Since these microballoons are transparent it is possible to see that they are hollow using a visual microscope (Figure 4.14a). To characterize the thickness of the microballoon outer shell, 30 microballoons from seven SAS experiments were placed onto SEM stubs. Visual images of the microballoons were obtained using a Nikon 40D CCD camera and a light microscope to confirm that they are hollow (Figure 4.14a). The stubs were then sputter coated with gold and imaged using a Zeiss DSM940 SEM (Figure 4.14b). The stubs were removed from the SEM, and tweezers were used to crush each of the microparticles. The stubs were again sputter coated with gold, and the crushed particles were imaged using the SEM (Figure 4.14c). Microballoons of PMMAVP4 processed at 84 bar and 50°C and PVP processed at 94 bar and 50°C were measured to obtain an average shell thickness of 15 μm with a standard deviation of 6 μm. This method allowed for the thickness of the microballoon shell to be determined.

A bimodal particle distribution was observed for PVP at 94 bar, 101 bar, and 104 bar; PMMAVP1 at 84 bar; PMMAVP3 at 84 bar; and PMMAVP4 at 84 bar, 94 bar, and 101 bar (Figure 4.10-13). The bimodal distribution is characterized by a small mode with

solid particles below 6.5 μm in diameter and a large mode with solid particles and microballoons between 6.5 μm and 300 μm in diameter. There appears to be a relation between solute solubility and the percent of particles counted in each mode as plotted in Figures 4.15 and 4.16 which show the number and volume, respectively, of PVP and PMMAVP4 particles in the small and large modes for each processing pressure. The percent of PVPMMA4 particles in the large mode is 9 % at 84 bar, 20 % at 94 bar, 2 % at 101 bar, and 1 % at 111 bar. The percent of PVP particles in the large mode is 0 % at 84 bar, 4 % at 94 bar, 2 % at 101 bar, 1 % at 104 bar, and 22 % at 111 bar. Large particles and microballoons of PMMAVP4 are formed at lower pressures than large particles and microballoons of PVP. According to the cloud point data, PMMAVP4 precipitates at a lower CO_2 concentration from CO_2-expanded ethanol than PVP (Table 1). This data indicates that the particles and microballoons which are characteristic of the large mode can be formed at lower pressures when the polymer is less soluble in the solvent.

The small mode can be analyzed independently by plotting the average particle diameters of particles below 6.5 μm (Figure 4.11). A minimum average particle diameter for PVP is observed at 101 bar. The average particle diameter of PMMAVP4 is slightly lower than PVP at 84 bar and 94 bar, but at 101 bar the average particle diameter of PVP is 0.25 μm larger the that of PMMAVP4. At pressures greater than 101 bar PVP particles were observed to increase in size. This may be due to operating conditions which are near or surpass the glass transition of PVP as demonstrated in Gong et al. (2005) which showed that PVP is plasticized by CO_2 at 150 bar and 75°C. Therefore the increase in particle size may be due to the malleability of the polymer rather than an effect of the mass transfer in the supercritical phase. Particles of PMMAVP4 at 111 bar are also

larger when compared to 101 bar but are smaller than the PVP particles. The minimum

average droplet diameter of the small mode was obtained when the jet break up

transitions from atomization to break up as a gas-like plume.

Tables

Polymer	M_{MMA}	M_{VP}	dm_{MMA}/dm_{VP}	m_{MMA}	m_{VP}	Filtered	Cloud Point Pressure (bar)
PVP	NA	NA	NA	0	1	No	94
PMMAVP1	0.10	0.90	0.62	0.38	0.62	No	92
PMMAVP3	0.30	0.70	2.02	0.67	0.33	Yes	87
PMMAVP4	0.40	0.60	3.01	0.75	0.25	Yes	88
PMMA	NA	NA	NA	1	0	NA	NA

Table 4.1 Theoretical monomer ratio and cloud point pressure for polymers used in SAS experiments where M_{MMA} is the moles of methyl methacrylate in the reaction solution, M_{VP} is the moles of vinyl pyrrolidone in the reaction solution, dm_{MMA}/dm_{VP} is the theoretical molar ratio of methyl methacrylate to vinyl pyrrolidone groups in the polymer, m_{MMA} is the theoretical fraction of methyl methacrylate in the polymer, and m_{VP} is the theoretical fraction of vinyl pyrrolidone in the polymer.

Polymer	CO$_2$ Conditions			Distance from Nozzle (mm)	Average Droplet Diameter (μm)	Standard Deviation (μm)	Droplets per Image	# of Droplets Measured	Jet Break Up Length (μm)	Standard Deviation of Jet Length (μm)	Measured Jet Images
	Temp (K)	Density (g/cm^3)	Pressure (bar)								
PVP	323	0.24	84	0					870	NA	NA
				3	37	10	4.5	994			
				7	94	52	5.0	995			
				14	116	69	3.4	780			
				44	152	98	2.7	976			
				74	125	87	2.8	984			
PVP	323	0.32	94	0					510	60	189
				3	74	29	6.6	997			
				7	101	51	10.0	1008			
PVP	323	0.44	104	0					260	30	754
PVP	323	0.52	111	0					220	30	146

Table 4.2(a) Statistical data of analyzed results from high magnification visualizations of PVP.

Polymer	CO$_2$ Conditions			Distance from Nozzle (mm)	Average Droplet Diameter (μm)	Standard Deviation (μm)	Droplets per Image	# of Droplets Measured	Jet Break Up Length (μm)	Standard Deviation of Jet Length (μm)	Measured Jet Images
	Temp (K)	Density (g/cm^3)	Pressure (bar)								
PMMAVP 1	323	0.24	84	0					1120	129	444
				3	62	33	3.8	1060			
				7	97	58	4.4	1008			
				14	135	98	2.9	857			
				44	182	109	2.2	691			
				74	210	108	1.7	252			
PMMAVP 1	323	0.32	94	0					560	46	208
				3	88	38	4.2	1059			
				7	103	51	8.1	1734			
				14	114	62	7.7	1563			
				44	147	78	3.9	1000			
				74	156	94	2.3	326			
PMMAVP 1	323	0.40	101	0					460	55	215
				3	59	21	5.7	770			
				14	121	49	4.4	237			
				44	143	76	2.0	290			
				74	139	63	1.8	100			

Table 4.2(b) Statistical data of analyzed results from high magnification visualizations of PMMAVP1.

Polymer	CO₂ Conditions			Distance from Nozzle (mm)	Average Droplet Diameter (μm)	Standard Deviation (μm)	Droplets per Image	# of Droplets Measured	Jet Break Up Length (μm)	Standard Deviation of Jet Length (μm)	Measured Jet Images
	Temp (K)	Density (g/cm³)	Pressure (bar)								
PMMAVP4	323	0.24	84	0					670	40	443
				3	72	34	4.3	1004			
				14	119	81	3.7	1000			
				44	160	95	2.0	577			
PMMAVP4	323	0.32	94	0					440	33	424
				3	80	31	6.8	1041			
				14	102	48	7.3	1003			
				44	152	72	2.8	839			
				74	138	72	3.0	838			
PMMAVP4	323	0.40	101	0					255	36	435
				3	83	25	2.4	417			
				14	98	40	3.7	584			
				44	106	50	2.6	371			
				74	113	47	1.7	148			
PMMAVP4	323	0.52	111	0					190	30	449

Table 4.2(c) Statistical data of analyzed results from high magnification visualizations of PMMAVP4.

Polymer	CO$_2$ Conditions			Distance from Nozzle (mm)	Average Droplet Diameter (μm)	Standard Deviation (μm)	Droplets per Image	# of Droplets Measured	Jet Break Up Length (μm)	Standard Deviation of Jet Length (μm)	Measured Jet Images
	Temp (K)	Density (g/cm^3)	Pressure (bar)								
PMMA	323	0.24	84	0					780	64	71
				3	57	35	7.2	801			
				7	84	36	11.9	808			
				14	149	96	7.6	721			
				44	155	92	4.8	423			
				74	221	124	2.6	292			
PMMA	323	0.32	94	0					320	53	106
				3	30	14	8.9	758			
				7	79	33	6.8	559			
				14	109	56	13.1	928			
				44	161	70	5.2	485			
				54	206	94	3.7	349			
				64	181	75	NA	222			
				74	175	60	NA	175			
PMMA	323	0.40	101	0					230	27	111
				3	61	25	7.32	732			
				7	78	30	4.4	529			
				14	106	35	7.0	744			
				44	109	44	4.6	703			

Table 4.2(d) Statistical data of analyzed results from high magnification visualizations of PMMA.

Polymer	CO$_2$ Conditions		Average Particle Diameter (μm) (below 6.5 μm)	Standard Deviation (μm)	Bimodal	# of Particles Measured
	Density (g/cm^3)	Pressure (bar)				
PVP	0.24	84	2.1	1.1	No	427
	0.32	94	2.0	1.2	Yes	420
	0.40	101	0.9	1.0	Yes	828
	0.44	104	1.9	1.1	Yes	1348
	0.52	111	2.5	1.6	Yes	4329
PMMAVP1	0.24	84	2.0	1.1	Yes	380
PMMAVP3	0.24	84	1.5	1.2	Yes	1172
PMMAVP4	0.24	84	1.9	1.3	Yes	3368
	0.32	94	1.6	1.1	Yes	5082
	0.40	101	1.1	0.7	Yes	310
	0.52	111	2.1	1.1	Yes	9769
PMMA	0.24	84	0.4	0.2	No	NA*
	0.32	94	0.8	0.5	No	NA*
	0.40	101	0.9	0.5	No	NA*

Table 4.3 Particle size measurements from SEM analysis for particles produced at an operating temperature of 323 K. The PMMA measurements (*) were obtained by Sullivan (2007).
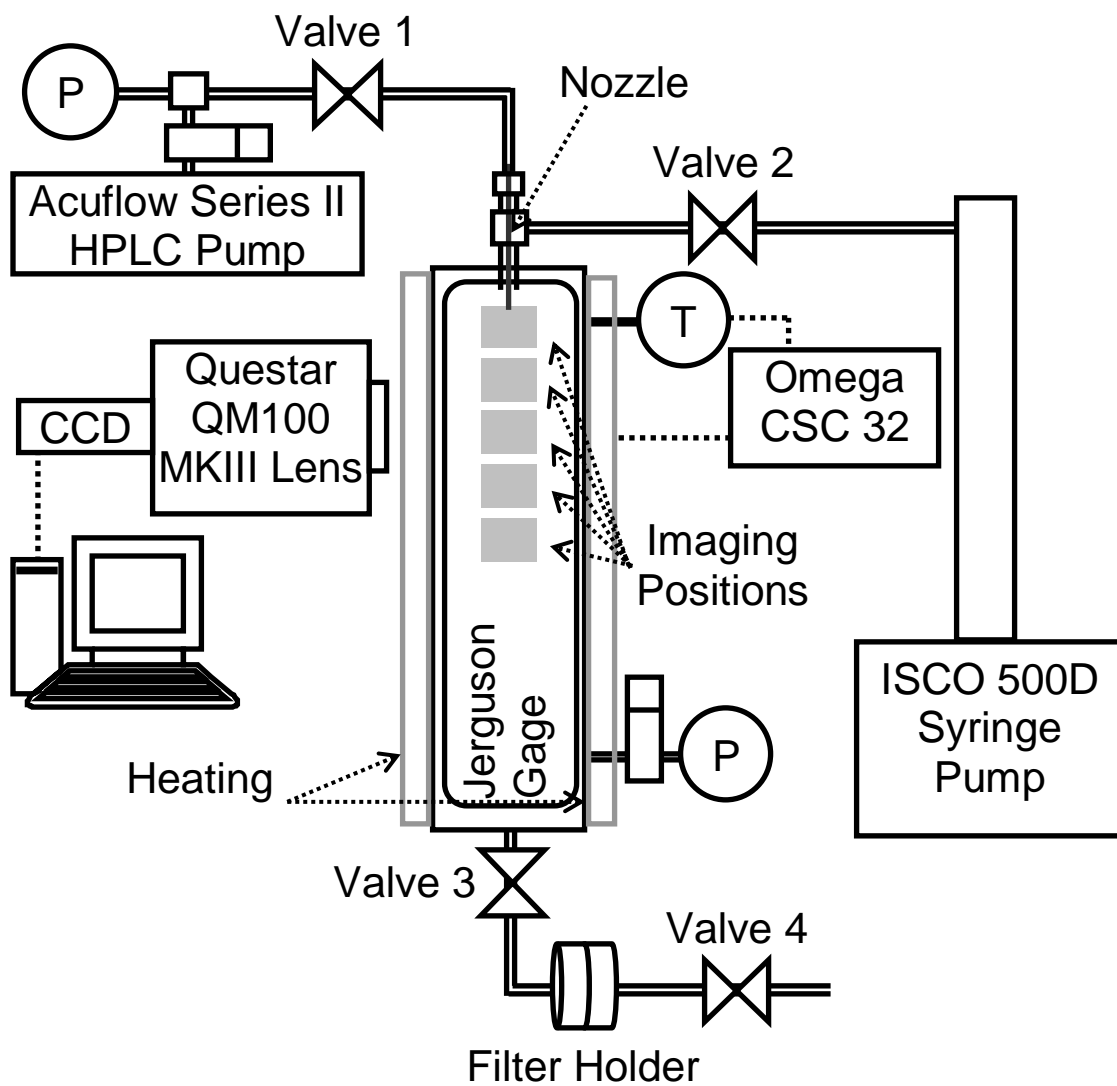
Figure 4.1 Diagram of the imaging system and the apparatus used to perform the supercritical antisolvent precipitation process. The positions imaged in the spray are represented by the shaded boxes inside the Jerguson gage.
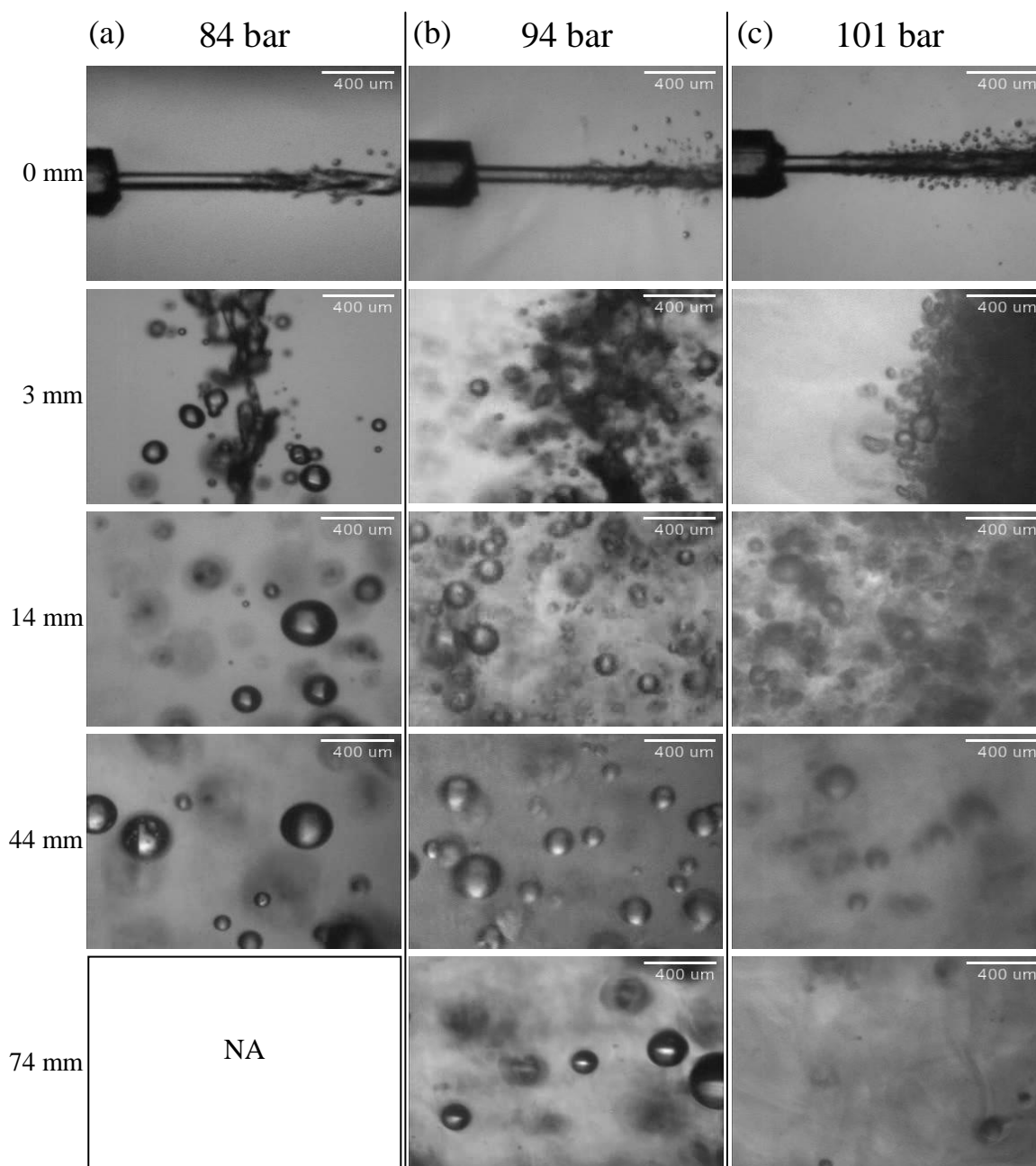
Figure 4.2 Selected frames taken from movies of the spray at given distances from the nozzle. These images are taken from experiments performed at a temperature of 323 K and noted pressures with a 1 wt% PMMAVP4/ethanol solution flow rate of 1.6 mL/min.
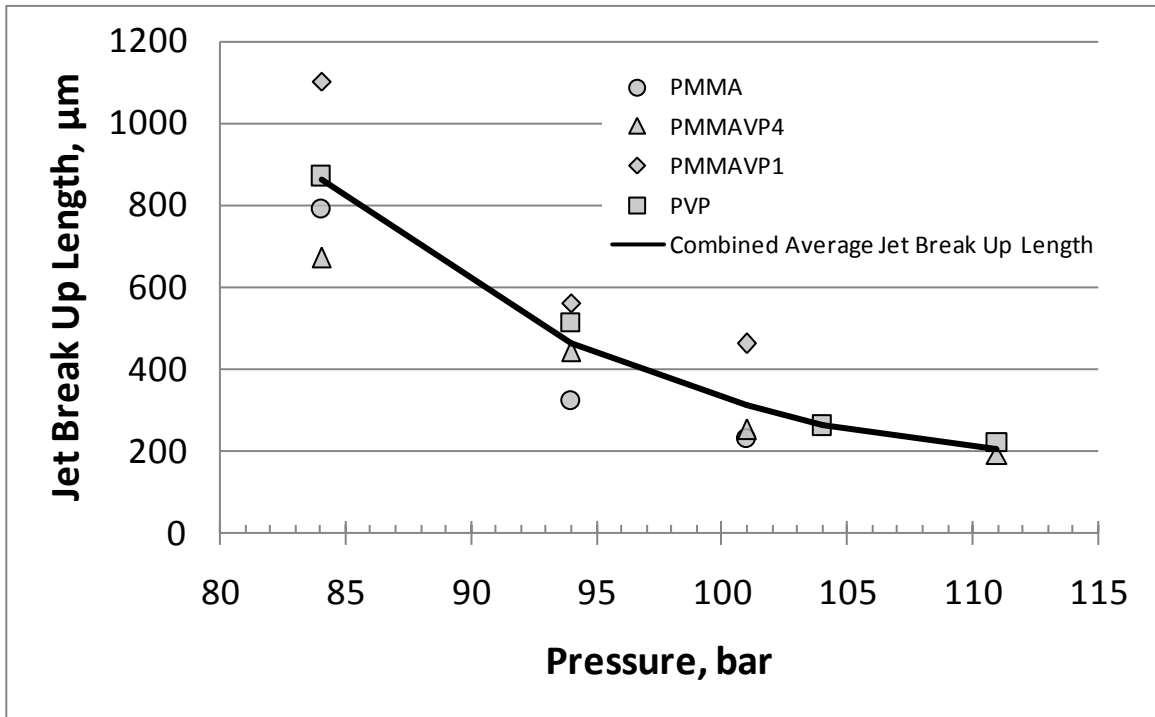
Figure 4.3 Average jet breakup lengths from SAS experiments performed at 323 K and select pressures with ethanol solutions at a flow rate of 1.6 mL/min.
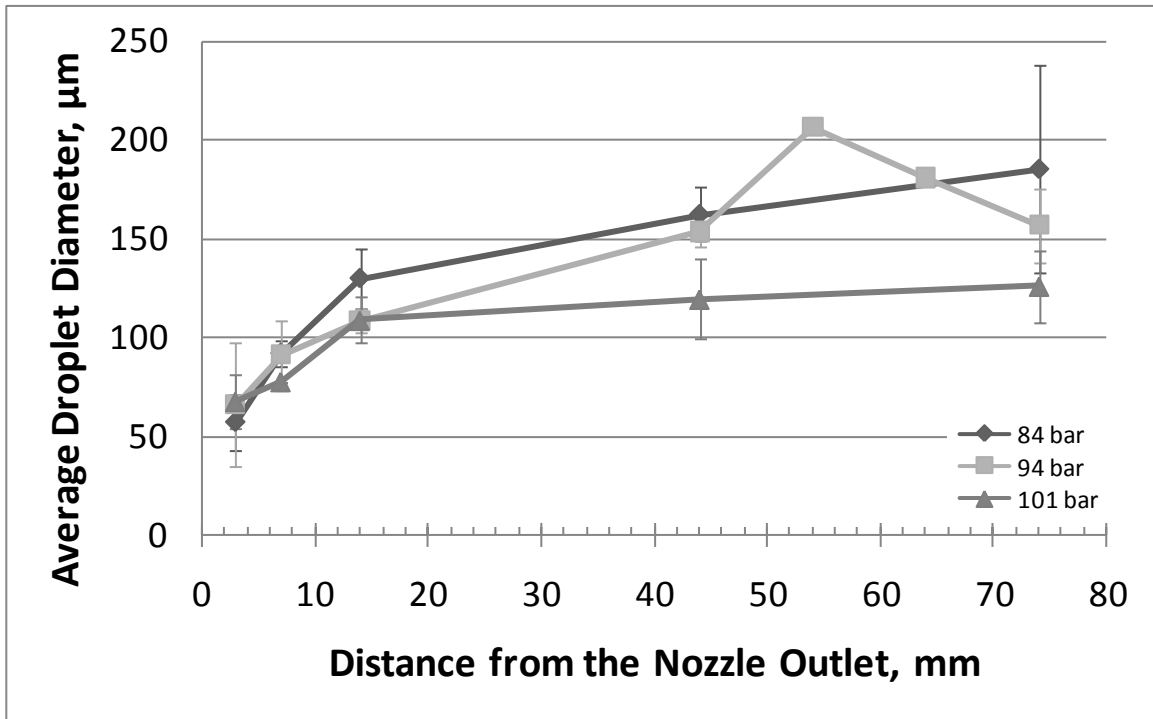
Figure 4.4 The average droplet diameters at several distances from the nozzle outlet from

SAS experiments performed at 323 K and select pressures with ethanol solutions at a

flow rate of 1.6 mL/min.
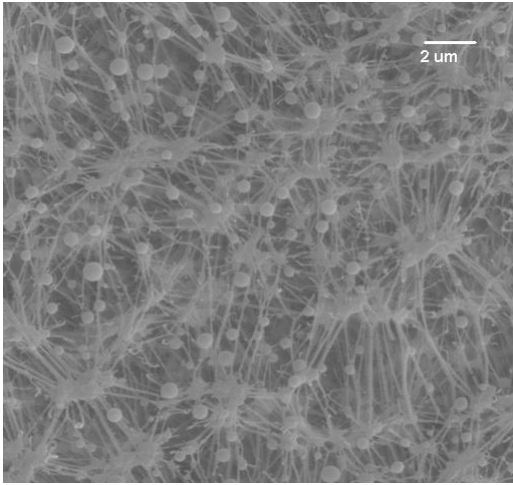
(a) PMMA
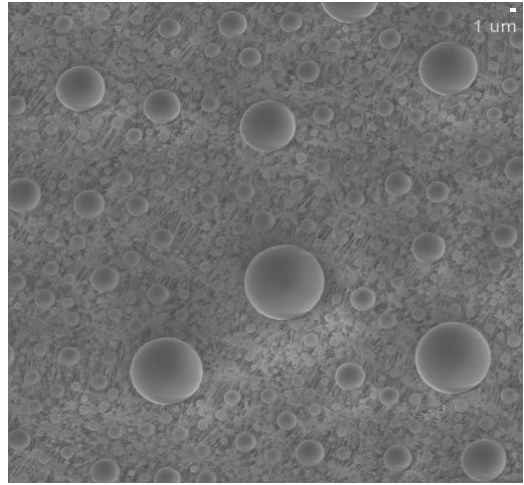
(c) PMMAVP1
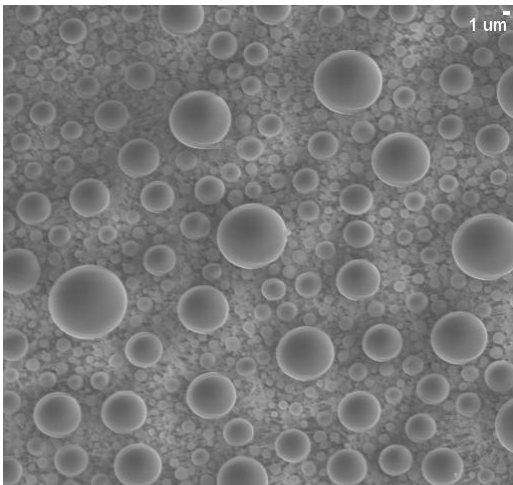
(b) PMMAVP4
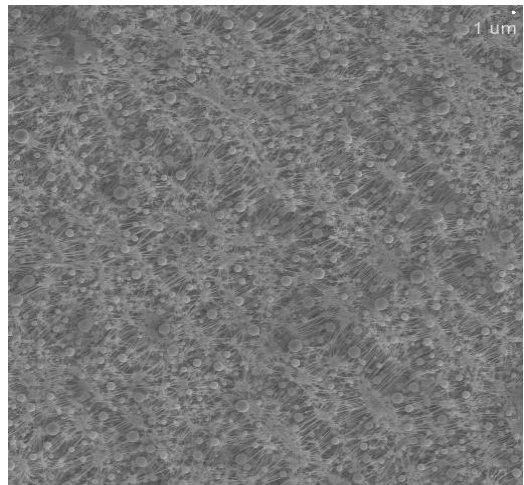
(d) PVP

Figure 4.5 SEM images of polymer particles, (a) PMMA x5000, (b) PMMAVP4 x1000, (c) PMMAVP1 x1000, and (d) PVP x1000, produced from the SAS precipitation process at 84 bar and 323 K.
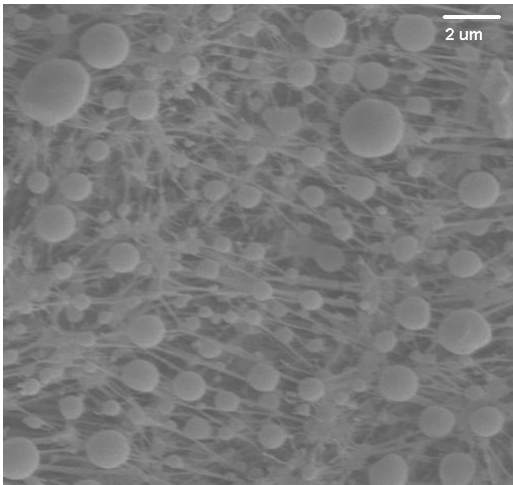
(a) PMMA
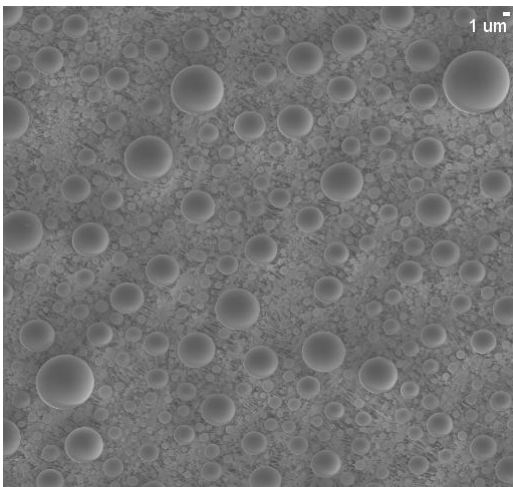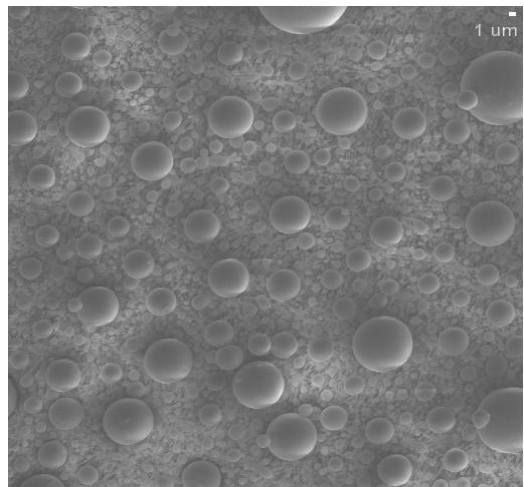
(b) PMMAVP4

(c) PVP

Figure 4.6 SEM images of polymer particles, (a) PMMA x5000, (b) PMMAVP4 x1000,

and (c) PVP x1000, produced from the SAS precipitation process at 94 bar and 323 K.
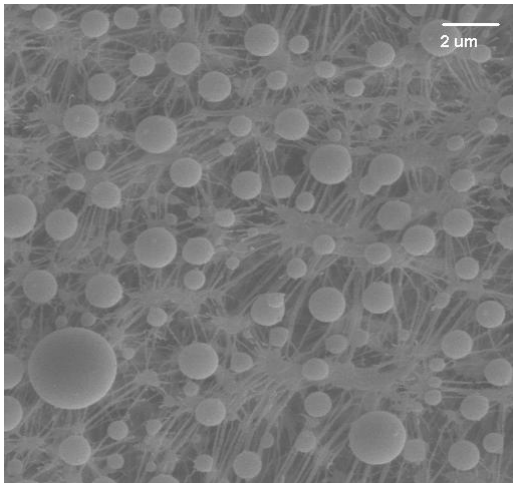
(a) PMMA
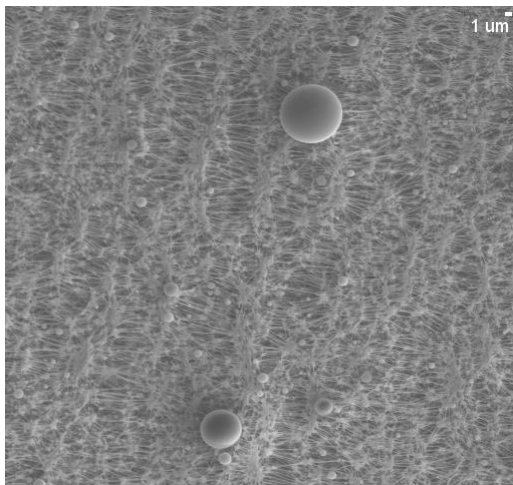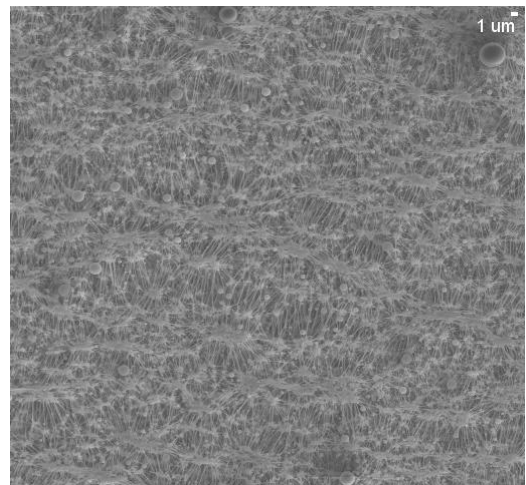
(b) PMMAVP4

(c) PVP

Figure 4.7 SEM images of polymer particles, (a) PMMA x5000, (b) PMMAVP4 x1000,

and (c) PVP x1000, produced from the SAS precipitation process at 101 bar and 323 K.
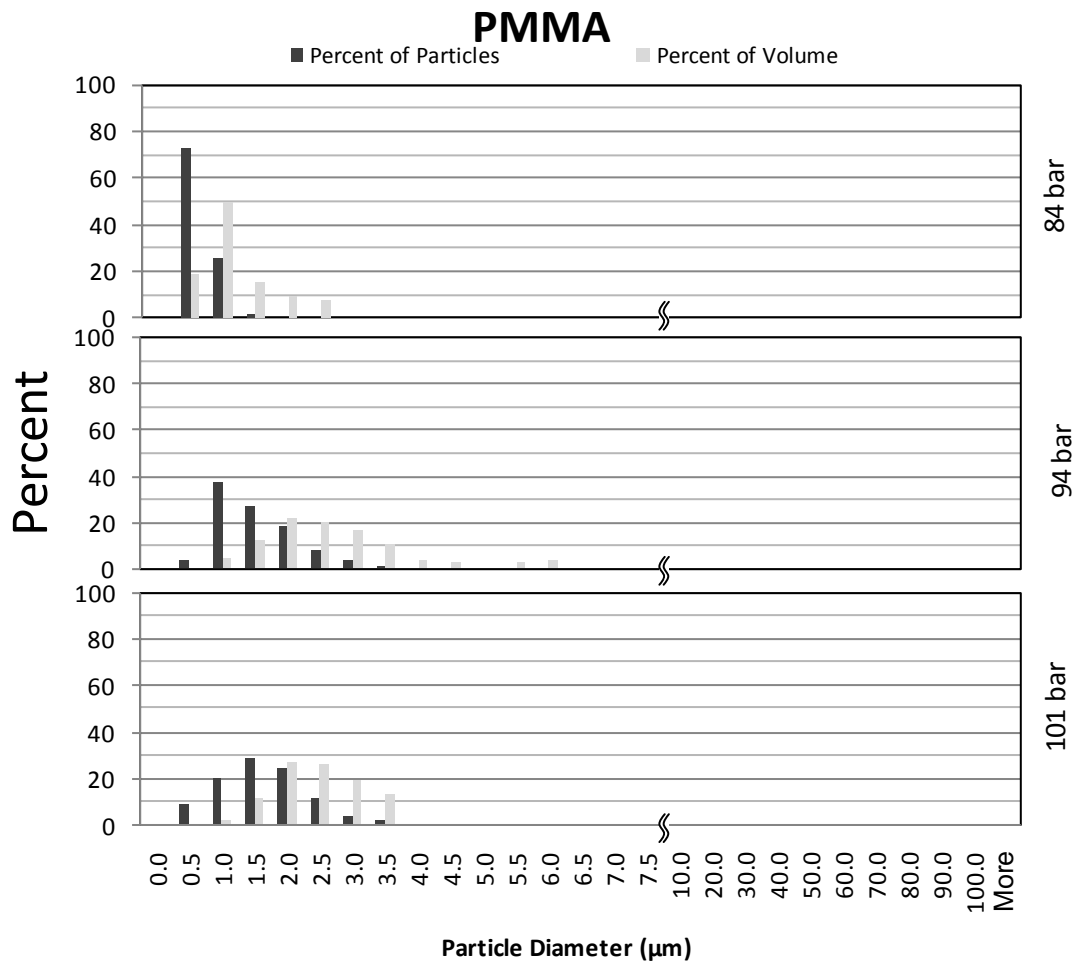
Figure 4.8 Histogram of particles collected from SAS experiments performed at 323 K and select pressures with saturated PMMA/ethanol solutions at a flow rate of 1.6 mL/min.
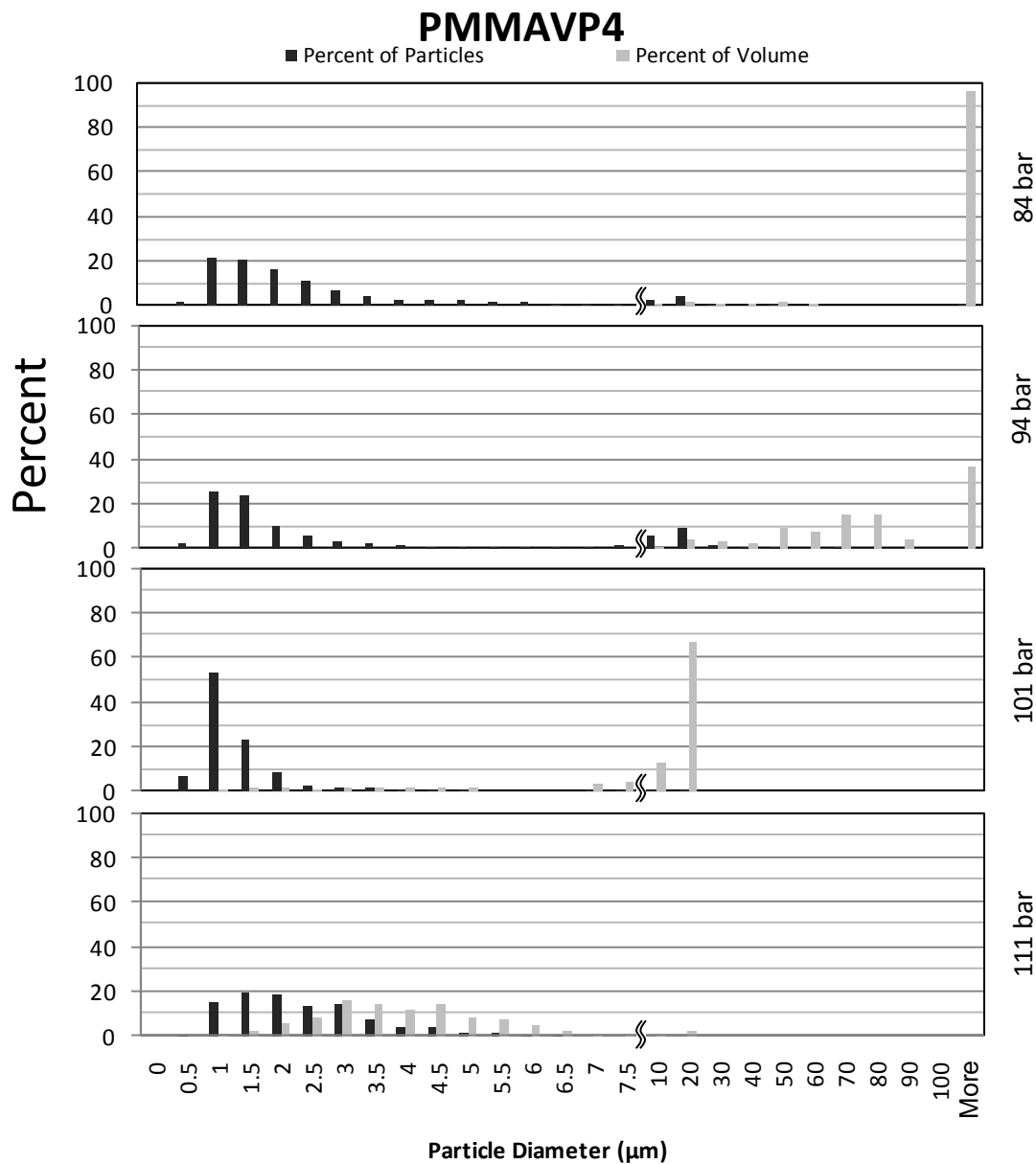
Figure 4.9 Histogram of particles collected from SAS experiments performed at 323 K and select pressures with 1 wt% PMMAVP4/ethanol solutions at a flow rate of 1.6 mL/min.
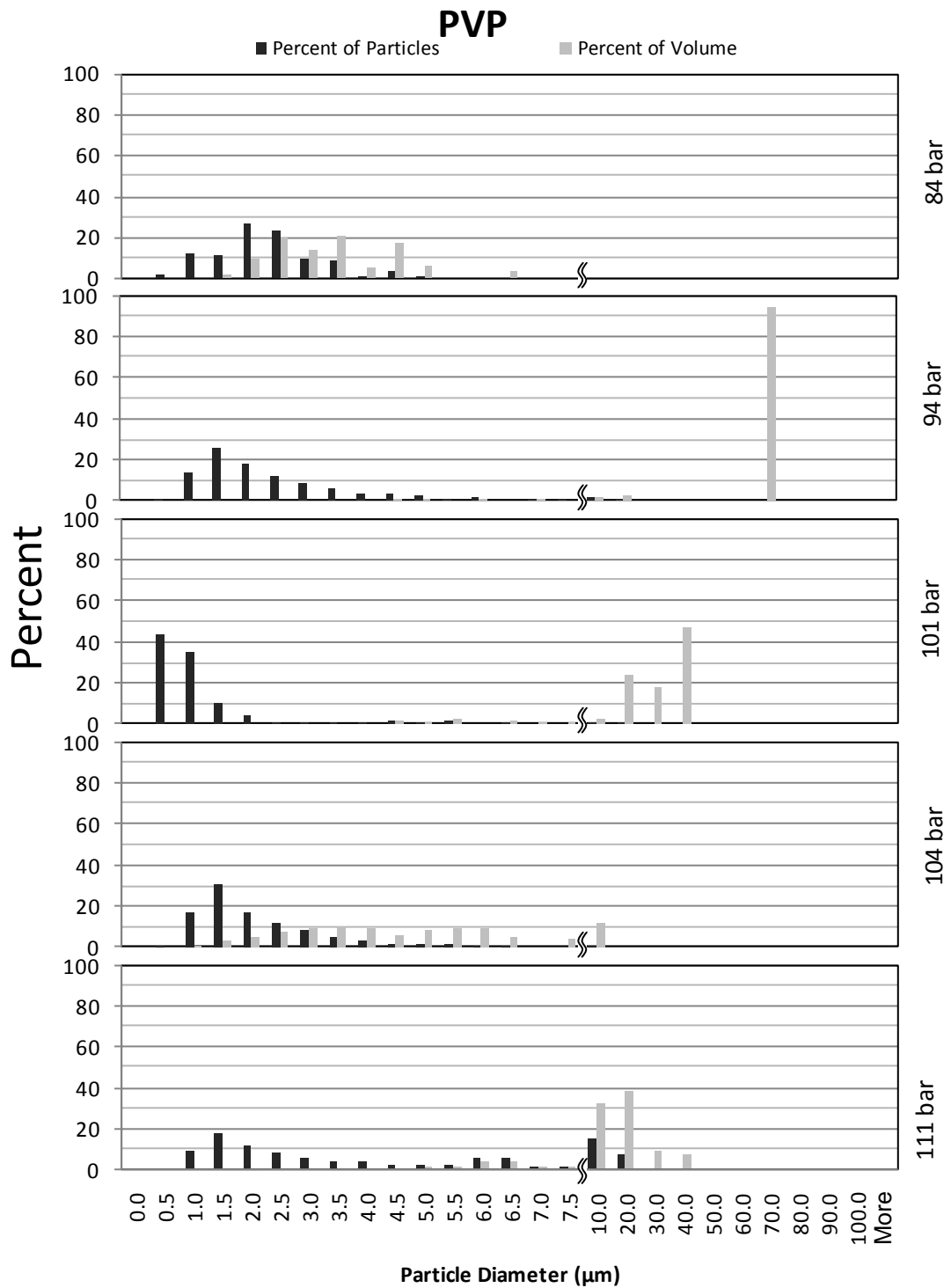
Figure 4.10 Histogram of particles collected from SAS experiments performed at 323 K and select pressures with 1 wt% PVP/ethanol solutions at a flow rate of 1.6 mL/min.
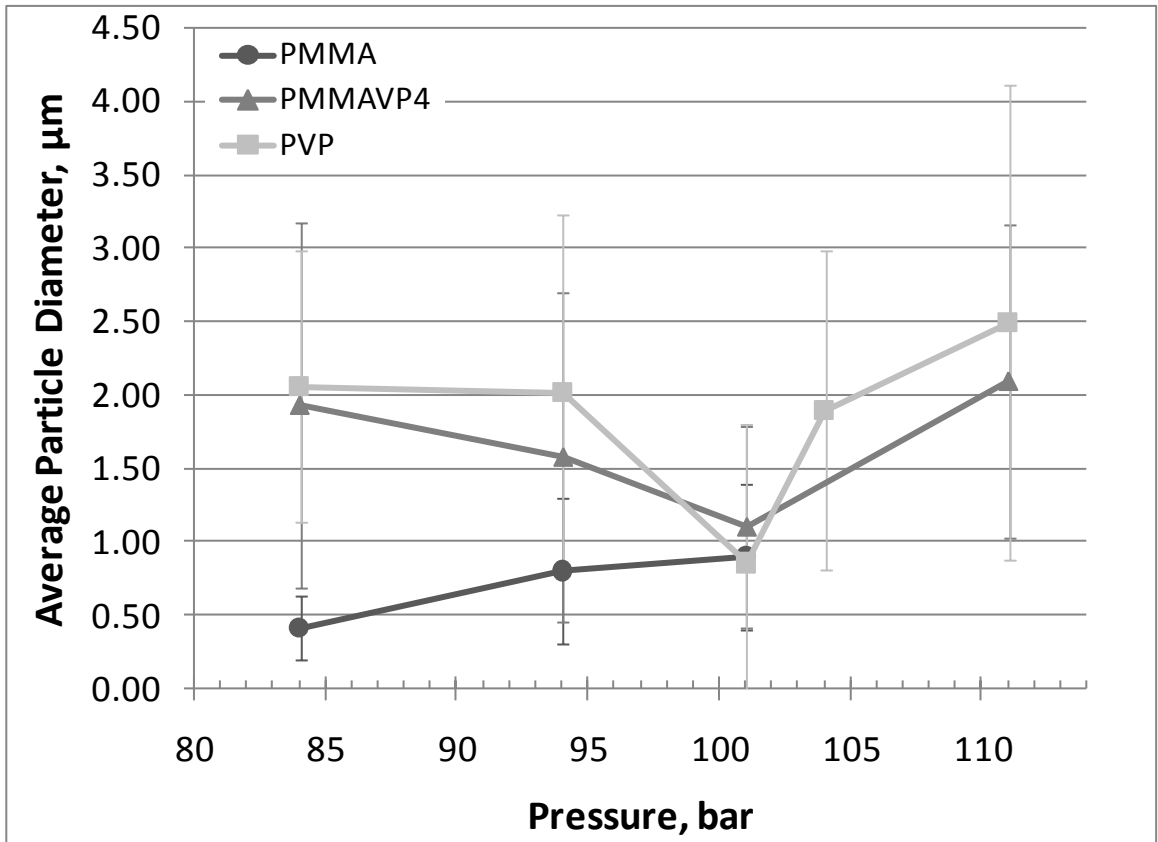
Figure 4.11 The average diameter for particles in the small mode (below 6.5 µm) from

SAS experiments performed at 323 K and select pressures with ethanol solutions at a

flow rate of 1.6 mL/min.
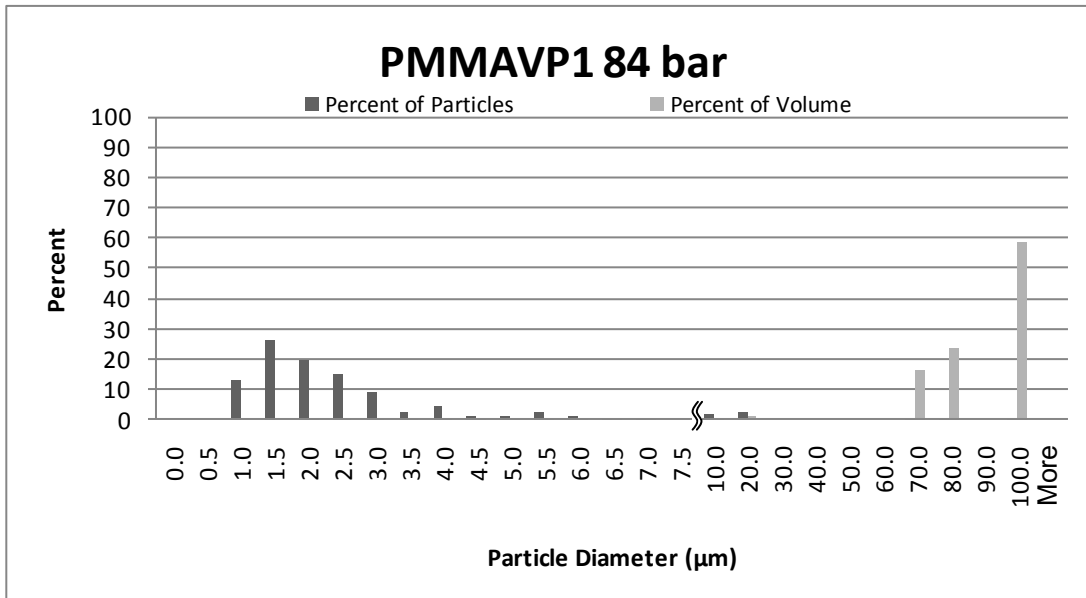
Figure 4.12 Histogram of particles collected from SAS experiments performed at 323 K and select pressures with 1 wt% PMMAVP1/ethanol solutions at a flow rate of 1.6 mL/min.
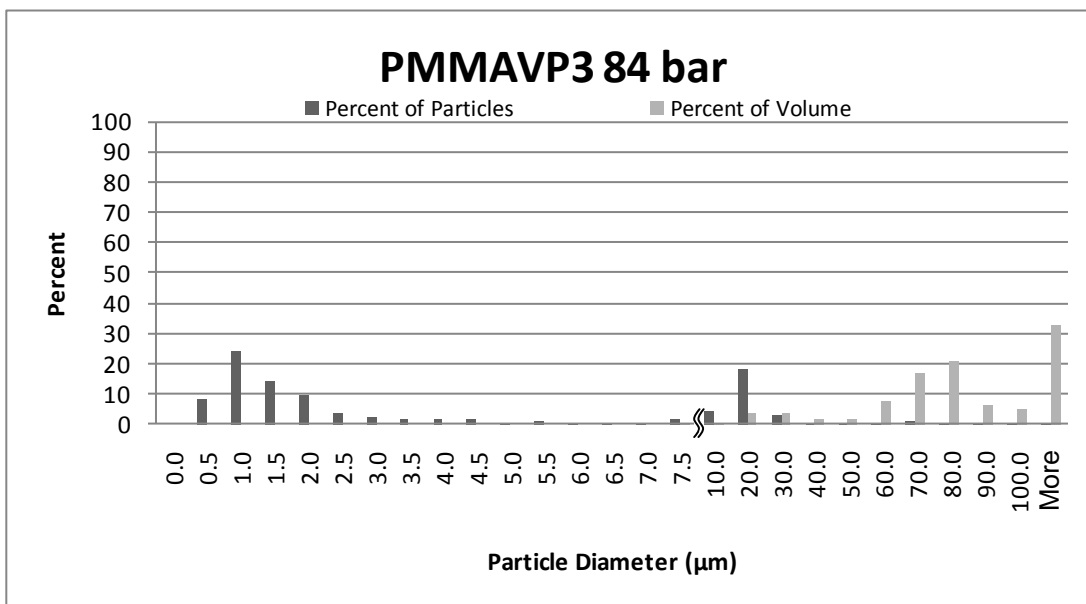
Figure 4.13 Histogram of particles collected from SAS experiments performed at 323 K

and select pressures with 1 wt% PMMAVP3/ethanol solutions at a flow rate of 1.6
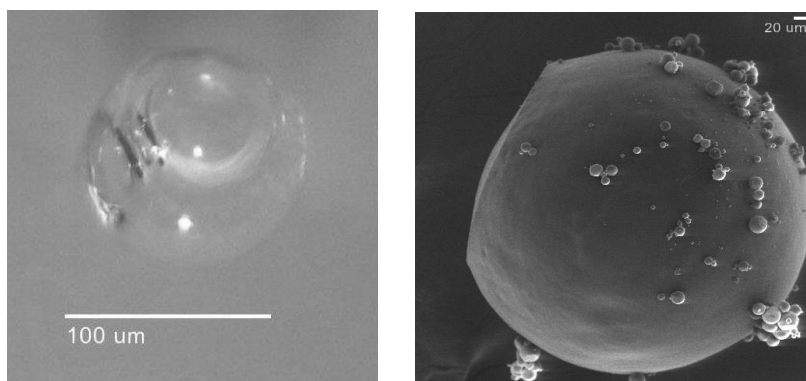
mL/min.

(a)

(b)
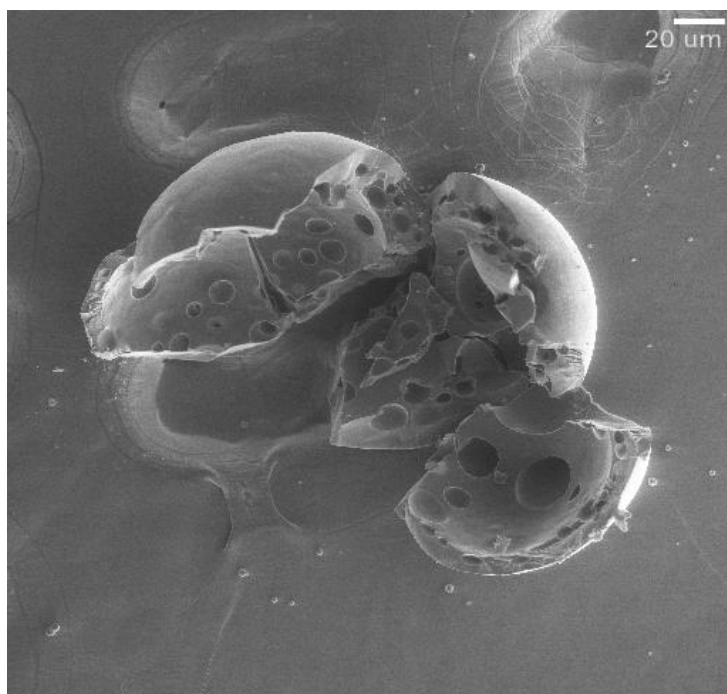
(c)

Figure 4.14 Representative images of microballoons produced via SAS from experiments at 323 K and 84 bar with 1 wt% polymer/ethanol solutions at a flow rate of 1.6 mL/min. To characterize the microballoons three types of images were obtained: (a) visual microscope image of PMMAVP1, (b) SEM image of a PMMVP4 microballoon, and (c) SEM image of the PMMAVP4 particle shown in (b) after crushing.
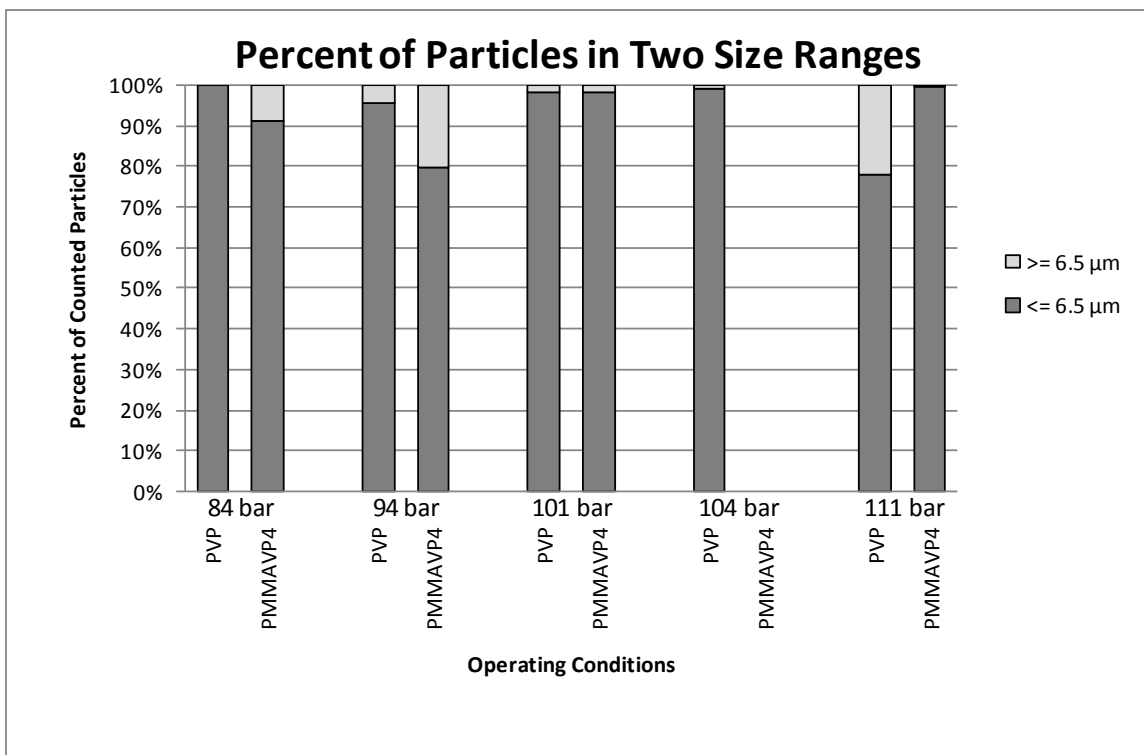
Figure 4.15 Particles sorted into two size ranges from SAS experiments performed at 323 K and select pressures with 1 wt% PVP or 1 wt% PMMAVP4/ethanol solutions at a flow rate of 1.6 mL/min.
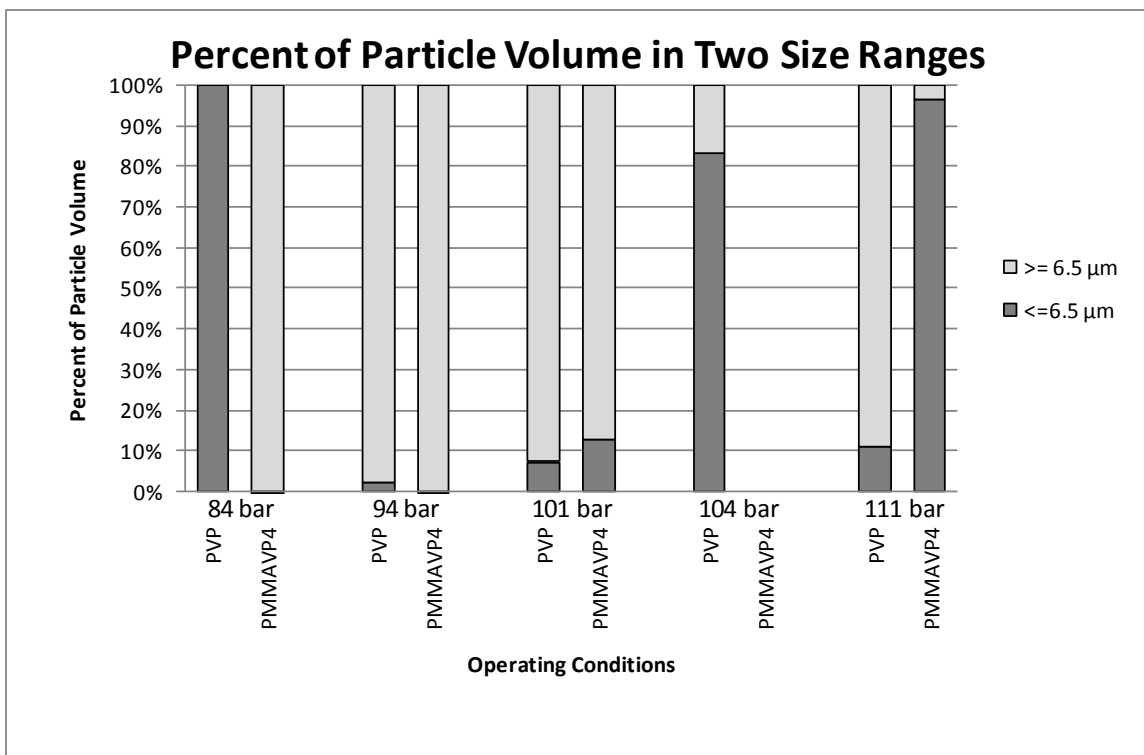
Figure 4.16 Volume of particles sorted into two size ranges from SAS experiments performed at 323 K and select pressures with 1 wt% PVP or 1 wt% PMMAVP4/ethanol solutions at a flow rate of 1.6 mL/min.

5. Feasibility of a Supercritical Closed-Loop Thermosyphon Precipitation Process

Introduction

Carbon dioxide can be either a solvent or antisolvent depending on the solute and operating condition. Carbon dioxide is a feeble (Beckman 2004) but tunable solvent, so it is possible to change the saturation concentration of a solute by changing the operating conditions (McHugh and Krukonis 1994). There are numerous processes which utilize the tunability of carbon dioxide to produce micro- and nano-scale particles (Reverchon and Adami 2006). Supercritical antisolvent (SAS) precipitation and gas antisolvent (GAS) precipitation use supercritical carbon dioxide as an antisolvent to lower the strength of a solvent which causes precipitation of a solute (Randolph et al. 1993). On the other hand, rapid expansion of a supercritical solvent (RESS) utilizes supercritical carbon dioxide as the solvent to dissolve the solute. The carbon dioxide and the solute are rapidly expanded to atmospheric pressure through a nozzle to rapidly lower the solvent strength of carbon dioxide (Matson et al. 1987). These processes have been shown to produce particles of a variety of substances, but each process has strengths and weaknesses. A new process was developed in this work that uses carbon dioxide as the sole processing fluid, but, unlike RESS, carbon dioxide is continuously recycled at a constant pressure. The presented thermosyphon precipitation process (Figure 5.1) uses cold, high density carbon dioxide to dissolve a substance and hot, low density carbon dioxide to supersaturate the substance. The carbon dioxide and solute are contained

inside a loop with two temperature zones, and flow between the hot zone and the cold zone is driven by buoyant effects due the density differential.

Background

A system where flow is driven by buoyancy is classified as a thermosyphon (Lock 1992). The classical make up of a thermosyphon is a pipe or, as used in these experiments, a loop which is filled with some type of working fluid: gas, liquid, or both. A density difference in the working fluid is induced by having two energy transfer zones. One zone is a heat sink while the other is a heat source. Flow is induced when buoyant forces cause the higher density portion of the fluid to flow down towards the lower density portion of the fluid or, conversely, the lower density portion of the fluid flows up to the higher density portion of the fluid. The main advantage of a thermosyphon is that no mechanical energy is necessary to induce flow of a fluid in a system.

The Perkins tube, developed in the early 1860's to transfer heat from a furnace to a remote area, was the first industrial use of thermosyphons (Lock 1992). Thermosyphons have been used for various purposes since the Perkins tube including applications related to solar energy (Enibe 2003), nuclear reactor cooling (Mousavian et al. 2004), and electronics cooling (Chu et al. 1999). Various studies have examined thermosyphons with supercritical fluids as the working fluid. Studies with supercritical water were performed to model cooling systems of nuclear reactors (Chatoorgoon 2001). A model for a heat exchanger with carbon dioxide as the working fluid was developed (van der Kraan et al. 2005). Also, a thermosyphon was developed to perform

106

supercritical fluid extraction using supercritical carbon dioxide as the working fluid (Yoshikawa et al. 2005).

The supercritical fluid extraction study by Yoshikawa et al. (2005) provides experimental and modeling results on the use of supercritical carbon dioxide as the working fluid for a closed-loop thermosyphon. The flow of carbon dioxide was measured using time-dependent UV detection of an acetone tracer. Flow rates of carbon dioxide between 0.8 to 4 m/min were produced by altering the pressure, temperature, and the mass of carbon dioxide loaded into the system. Operating conditions ranged from 78 to 120 bar, 15 to 55°C, and 0.55 to 0.80 g/mL. The system was predicted to have an increased velocity with an increasing density difference between the hot and cold zones. The carbon dioxide was shown to extract the desired substance in the hot zone and then the substance precipitated from the fluid in the cold zone.

Precipitation is driven by the dependence of carbon dioxide solvent strength on density which is dependent on temperature and pressure. Nucleation of the solute will occur due to supersaturation by lowering the solubility. Depending on the kinetics of the system, higher supersaturation usually results in faster nucleation and smaller particles (Randolph and Larson 1988). The solubility of substances in carbon dioxide decreases as the temperature increases isobarically at pressures below the cross-over pressure (Figure 5.2) (Mukhopadhyay 2000). The cross-over pressure is defined as the pressure at which the solubility of a substance within a fluid switches from increasing with temperature to decreasing with temperature. Due to the variation in solubility, a solute can be dissolved at a cold temperature and precipitated at a hot temperature. The supersaturation in the hot zone will depend on the difference between the hot and cold zone saturation

concentrations and the efficiency of dissolution in the cold zone. The level of supersaturation in the hot zone can be used to predict characteristics of the resulting particles.

Presented Thermosyphon Precipitation Process

This study uses the solvent properties of carbon dioxide in a cold zone to dissolve a solute and a hot zone to induce precipitation. The process is performed in a closed-loop thermosyphon of which the initial design is described in detail below (Figure 5.3). The substance to be processed is placed in the cold zone of the loop. Two temperature zones are maintained using hot and cold water baths. After the temperature zones are stabilized, the loop is pressurized with carbon dioxide. The operating pressure must be below the cross-over pressure for the solubility of the solute in carbon dioxide to be lower in the cold zone. The solute in the cold zone then dissolves into the carbon dioxide, and the density differential induces flow of the carbon dioxide. The flow of the fluid carries the solute into the hot zone where precipitation occurs. The pressure and temperatures at which to operate the thermosyphon are determined by the solubility of the substance in carbon dioxide.

The thermosyphon process presented in this paper has several advantages over other methods used to make microparticles. Since organic solvents are not used, there is no possibility of the collected particles being contaminated with residual solvent, and potential harmful contamination of the environment is reduced. Also, there is no rapid depressurization of the solute, so sensitive particles can be processed using this method. To operate the process, mechanical pumps are only necessary for the initial pressurization

and final depressurization. There are two main disadvantages of the process. The time to fully process a solute sample could be quite large, but careful design of the system should be able to overcome this difficulty. There are a limited number of solutes which can be dissolved by pure carbon dioxide. Adding a cosolvent, as has been done in RESS (Thakur and Gupta 2005), could expand the number of potential solutes. Developing this process will provide a safe, economical, and green option to produce microparticles of a solute.

The thermosyphon is expected to process a solute sample into micro- or nano-scale particles. The volumetric flow rate is expected to increase with an increasing hot to cold zone carbon dioxide density difference. The time for a solute sample to be processed should decrease as the pressure increases. Particle size is expected to vary relative to the solubility of the substance in carbon dioxide within the hot and cold zones. A lower solubility in the hot zone should result in smaller particles, since higher supersaturation usually results in faster nucleation and smaller particles (dependent on system kinetics) (Randolph and Larson 1988).

To evaluate the process, two thermosyphon systems were designed, built, and operated to allow supercritical carbon dioxide to flow within a loop that has two temperature zones. A side-by-side hot and cold zone system (Figure 5.3) was first built and tested. The initial configuration was modified to improve the flow rate and precipitation characteristics (Figure 5.5). Naphthalene was chosen as the solute to test the system. The temperatures and pressure (Table 5.1) at which to test the system were chosen to maximize the amount of naphthalene which dissolves and then precipitates. Collected particles were analyzed using a light microscope. The process was visualized

with a high speed camera and lens to show carbon dioxide and naphthalene exiting the nozzle into the precipitation chamber.

Experimental

Materials

Naphthalene 99% was obtained from Sigma-Aldrich. Carbon dioxide (grade 5.5) was obtained from Airgas. All materials will be used as received.

Initial Apparatus

The initial apparatus consisted of a loop with two temperature zones as shown in Figure 5.3. The hot temperature zone is maintained using a circulating water heater, Fisher Scientific Isotemp Immersion Circulator Model 730, and the cold temperature zone is maintained using water heater/chiller, Fisher Scientific Model 9510. The fittings in the loop are connected with 1/16" O.D. stainless steel tubing. A blowout plug, HIP 15-63AF1, with a maximum pressure of 3500 psia is located at the top of the ambient middle section. Going clockwise around the loop, tubing goes through a rubber stopper into the cold temperature section. T-connector 1 connects a pressure gauge to the system through the top port. The lower port of T-connector 1 continues the path of the loop. A microreactor, HiP, contains the unprocessed solute. Three metal screens above and below the unprocessed solute contain the substance. Below the microreactor, a bend turns the stainless steel tubing toward the hot zone. Union 1, Valco from Alltech #30715, connects the stainless steel tubing to 100 μm I.D. capillary tubing, Alltech 602036. The capillary tubing is inserted inside Union 2, HiP 15-21AF1AF2. Stainless steel tubing,

1/8", threaded with capillary tubing then passes through the middle ambient temperature zone and enters the hot temperature zone. The stainless steel tubing terminates at the inlet port of the precipitation chamber. The capillary tubing extends approximately 1 cm into the precipitation chamber which is a Jerguson Gage 5TM40. Downstream of the precipitation chamber, a bend directs the stainless steel tubing upwards. Union 3 is downstream of the precipitation chamber to allow for future flexibility with the loop. The tubing is then attached to the side port of T-connector 2, HiP 15-23AF1. Connected to the top of T-connector 2 is Valve 1 which connects to a syringe pump, ISCO 500D, to charge the system with carbon dioxide and opens the system to the atmosphere when pressure is being reduced. The side port of T-connector 2 leads back to the blowout plug to complete the loop.

Redesigned Apparatus

The redesigned apparatus (Figure 5.5) also has two temperature zones, but the cold zone is located above the hot zone. The water heater and the heater/chiller are the same as in the initial apparatus. The fittings in the loop are connected with 1/8" O.D. stainless steel tubing. Going clockwise around the loop, there is a Swagelok T-connector with a blowout plug attached to the top port. Connected to the bottom port of the T-connector is the microreactor which contains the backed bed of unprocessed solute. Tubing connected to the bottom of the microreactor exits the cold zone and is attached to the precipitation chamber. Tubing out of the side port of the precipitation chamber is connected to a stainless steel elbow which directs the loop upward. Tubing from the elbow is connected to a 4-way cross at the top of the loop. Attached to the cross is a

111

pressure gauge and a valve which is used to add and remove carbon dioxide. Also another piece of tubing connects the 4-way cross to the T-connector to complete the loop. It should be noted that there is no capillary tubing in this apparatus. Instead at the top of the precipitation chamber there is a screw with a 1 mm bore.

Procedure for Operating the Thermosyphon

The thermosyphon apparatus is prepared for operation by loading a solute into the microreactor and placing a clean collector in the precipitation chamber. The microreactor is removed from the loop, and the solute is secured inside the microreactor using wire mesh. The precipitation chamber is also removed from the system. A glass plate such as a microscope slide or similar collection apparatus is placed on the bottom of the precipitation chamber. The microreactor and precipitation chamber are then placed back in the loop.

The apparatus temperature zones are created and maintained, and then carbon dioxide is added at the desired pressure. The hot temperature zone is created by filling the "hot" side of the bath with water, turning on the circulating water heater, and setting the heater to maintain the desired temperature. The cold temperature zone is created by filling the "cold" side of the bath with water, turning on the circulating water heater/chiller, and setting the heater/chiller to maintain the desired temperature. These water baths allow for a variable cold temperature zone of 1°C to >100°C and a variable hot temperature zone of room temperature to 100°C. After the temperatures of the water baths and apparatus components have stabilized, an ISCO 500D Syringe Pump is used to charge the system with carbon dioxide by opening Valve 1. When the desired amount of

carbon dioxide has been added to the loop, Valve 1 is closed, and the syringe pump is detached. It is assumed that the carbon dioxide in the loop varies in temperature around the loop and thus circulates. The system is allowed to operate for several hours.

To end the process, carbon dioxide is slowly removed from the system by partially opening Valve 1. When the system has reached atmospheric conditions, the heater and chiller are turned off, and water is removed from both sides of the bath. The unprocessed and processed solute is collected by removing the microreactor and precipitation chamber. The collected solute is weighed to determine the amount which was dissolved and removed. The processed solute is characterized using an optical or scanning electron microscope.

Pressure Drop and Flow Calculations

The flow rate and temperature profiles within the loop were estimated to evaluate the physical design and operating conditions of the loop. The pressure drop was calculated around the loop assuming a constant flow rate. Since the system is a loop the pressure was constrained such that the starting and ending pressure were the overall system pressure. The following equation was used to estimate the pressure drop as

$$P_2 = P_1 - \left[g\rho(\Delta z) + Q^2 \frac{\rho}{A^2} \left[\frac{L}{4D} \left(\log \frac{5.74}{Q^{0.9} \left(\frac{D\rho}{A\mu} \right)^{0.9}} \right)^{-2} + \Sigma K \right] \right] \quad (5.1)$$

where P_i is the pressure, i represents a positions in the thermosyphon loop, Δz is the height change in each section, Q is the volumetric flow rate, D is the pipe diameter, L is the length of each section, K accounts for friction due to fittings, and the log term

113

accounts for friction from the pipe walls (Bird et al. 1960). The mass flow rate of the system is assumed to be constant. By comparing the friction contributions, the effect of the apparatus configuration on the flow rate was evaluated. The temperature of CO_2 throughout the loop was assumed to be that of the temperature zone.

Results and Discussion

There were several experiments performed to evaluate the feasibility of the thermosyphon process. The conditions for operating the thermosyphon were based on the saturation concentration of naphthalene in carbon dioxide (Figure 5.4). The cross-over pressure of naphthalene in supercritical carbon dioxide is ~ 110 bars. At ~80 bar the difference between the solubilities of naphthalene in carbon dioxide at 50°C and 31°C is near a maximum while remaining a supercritical system (McHugh and Krukonis 1994). Based on these values, naphthalene was processed at an operating pressure of 84 bar, cold zone temperatures of 32°C to 34°C, and hot zone temperatures of 50°C to 45°C (Table 5.1).

Run 1 and 2 (Table 5.1) were performed in the initial apparatus (Figure 5.3) at 84 bar, a hot temperature of 50°C, and a cold temperature of 32°C. In run 1, the tip of the capillary tubing was visualized (Figure 5.6). In Figure 5.6, a droplet is observed to be hanging from the nozzle used in the proposed process. After the initial carbon dioxide loading, a droplet was observed to gradually grow from what appeared to be liquid drops exiting the nozzle. After roughly twenty minutes the droplet was observed to fall off the nozzle. Another droplet then grew at the same position on the tip of the nozzle and fell after a similar amount of time. These droplets left a lump of naphthalene on the bottom

of the precipitation chamber. In run 2 the capillary tubing was removed from the system in an attempt to increase the fluid flow rate to reduce friction, and the same operating temperature and pressure as run 1 were used. Naphthalene was observed to collect on the window of the precipitation chamber. The precipitated solid was collected and characterized via a light microscope (Figure 5.7). The run was ended when it was apparent that the tubing leading into the precipitation chamber was clogged with naphthalene. These experiments provided definitive evidence that naphthalene was being transferred from the cold zone to the hot zone during the proposed process.

Runs 1 and 2 suggested that the flow rate needed to be increased and precipitation needed to be prevented prior to the precipitation chamber. To improve the system, the friction of the loop was reduced to increase the flow rate while keeping the volume of the system small. Pressure drop calculations were performed on the system to estimate the friction effects of the design. The pressure drop calculations and runs 1 and 2 suggested minimizing the overall length of the nozzle, minimizing the length of nozzle in the hot zone, and increasing the nozzle interior diameter would greatly improve the performance of the thermosyphon.

After evaluating the initial apparatus, a revised thermosyphon experimental setup (Figure 5.5) was constructed. The cold zone was relocated to be on top of the precipitation chamber. The capillary tubing was removed and a bored-through stainless steel screw was installing in its place. This setup was tested in run 3 (Table 5.1) at 84 bar and a hot zone temperature of 45°C and a cold zone temperature of 34°C. There was no visual evidence of flow (droplet formation) as in the first setup. After the run a small amount of naphthalene was present on the bottom of the chamber (Figure 5.8). When the

115

tubing between the hot and cold zone was removed, it was observed to be clogged with naphthalene. This clogging indicates that the naphthalene was dissolved by the carbon dioxide, but the fluid heated up before reaching the precipitation chamber.

Conclusion and Future Work

These experiments have demonstrated that supercritical carbon dioxide can be used as a processing medium in a closed loop thermosyphon. Moderate temperature changes generated sufficient buoyant forces to induce fluid flow. By operating below the crossover pressure naphthalene was dissolved in the cold zone and precipitated in the hot zone. This study demonstrates that the supercritical thermosyphon precipitation process is feasible, but there are several areas of future research. The system needs to be altered to prevent naphthalene from precipitating before entering the precipitation chamber and clogging the nozzle. To prevent precipitation of naphthalene before the precipitation chamber, it is suggested that a short, nonconducting nozzle be installed in the system to prevent the fluid from warming up due to an increasing wall temperature. The hot and cold water segregation needs to be improved. Finally, the pressure drop calculations can be extended to include thermal gradients to better understand the fluid flow and CO_2 solvent strength throughout the system.

Tables

Run			1	2	3
Apparatus			Initial	Initial	Revised
Date			04/21/06	06/06/06	08/01/06
Hot Zone	Temperature	°C	50	50	45
		K	323	323	318
	CO_2 Density	g/cm^3	0.24	0.24	0.27
	Approximate Naphthalene Concentration	Wt%	0.1	0.1	0.2
Cold Zone	Temperature	°C	32	32	34
		K	305	305	307
	CO_2 Density	g/cm^3	0.68	0.68	0.63
	Approximate Naphthalene Concentration	Wt%	2	2	2
	CO_2 Density Difference	g/cm^3	0.44	0.44	0.36

Table 5.1 Operating conditions used for performing the thermosyphon precipitation

process at a pressure of 84 bar (1200 psig).

Figures

The box in the figure contains:

$$T_{Hot} > T_{Cold}$$

$$\rho_{Hot} < \rho_{Cold}$$

$$P_{Hot} = P_{Cold}$$

$$^{E}x_{hot} < {}^{E}x_{cold}$$
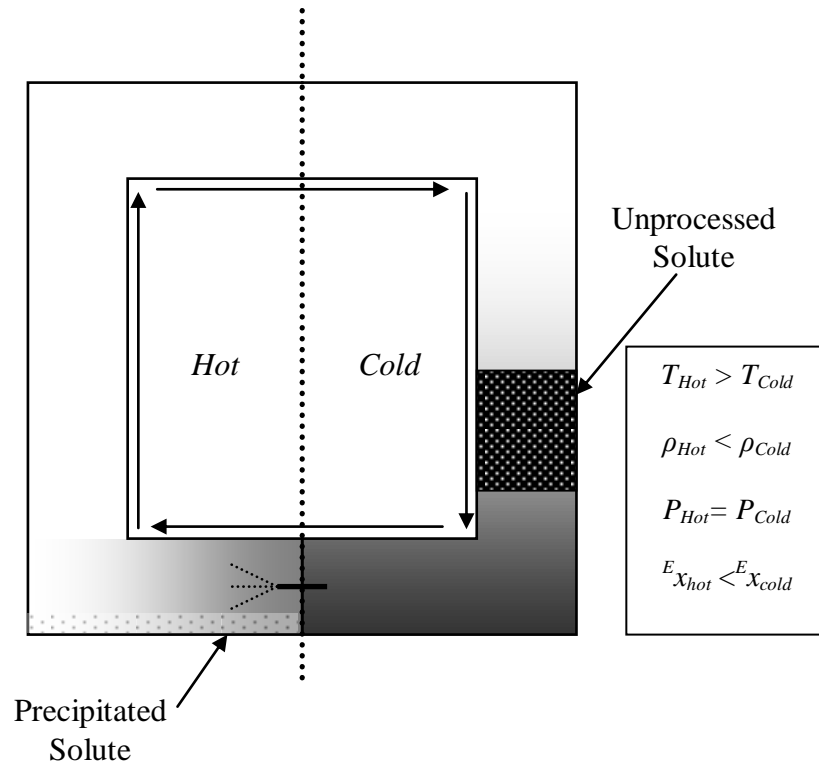
Figure 5.1 Cartoon showing the operation of the thermosyphon precipitation process.

The shading represents the concentration of the solute in solution. The equilibrium solute

concentrations at the hot and cold temperatures are represented by $^{E}x_{hot}$ and $^{E}x_{cold}$.
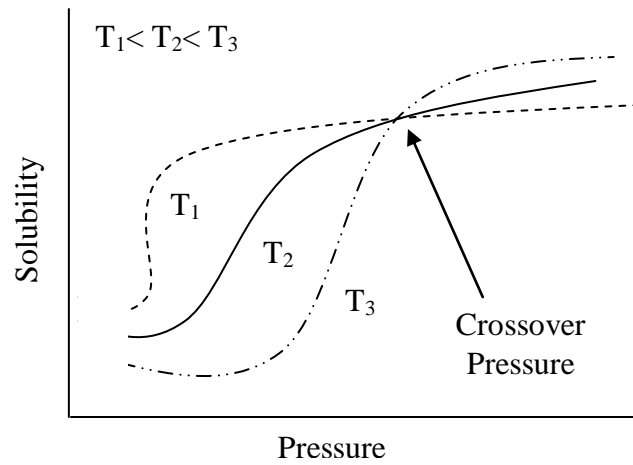
Figure 5.2 Cartoon demonstrating the effect of pressure and temperature on solubility. Below the crossover pressure solubility decreases with temperature. Conversely, above the crossover pressure the solubility increases with temperature (adapted from Mukhopadhyay 2000).
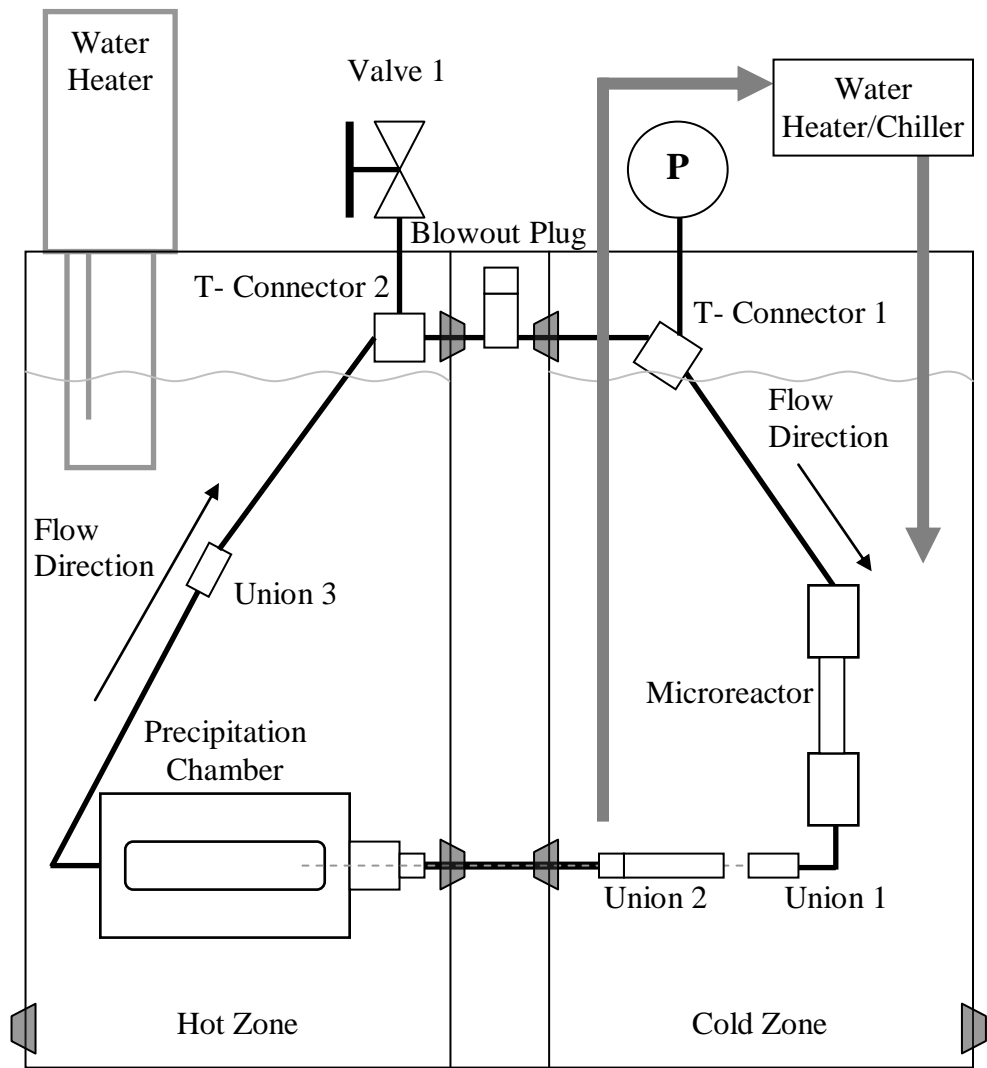
Figure 5.3 A diagram of the initial configuration of the thermosyphon

precipitation process system.
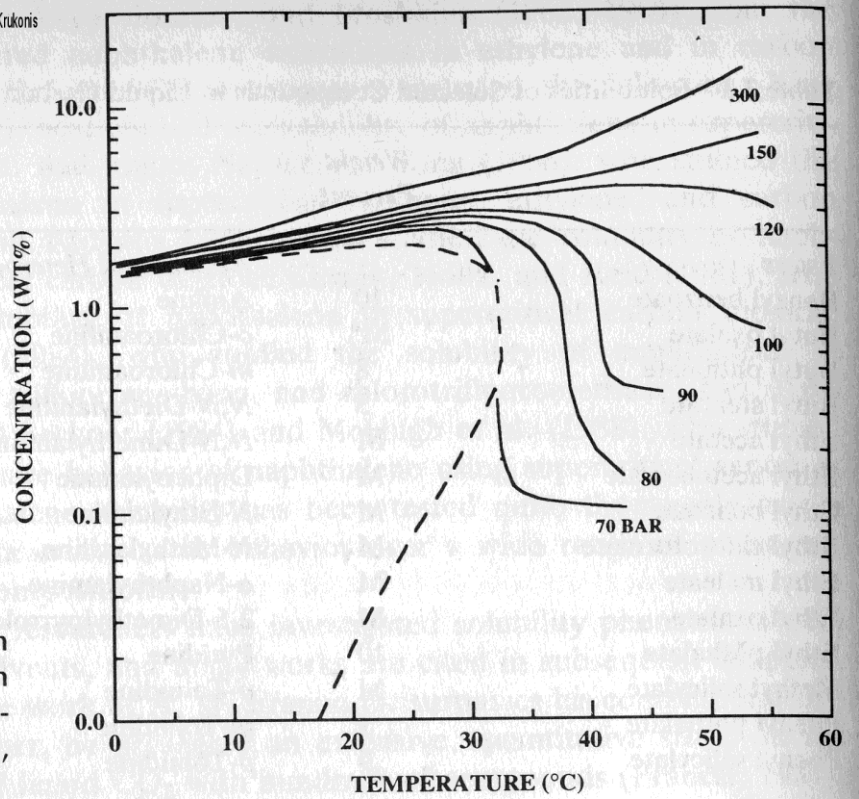
Figure 2.2 Solubility of solid naphthalene in supercritical carbon dioxide (data assembled by Modell et al., 1979).

Figure 5.4 Solubility of naphthalene in carbon dioxide (McHugh and Krukonis 1994).

121
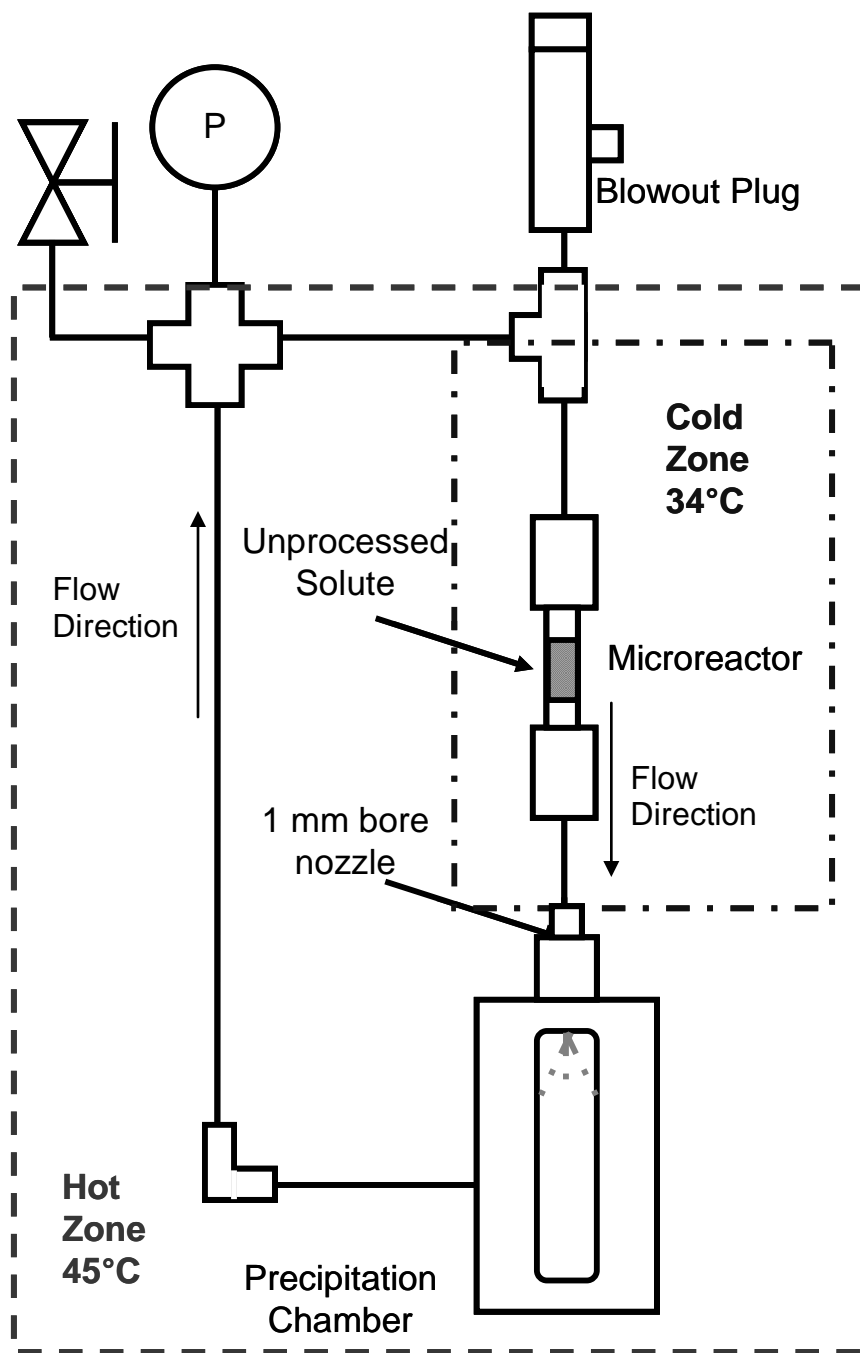
Figure 5.5 A diagram of the redesigned thermosyphon precipitation process system.
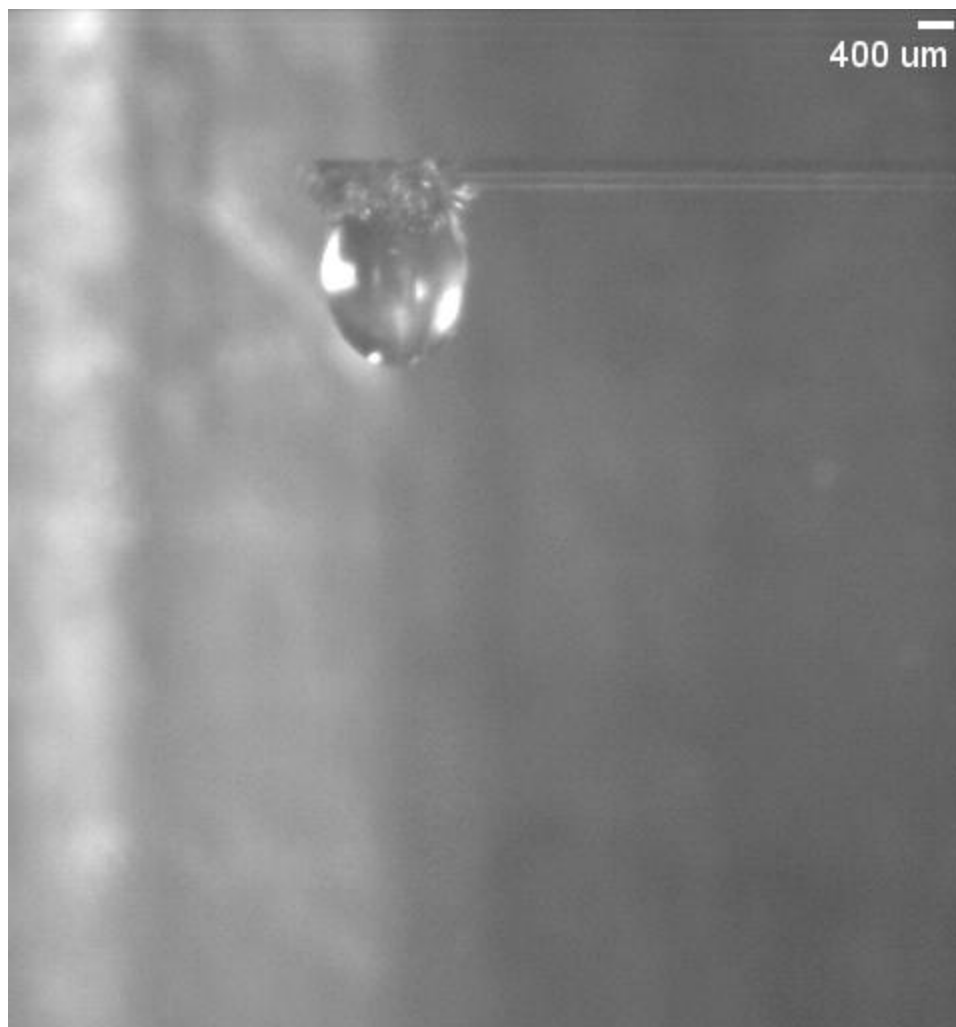
Figure 5.6 Visualization of naphthalene/carbon dioxide mixture collecting on the exit of

capillary tubing nozzle during run 1 which was performed in the initial configuration.
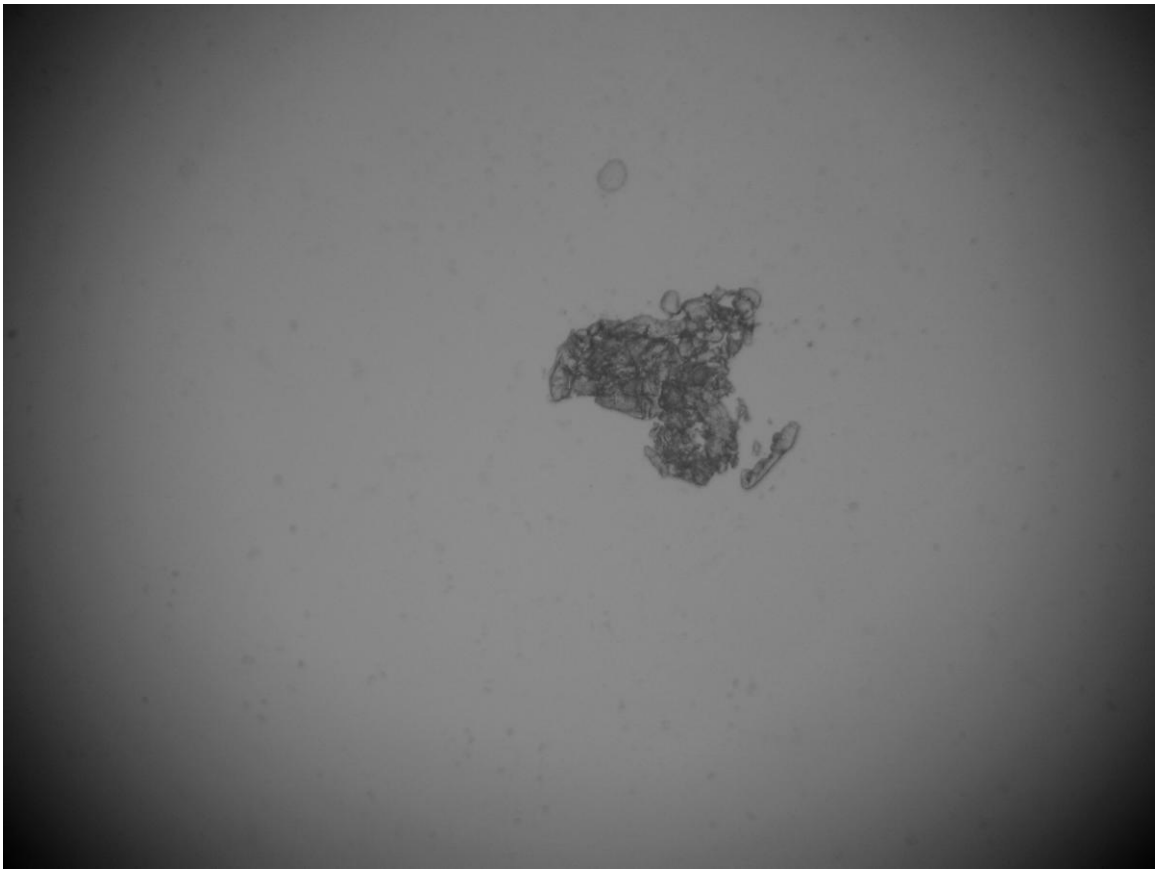
Figure 5.7 Microscope image of naphthalene particles that collected inside the

precipitation chamber during run 2 which was performed in the initial configuration.

Figure 5.8 Microscope image of naphthalene particles that collected inside the

precipitation chamber during run 3 which was performed in the redesigned configuration.

6. Conclusion and Recommendations

Studies were performed to probe the underlying phenomena of the supercritical antisolvent (SAS) precipitation process. By changing the SAS precipitation process operating conditions (temperature and pressure), it is possible to change the spray characteristics. To study the link between spray characteristics and the resulting particles, a high magnification visualization setup was used to image the spray of solution into supercritical carbon dioxide at several pressure and temperature combinations. The effect of the affinity of the solute for the solvent on the SAS precipitation process was tested by processing several polymers with different solubilities. Also, a new particle precipitation process which utilizes the effect of temperature on the density of supercritical fluids was developed.

A high magnification visualization system was used to characterize the spray of a 1 wt% poly(L-lactic) acid in methylene chloride solution into supercritical carbon dioxide at various pressure, temperature, and density combinations. The spray of a solution into supercritical carbon dioxide was characterized by visualizing the spray at various distances from the nozzle outlet to measure jet break up lengths and droplet diameters. The jet break up was observed to occur as atomization into droplets or break up as a gas-like plume depending on the operating conditions. When the jet atomized into droplets, the average droplet diameter increased then decreased with distance from the nozzle outlet. A series of experiments performed at a fixed supercritical CO_2 density of 0.33 $g/cm^3 \pm 2\%$ at various pressure and temperature combinations produced radically

different spray characteristics at a solution flow rate of 0.9 cm^3/min. Atomization was observed at 84 bar, 313 K and 89 bar, 318 K; jet break up as a gas-like plume was observed at 94 bar, 323 K. Despite differences in the jet break up regime, similar size distributions of microparticles, 0.5-2.5 μm, were obtained when SAS was used to process poly(L-lactic) acid at a fixed supercritical CO$_2$ density of 0.33 g/cm^3 ± 2%. A series of experiments on the SAS precipitation process was also performed at a fixed temperature of 323 K at various pressure and density combinations and a solution flow rate of 1.6 cm^3/min. At 84 bar, 0.241 g/cm^3 and 89 bar, 0.278 g/cm^3 atomization was observed, and a gas-like plume was observed at 94 bar, 0.323 g/cm^3. When the atomization of the jet occurred during experiments with a fixed temperature, similar average droplet diameters with different droplet densities were observed at distances near the nozzle outlet. Poly(L-lactic) acid particles processed using SAS at 89 bar, 0.278 g/cm^3 and 94 bar, 0.323 g/cm^3 had a similar particle diameter range, 0.2-2.2 μm, while a larger particle size range, 0.1-5.5 μm, was produced when processing poly(L-lactic) acid at 84 bar, 0.241 g/cm^3. In both the fixed supercritical CO$_2$ density and fixed temperature experiments, the transition from atomization to break up as a gas-like plume coincided with a decrease of the jet break up length and a decrease in the distance from the nozzle outlet at which droplets dissipate. Despite the very different spray characteristics, poly(L-lactic) acid particles obtained from both jet break up regimes had a similar size and morphology.

To study the effect of the solute/organic solvent affinity on the SAS precipitation process, polymer solutes with different solubilities in a chosen solvent were processed in SAS experiments. Copolymers of methyl methacrylate and vinyl pyrrolidone were synthesized at several monomer ratios. Ethanol was chosen as the organic solvent since

it readily dissolves polyvinyl pyrrolidone while polymethyl methacrylate is slightly soluble in ethanol. The SAS precipitation process was performed using polyvinyl pyrrolidone, polymethyl methacrylate, and poly(methyl methacrylate-vinyl pyrrolidone) as solutes at 50°C and pressures of 84 bar, 94 bar, 101 bar, 104 bar, and 111 bar. Cloud point experiments demonstrated that the affinity of the polymer for ethanol decreased with increased methyl methacrylate content for polyvinyl pyrrolidone and poly(methyl methacrylate-vinyl pyrrolidone). Visualizations of the SAS precipitation process that were performed with polymer/ethanol solutions demonstrated that the spray characteristics were solute independent. SAS processing of methyl methacrylate resulted in only small particles, 0.1-5.7 μm. A bimodal particle size distribution was obtained when processing polyvinyl pyrrolidone and poly(methyl methacrylate-vinyl pyrrolidone) at operating conditions near the transition from jet break up by atomization to break up as a gas-like plume. Two particle modes were identified: a small mode with particle from 0.2-6.5 μm and a large mode with particles from 6.5-300 μm. Particles in the large mode, diameters greater than 6.5 μm, were often microballoons. Poly(methyl methacrylate-vinyl pyrrolidone) formed microballoons at lower pressures and in higher concentrations than polyvinyl pyrrolidone. When analyzing the small mode, minimum average particle diameters for both polyvinyl pyrrolidone and poly(methyl methacrylate-vinyl pyrrolidone) were observed to occur at 101 bar. Distinctly different polymer particle characteristics were obtained at different conditions near the mixture critical point. By changing the affinity between the polymer solute and the organic solvent, the tendency to form microballoons was altered.

A new method to form microparticles was developed which used buoyancy driven flow and tunable solvent strength of supercritical fluids. Fluid flow of a supercritical fluid can be induced by heating one portion and cooling another. The cold, dense portion will flow down while the hot, less dense portion will flow up. If the supercritical fluid is inside a loop, a continuous flow of fluid may be induced with distinct density sections. This loop can then be used to dissolve and precipitate a solute because the saturation concentration of the solute is dependent on temperature and pressure. The saturation concentration of a solute in a supercritical fluid is higher at a cold temperature than at a hot temperature when operating below the crossover pressure, the point at which this relation is reversed. The proposed process consists of a two temperature zone loop loaded with a packed bed of solute in the cold zone and filled with a supercritical fluid. The supercritical fluid dissolves the solute in the cold section. The supercritical fluid and solute are transported to the hot zone by buoyant flow; in the hot zone the solute precipitates. The supercritical fluid is then transported back to the cold zone by buoyant flow. To test this process, supercritical carbon dioxide was used as the working fluid inside a closed loop thermosyphon. A packed bed of naphthalene was placed in the cold section of the loop. Constant heating and cooling in different portions of the loop induced two distinct density zones of carbon dioxide which allowed for buoyancy driven flow. The naphthalene was dissolved in the cold zone then transported to the hot zone where it precipitated. The feasibility of this process was demonstrated and future development is encouraged.

There are two recommendations for future work on the SAS precipitation process of which a detailed description can be found in Appendix A. To further understand the

mass transfer of the SAS precipitation process, concentration fields in the precipitation chamber need to be obtained. One method to obtain the concentration field in the precipitation chamber involves planar laser-induced fluorescence (PLIF). Planar laser-induced fluorescence is performed by exciting molecules using a plane of light and imaging the resulting fluorescent emission (Valeur 2002). The fluorescent emission can then be recorded using a visualization setup. By performing the SAS precipitation process with a fluorescent molecule as the solute, the *in situ* concentration field of the molecule could be imaged using PLIF and the previously described high magnification visualization setup (Obrzut et al. 2007). By comparing the fluorescent data at various process conditions, particle characteristics and mass transfer properties can be related.

Another recommended future study involves theoretical modeling of the SAS precipitation process. There have been several models of the SAS precipitation process. These models have typically attempted to model the mass transfer in the process. There also has been some work on the relative time scale of mass transfer and nucleation. While there have been several attempts to date there is no model which accurately predicts the final particle size. I suggest that a model be developed that incorporates the nucleation and growth of particles as well as mass transfer. Understanding the effect of mass transfer, supersaturation, and nucleation on the resulting particle size will assist in scale up of the SAS precipitation process to an industrial scale.

In this research, the SAS precipitation process was studied using high magnification visualization of the spray of solution into a supercritical fluid. At conditions above the mixture critical point the jet break up regime was observed to have little effect on the resulting particles. The affinity of the solute for the solvent was shown

130

to have little effect on the spray characteristics. Solutes with lower affinity for the solvent tended to form more microballoons at subcritical conditions near the mixture critical point. Also, the feasibility of a supercritical precipitation process in a thermosyphon loop was demonstrated. These studies have furthered the understanding of the underlying phenomena which control supercritical precipitation processes.

7. Works Cited

R. Adami, E. Reverchon, E. Järvenpää, R. Huopalahti, Supercritical antisolvent micronization of nalmefene HCl on laboratory and pilot scale, Powder Technology 182 (2008) 105–112.

D. Arcos, M.V. Cabañas, C.V. Ragel, M. Vallet-Regí, J. San Román, Ibuprofen release from hydrophilic ceramic-polymer composites, Biomaterials 18 (1997) 1235-1242.

A.F.M. Barton, CRC handbook of polymer-liquid interaction parameters and solubility parameters, 1990, CRC Press, Boca Raton.

A.F.M. Barton, CRC handbook of solubility parameters and other cohesion parameters, 1991, CRC Press, Boca Raton.

J. Brandrup, E.H. Immergut, E.A. Grulke, Polymer Handbook Volume 1, Wiley-Interscience (1999) 4th edition, Hoboken NJ.

E.J. Beckman, Supercritical and near-critical CO_2 in green chemical synthesis and processing, The Journal of Supercritical Fluids 28 (2004) 121-191.

P.W. Bell, A.P. Stephens, C.B. Roberts, S.R. Duke, High-resolution imaging of the supercritical antisolvent process, Experiments in Fluids 38 (2005) 708-719.

R.B. Bird, W.E. Stewart, E.N. Lightfoot, Transport Phenomena, 1960, Wiley, New York.

J. Bleich, P. Kleinebudde, B. W. Müller, Influence of gas density and pressure on microparticles produced with the ASES process, International Journal of Pharmaceutics 106 (1994) 77-84.

S. Bristow, T. Shekunov, B.Yu. Shekunov, P. York, Analysis of the supersaturation and precipitation process with supercritical CO2, The Journal of Supercritical Fluids 21 (2001) 257-271.

E. Carretier, E. Badens, P. Guichardon, O. Boutin, G. Charbit, Hydrodynamics of supercritical antisolvent precipitation: Characterization and influence on particle morphology, Industrial & Engineering Chemistry Research 42 (2003) 331-338.

A.A. Chang, D. Larobina, R.G. Carbonell, Influence of supersaturation and growth on particle size and morphology in high pressure CO_2 antisolvent process, AICHE Annual Meeting (2005).

F. Chávez, P.G. Debenedetti, J.J. Luo, R.N. Dave, R. Pfeffer, Estimation of the characteristic time scales in the supercritical antisolvent process, Industrial & Engineering Chemistry Research 42 (2003) 3156-3162.

V. Chatoorgoon, Stability of supercritical fluid flow in a single-channel natural-convection loop, International Journal of Heat and Mass Transfer 44 (2001) 1963-1972.

P. Chattopadhyay, R.B. Gupta, Supercritical CO_2-based production of fullerene nanoparticles, Industrial & Engineering Chemistry Research 39 (2000) 2281-2289.

P. Chattopadhyay, R.B. Gupta, Production of griseofulvin nanoparticles using supercritical CO_2 antisolvent with enhanced mass transfer, International Journal of Pharmaceutics 228 (2001) 19-31.

R.C. Chu, R.E. Simons, G.M. Chrysler, Experimental investigation of an enhanced thermosyphon heat loop for cooling of a high performance electronics module, Fifteenth IEEE SEMi-THERM Symposium (1999) 1-9.

P.G. Debenedetti, Metastable Liquids: Concepts and Principles, 1996, Princeton University Press, Princeton NJ.

I. De Marco, E. Reverchon, Supercritical antisolvent micronization of cyclodextrins, Powder Technology 183 (2008) 239–246.

I. Diamond, J. Jeffries, Beginning Statistics, 2001, SAGE Publications, Thousand Oaks, CA.

D.J. Dixon, K.P. Johnston, R.A. Bodmeier, Polymeric materials formed by precipitation with a compressed fluid antisolvent, AIChE Journal 39 (1993) 127-139.

D.J. Dixon, G. Luna-Barcenas, K.P. Johnston, Microcellular microspheres and microballoons by precipitation with a vapor-liquid compressed fluid antisolvent, Polymer 35 (1994) 3998-4005.

S.S. Dukhin, C. Zhu, R. Dave, R. Pfeffer, J.J. Luo, F. Chavez, Y. Shen, Dynamic interfacial tension near critical point of a solvent-antisolvent mixture and laminar jet stabilization, Colloids and Surfaces A: Physicochemical and Engineering Aspects 229 (2003) 181-199.

S.S. Dukhin, Y. Shen, R. Dave, R. Pfeffer, Droplet mass transfer, intradroplet nucleation and submicron particle production in two-phase flow of solvent-supercritical, Colloids and Surfaces A: Physicochemical and Engineering Aspects 261 (2005) 163-176.

S.O. Enibe, Thermal analysis of a natural circulation solar air heater with phase change material energy storage, Renewable Energy 28 (2003) 2269-2299.

A. Gokhale, B. Khusid, R.N. Dave, R. Pfeffer, Effect of solvent strength and operating pressure on the formation of submicrometer polymer particles in supercritical microjets, The Journal of Supercritical Fluids 43 (2007) 341-356.

A.T. Griffith, Y. Park, C.B. Roberts, Separation and recovery of nylon from carpet waste using a supercritical fluid antisolvent technique, Polymer-Plastics Technology and Engineering 38 (1999) 411-431.

M. Hanna, P. York, Patent WO 95/01221 (1994)

W. Hayduk, B.S. Minhas, Correlations for prediction of molecular diffusivities in liquids, The Canadian Journal of Chemical Engineering 60 (1982) 295-299.

Y. Ho Kim, K.S. Shing, Supercritical fluid-micronized ipratropium bromide for pulmonary drug delivery, Powder Technology 182 (2008) 25–32.

Y. Ho Kim, C. Sioutas, P. Fine, K.S. Shing, Effect of albumin on physical characteristics of drug particles produced by supercritical fluid technology, Powder Technology 182 (2008) 354–363.

G.A. Hughmark, Liquid-liquid spray column drop size, holdup and continuous phase mass transfer, Industrial & Engineering Chemistry Fundamentals 6 (1967) 408-413.

P.G. Jessop, B. Subramaniam, Gas-Expanded Liquids, Chem. Rev. 107 (2007) 2666.

C.G. Kalogiannis, C.G. Panayiotou, Bubble and cloud points of the system poly(L-lactic acid) + carbon dioxide + dichloromethane, Journal of Chemical and Engineering Data 50 (2005) 1442-1447.

A.W. Kerst, B. Judat, E.U. Schlünder, Flow regimes of free jets and falling films at high ambient pressure, Chemical Engineering Science 55 (2000) 4189-4208.

I. Kikic, M. Lora, A. Bertucco, A thermodynamic analysis of three-phase equilibria in binary and ternary systems for applications in rapid expansion of a supercritical solution (RESS), particles from gas-saturated solutions (PGSS), and supercritical antisolvent (SAS), Industrial & Engineering Chemistry Research 36 (1997) 5507-5515.

J.L. Koenig, Spectroscopy of Polymers, 1992, American Chemical Society, Washington D.C.

M.J. Lazzaroni, D. Bush, R. Jones, J.P. Hallett, C.L. Liotta, C.A. Eckert, High-pressure phase equilibria of some carbon dioxide-organic-water systems, Fluid Phase Equilibria 224 (2004) 143-154.

B.C. Lee, Y.M. Kuk, Phase behavior of poly(L-lactide) in supercritical mixtures of dichloromethane and carbon dioxide, Journal of Chemical & Engineering Data 47 (2002) 367-370.

E.W. Lemmon, M.O. McLinden, D.G. Friend, NIST Chemistry WebBook, NIST Standard Reference Database Number 69, Eds. P.J. Linstrom and W.G. Mallard, June 2005, National Institute of Standards and Technology, Gaithersburg MD, 20899 (http://webbook.nist.gov).

C.S. Lengsfeld, J.P. Delplanque, V.H. Barocas, T.W. Randolph, Mechanism governing microparticle morphology during precipitation by a compressed antisolvent: atomization vs nucleation and growth, The Journal of Physical Chemistry B 104 (2000) 2725-2735.

S.P. Lin, R.D. Reitz, Drop and spray formation from a liquid jet, Annual Review of Fluid Mechanics 30 (1998) 85-105.

G.G. Liversidge, K.C. Cundy, Particle size reduction for improvement of oral bioavailability of hydrophobic drugs: I. Absolute oral bioavailability of nanocrystalline danazol in beagle dogs, International Journal of Pharmaceutics 125 (1995) 91-97.

G.S.H. Lock, The tubular thermosyphon: variations on a theme, 1992, Oxford University Press, Oxford.

M. Lora, A. Bertucco, I. Kikic, Simulation of the semicontinuous supercritical antisolvent recrystallization process, Industrial & Engineering Chemistry Research 39 (2000) 1487-1496.

M. Maiani, W.J.M. de Kruijf, W. Ambrosini, An analytical model for the determination of stability boundaries in a natural circulation single-phase thermosyphon loop, International Journal of Heat and Fluid Flow 24 (2003) 853-863.

Y. Marcus, Are solubility parameters relevant to supercritical fluids?, The Journal of Supercritical Fluids 38 (2006) 7-12.

T.M. Martin, A.A. Lateef, C.B. Roberts, Measurements and modeling of cloud point behavior for polypropyle / n-pentane and polypropyle / n-pentane / carbon dioxide mixtures at high pressure, Fluid Phase Equilibria 154 (1999) 241-259.

T.M. Martin, N. Bandi, R. Shulz, C.B. Roberts, U.B. Kompella, Preparation of budesonide and budesonide-PLA microparticles using supercritical fluid precipitation technology, AAPS PharmSciTech 3 (2002).

A. Martín, M.J. Cocero, Numerical modeling of jet hydrodynamics, mass transfer, and crystallization kinetics in the supercritical antisolvent (SAS) process, The Journal of Supercritical Fluids 32 (2004) 203-219.

D.W. Matson, J.L. Fulton, R.C. Petersen, R.D. Smith, Rapid expansion of supercritical fluid solutions: solute formation of powders, thin films, and fibers, Industrial & Engineering Chemistry Research 26 (1987) 2298-2306.

S. Mawson, S. Kanakia, K.P. Johnston, Coaxial nozzle for control of particle morphology in precipitation with a compressed fluid antisolvent, Journal of Applied Polymer Science 64 (1997) 2105-2118.

M.A. McHugh, V.J. Krukonis, Supercritical Fluid Extraction: Principles and Practices, 1994, Butterworth-Heinemann, Boston.

A.W. Monfort, D.L. Obrzut, S.R. Duke, Characterization of pressure effects on fluid flow and particle production in the supercritical antisolvent precipitation process: pressure effects on poly(vinylpyrrolidone) precipitation in SCF carbon dioxide, NSF REU report, Auburn University, 2006.

S.K. Mousavian, M. Misale, F.D'Auria, M.A. Salehi, Transient and stability analysis in single-phase natural circulation, Annals of Nuclear Energy 31 (2004) 1177-1198.

M. Mukhopadhyay, Natural extracts using supercritical carbon dioxide, 2000, CRC Press, Boca Raton, FL.

M. Mukhopadhyay, S.V. Dalvi, Mass and heat transfer analysis of SAS: effects of thermodynamic states and flow rates on droplet size, The Journal of Supercritical Fluids 30 (2004) 333-348.

J.W. Mullin, Crystallization, 2004, Elsevier Butterworth-Heinemann, Burlington, MA.

D.L. Obrzut, P.W. Bell, C.B. Roberts, S.R. Duke, Effect of process conditions on the spray characteristics of a PLA+methylene chloride solution in the supercritical Antisolvent Precipitation Process, The Journal of Supercritical Fluids 42 (2007) 299-309.

W.v. Ohnesorge, Die bildung von tropfen an düsen und die auflösung flüssiger strahlen, Zeitschrift fuer angewandte Mathematik und Mechani 16 (1936) 355-358.

M. Orbay, R. Laible, L. Dulog, Preparation of amide and amine groups containing copolymers of methyl methacrylate and their performance in solid polymer composites, Die Makromolekulare Chemie, 183 (1982) 47-63.

Y. Park, C.W. Curtis, C.B. Roberts, Formation of nylon particles and fibers using precipitation with a compressed antisolvent, Industrial & Engineering Chemistry Research 41 (2002) 1504-1510.

Y. Pérez de Diego, F.E. Wubbolts, P.J. Jansens, Modeling mass transfer in the PCA process using the Maxwell-Stefan approach, The Journal of Supercritical Fluids 37 (2006) 53-62.

O.R. Quayle, The Parachors of organic compounds: An interpretation and catalogue, Chemical Reviews 53 (1953) 439-589.

A.D. Randolph, M.A. Larson, Theory of Particulate Processes: Analysis and Techniques of Continuous Crystallization, 1988, Academic Press, San Diego.

T.W. Randolph, A.D. Randolph, M. Mebes, S. Yeung, Sub-micrometer-sized biodegradable particles of poly(L-lactic acid) via the gas antisolvent spray precipitation process, Biotechnology Progress 9 (1993) 429-435.

M. Rantakylä , M. Jäntti, O. Aaltonen, M. Hurme, The effect of initial drop size on particle size in the supercritical antisolvent precipitation (SAS) technique, The Journal of Supercritical Fluids 24 (2002) 251-263.

N. Rasenack, B.W. Müller, Micron-size drug particles: common and novel micronization techniques, Pharmaceutical Development and Technology 9 (2004) 1-13.

J.T. Reaves, A.T. Griffith, C.B. Roberts, Critical properties of dilute carbon dioxide +entrainer and ethane + entrainer mixtures, Journal of Chemical & Engineering Data 43 (1998) 683-686.

R.C. Reid, J.M. Prausnitz, B.E. Poling, The Properties of Gases and Liquids, 1988, McGraw-Hill, New York.

E. Reverchon. R. Adami, Nanomaterials and supercritical fluids, The Journal of Supercritical Fluids 37 (2006) 1-22.

E. Reverchon, I. De Marco, G. Della Porta, Rifampicin microparticles production by supercritical antisolvent precipitation, International Journal of Pharmaceutics 243 (2002) 83-91.

E. Reverchon, G. Caputo, I. De Marco, Role of phase behavior and atomization in the supercritical antisolvent precipitation, Industrial & Engineering Chemistry Research 42 (2003) 6406-6414.

S. Roy, S.R. Duke, Visualization of oxygen concentration fields and measurement of concentration gradients at bubble surfaces in surfactant-contaminated water, Experiments in Fluids, 36 (2004) 654-662.

J.M. Seitzman, R.K. Hanson, Instrumentation for Flows with Combustion, Instrumentation for Flows with Combustion, Ed. AMKP Taylor, 1993, Academic Press, London.

B.Y. Shekunov, J. Baldyga, P. York, Particle formation by mixing with supercritical antisolvent at high Reynolds numbers, Chemical Engineering Science 56 (2001) 2421-2433.

R. Sih, N.R. Foster, Visualization and conception of the atomized rapid injection for solvent extraction (ARISE) process for the production of highly respirable powders, AICHE Annual Meeting (2007).

P.J. Sinko, Martin's Physical Pharmacy and Pharmaceutical Sciences, 2006, Lippincott, Williams & Wilkins, Baltimore.

A.P. Stephens, Visualization of particle formation processes in supercritical fluids, MS Thesis, Auburn University, 2003.

M. Stievano, N. Elvassore, High-pressure density and vapor-liquid equilibrium for the binary systems carbon dioxide-ethanol, carbon dioxide-acetone and carbon dioxide-dichloromethane, The Journal of Supercritical Fluids 33 (2005) 7-14.

B.P. Sullivan, Effect of pressure on a PMMA-ethanol supercritical antisolvent process, Undergraduate Honors Thesis, Auburn University, 2007.

Y. Sun, B.Y. Shekunov, P. York, Refractive index of supercritical CO2-ethanol solvents, Chemical Engineering Communications 190 (2003) 1-14.

R. Thakur, R.B. Gupta, Rapid expansion of supercritical solution with solid cosolvent (RESS-SC) process: Formation of griseofulvin nanoparticles, Industrial & Engineering Chemistry Research 44 (2005) 7380-7387.

R. Thiering, F. Dehghani, A. Dillow, N.R Foster, Solvent effects on the controlled dense gas precipitation of model proteins, Journal of Chemical Technology and Biotechnology 75 (2000) 42-53.

I. Tsivintzelis, D. Missopolinou, K. Kalogiannis, C. Panayiotou, Phase compositions and saturated densities for the binary systems of carbon dioxide with ethanol and dichloromethane, Fluid Phase Equilibria 224 (2004) 89-96.

B. Valeur, Molecular Fluorescence: Principles and Applications, 2002, Wiley-VCH, Weinheim.

M. van der Kraan, M.M.W. Peeters, M.V. Fernandez Cid, G.F. Woerlee, W.J.T. Veugelers, G.J. Witkamp, The influence of variable physical properties and buoyancy on

heat exchanger design for near- and supercritical conditions, The Journal of Supercritical Fluids 34 (2005) 99-105.

A. Vega-González, P. Subra-Paternault, A.M. López-Periago, C.A. García-González, C. Domingo, Supercritical CO_2 antisolvent precipitation of polymer networks of L-PLA, PMMA and PMMA/PCL blends for biomedical applications, European Polymer Journal 44 (2008) 1081–1094.

A. Vignes, Diffusion in binary solutions: variation of diffusion coefficient with composition, Industrial & Engineering Chemistry Fundamentals 5 (1966) 189-199.

A. Weber, L.V. Yelash, T. Kraskac, Effect of the phase behavior of the solvent-antisolvent systems on the gas-antisolvent-crystallization of paracetamol, The Journal of Supercritical Fluids 33 (2005) 107-113.

J.O. Werling, P.G. Debenedetti, Thermal analysis of a natural circulation solar air heater with phase change material energy storage, The Journal of Supercritical Fluids 16 (1999) 167-181.

J.O. Werling, P.G. Debenedetti, Numerical modeling of mass transfer in the supercritical antisolvent process: miscible conditions, The Journal of Supercritical Fluids 20 (2000) 11-24.

P.T. Woodrow, S.R. Duke, LIF measurements of oxygen concentration gradients along flat and wavy air-water interfaces, Industrial & Engineering Chemistry Research 40 (2001) 1985-1995.

H-T. Wu, M-J. Lee, H-m. Lin, Nano-particles formation for pigment red 177 via a continuous supercritical anti-solvent process, The Journal of Supercritical Fluids 33 (2005) 173-182.

F.E. Wubbolts, O.S.L. Bruinsma, G.M. van Rosmalen, Dry-spraying of ascorbic acid or acetaminophen solutions with supercritical carbon dioxide, Journal of Crystal Growth 198/199 (1999) 767-772.

L. Yeng Lee, C. Hwa Wang, K.A. Smith, Supercritical antisolvent production of biodegradable micro- and nanoparticles for controlled delivery of paclitaxel, Journal of Controlled Release 125 (2008) 96–106.

S. Yeo, E. Kiran, Formation of polymer particles with supercritical fluids: A review, The Journal of Supercritical Fluids 34 (2005) 287-308.

S. Yeo, G. Lim, P.G. Debenedetti, H. Bernstein, Formation of microparticulate protein powders using a supercritical fluid antisolvent, Biotechnology and Bioengineering 41 (1993) 341-346.

S. Yoshikawa, R.L. Smith Jr., H. Inomata, Y. Matsumura, K. Arai, Performance of a natural convection circulation system for supercritical fluids, The Journal of Supercritical Fluids 36 (2005) 70-80.

Y. Zvirin, A review of natural circulation loops in pressurized water reactors and other systems, Nuclear Engineering and Design 67 (1981) 203-225.

Appendix A - Future Work

Planar Laser-Induced Fluorescence

Introduction

Nucleation and precipitation of a solute from a solution occurs due to supersaturation of the solute (Randolph and Larson 1988). In the SAS precipitation process, supersaturation is caused by counter diffusion of a supercritical antisolvent and an organic solvent (Werling and Debenedetti 1999). In subcritical systems, this diffusion has been shown to result in the growth and gradual dissipation of droplets as distance from the nozzle outlet is increased (Obrzut et al. 2007). In supercritical systems, a gas-like plume was shown to be present instead of droplets. To further understand the diffusion in the SAS precipitation process, the concentration of species throughout the spray needs to be characterized. Planar laser-induced fluorescence can be used to characterize the concentration of individual species throughout the precipitation chamber.

Planar laser-induced fluorescence (PLIF) is performed by exciting molecules using a plane of light and imaging the resulting fluorescent emission. To form the plane, laser light at a uniform wavelength is sent through several lenses. A spherical lens is used to focus the laser into a narrow waist. A cylindrical lens spreads the point source into a triangular plane. If necessary another cylindrical lens can be used to stop the spread of the triangle and form a plane of light with parallel edges (Seitzman and Hanson 1993). This plane of light intersects the fluid to be fluoresced. The light excites electrons occupying π orbitals of the fluorescent molecule. Fluorescence occurs when the electrons

return to the ground state and release energy at a higher wavelength (Valeur 2002). A detector, such as a CCD camera, is focused on the plane of light to record the fluorescence. The intensity of the fluorescence can then be related to the concentration of the fluorescing species.

Utilizing PLIF with a fluorescent solute to study the SAS precipitation process would allow for the solute concentration profile in the spray to be characterized. A PLIF system similar to that of Roy and Duke (2004) and Woodrow and Duke (2001) could be developed and constructed to image inside a high pressure chamber. Previously demonstrated high-magnification imaging techniques in combination with PLIF would allow for the fluorescence from small portions of the spray to be recorded. Low magnification imaging could be used to obtain the overall fluorescent emission. By comparing the fluorescent data at various process conditions, particle characteristics and mass transfer properties can be related.

Experimental

SAS Apparatus

The SAS setup for these experiments could be the similar to that presented in Obrzut et al. (2007) with modifications. The main modification would be to allow a plane of light to be introduced parallel to the imaging windows. This necessary alteration could be made in one of two ways: modifying the current SAS system or purchasing a new high pressure vessel. To obtain a parallel window, a 1 cm diameter circular window could be placed on the side of the precipitation chamber. The circular window would be positioned 5 cm below the top of the main windows and centered on the wall

perpendicular to the main windows. The location of the nozzle outlet relative to the top

of the main windows could be altered to change the distance from the nozzle at which the

spray is visible through the circular window. Moving the nozzle outlet could be achieved

by maintaining the same length of capillary tubing but altering the amount of 1/8" S.S.

tubing it is threaded through outside of the vessel. For example, six lengths of S.S.

tubing could be used to obtain distances from the nozzle lengths which are visible

through the circular window of 0, 3, 7, 14, 24, and 34 mm.

Visualization

To induce fluorescence of the solute, a nitrogen laser, Photon Technology

International GL-3300, could be used as an ultraviolet light source. The nitrogen laser

produces light at 337.1 nm with a maximum average power of 56 mW and a maximum

energy pulse of 2.8 mJ. The laser could be focused using a spherical lens. The focused

beam would then be flattened using a cylindrical lens positioned between the chopper and

the precipitation chamber. The sheet of light would be oriented parallel to the main

windows of the precipitation chamber. This setup would allow a fluoresced plane of light

to be visible through the main windows of the precipitation chamber. The visual

detection setup of this system could also be the same as that used in Obrzut et al. (2007).

Materials

Poly[methylmethacrylate-co-(7-(4-trifluoromethyl)coumarin methacrylamide)]

(Aldrich #56624-1) (Figure A.1) has a maximum absorbance of 339 nm. The spectrum

(Figure A.2) shows that there is significant absorbance by the polymer at 337.1 nm, so

the Photon Technology International GL-3300 nitrogen laser could be used to fluoresce the copolymer.

<u>Expectations</u>

Standard solutions could be used to obtain the relationship between fluorescence intensity and solute concentration. The fluorescent intensity of these standards are expected to directly correlate to the fluorescent intensities obtained while performing SAS. At 0 mm and 3 mm from the nozzle outlet, the solute is expected to be evenly dispersed within the jet and droplets with a solute concentration lower than the original solution. As the distance from the nozzle outlet is increased the solute is expected to become more evenly distributed. Upon precipitation, the fluorescent emission should no longer be continuous. The obtained concentration profile should provide visual evidence as to where the particles precipitate during the SAS precipitation process.

Modeling the SAS Precipitation Process

There have been several models of the SAS precipitation process which are described in detail in Appendix C. These models have typically been used to understand the mass transfer in the process. There also has been some work on the relative time scales of mass transfer and nucleation processes. While there have been several reported modeling attempts, to this point there is no model which accurately predicts the final particle size from the SAS precipitation process.

To further the understanding of the SAS precipitation process, two phenomenon need to be modeled: mass transfer and nucleation. The concentration profiles and the

mixture critical point of the solvent and antisolvent solutions need to be identified. The supersaturation point of the solute must be determined. The rate of nucleation and growth of the solute must be estimated, and a point at which growth ceases must be determined. By simultaneously calculating the concentration profile and the nucleation rate, the size of particles produced in the SAS precipitation process could be estimated.

First, it is necessary to understand the flow profile. This could either be calculated as carbon dioxide entering a droplet under subcritical conditions or as carbon dioxide entering a cone of fluid under supercritical conditions. For supercritical conditions diffusion could be modeled as mass transfer between the high solvent concentration cone and the bulk fluid. This behavior could be modeled as a cylinder which is gradually increasing in diameter as carbon dioxide diffuses into the system. For subcritical flow, the mass transfer model developed by Mukhopadhyay and Dalvi (2004) is suggested since it uses a core-shell model of the droplet (Figure A.3). This model is suggested since assuming the core of the droplet is at a uniform concentration would simplify modeling the nucleation in the system.

The model developed by Mukhopadhyay and Dalvi (2004) was presented in detail in Appendix C of this dissertation but the main points of this model will be presented here. The mass transfer of CO_2 into the droplet was represented by

$$N_{CO2} = k_L * (C_{CO2,L,i} - C_{CO2,L}) \qquad (A.1)$$

where N_{CO2} is the moles of CO_2 entering the droplet, k_L is the mass transfer coefficient, $C_{CO2,L,i}$ is the concentration of CO_2 at the interface of the liquid droplet, and $C_{CO2,L}$ is the concentration of CO_2 in the bulk of the liquid droplet. The mass transfer coefficient was estimated using penetration theory as

$$k_L = \sqrt{\frac{4 * D_L}{\pi * t_c}} \tag{A.2}$$

where D_L is the diffusivity of CO_2 in the droplet and t_C is the contact time which can be related to the velocity of the droplet. Similarly the mass transfer of solvent into the bulk fluid was represented by

$$N_S = k_G * (C_{S,G,i} - C_{S,G}) \tag{A.3}$$

where N_S is the moles of solvent entering the bulk gaseous phase, k_G is the mass transfer coefficient, $C_{S,G,i}$ is the concentration of solvent at the interface of the bulk gaseous phase, and $C_{S,G}$ is the concentration of solvent in the bulk gaseous phase. The mass transfer coefficient was estimated using the Hughmark equation. The speed of the droplet is necessary to calculate the mass transfer coefficients and was represented by balancing the forces on the droplet

$$F_{Tot} = F_{Gravity} - F_{Buoyancy} - F_{Drag} . \tag{A.4}$$

The size of the droplet also is necessary to estimate the mass transfer coefficients and was calculated using number of moles which are in the droplet at a given period of time and an equation of state to estimate the density of the droplet. Using this model it is possible to estimate the carbon dioxide concentration in droplets.

Once the solvent/antisolvent concentration profile is obtained, the phase behavior of the system could be determined. Using an appropriate equation of state, the mixture supercritical point at the calculated solvent/antisolvent mole fractions could estimated. The supersaturation of the solute could also be determining once the solvent/antisolvent concentration profile is known. Supersaturation can be defined in several ways including

$$S = \frac{c}{c^*} \tag{A.5}$$

154

where S is supersaturation, c is the concentration of solute, and c^* is the saturated

concentration of solute. The concentration of solute could be determined by assuming

that the solute stays in the dense phase and does not enter the bulk fluids. Also it could

be assumed that the solute is evenly dispersed in the dense phase and solute concentration

is only affected by the volume change as the solution moves away from the nozzle until

nucleation begins. The supersaturation can be determined either through empirical or

theoretical data. Cloud point experiments could be used to determine the concentration at

a specified temperature and pressure that the solute precipitated. Solubility parameters

could be used to obtain a rough estimate of the supersaturation.

When the system has been identified as supersaturated, the nucleation and growth

of particles can be calculated. The critical nucleus radius could be estimated using

$$r_c = \frac{2*\sigma*\upsilon}{k*T*\ln(S)} \tag{A.6}$$

where σ is the surface tension, v is the molecular volume, k is the Boltzmann constant,

and r is the particle radius (Mullin 2004). The critical nucleus radius could then be used

to calculate the nucleation rate as suggested by Chavez et al. (2003) using

$$J_o = \omega^* * Z * N(n^*) \tag{A.7}$$

where w^* is the frequency which molecules attach to a nucleus of critical size, Z is the

Zeldovich nonequilibrium factor, and $N(n^*)$ is the equilibrium concentration of critical

nuclei. The growth of the nucleus, moles added per time, could then be calculated using

$$\frac{dM}{dt} = K_G A * (c - c^*)^g \tag{A.8}$$

where K_G is an overall growth coefficient, A is the surface area of a particle, and g is an

empirical value (Mullin 2004). The point at which growth of the particle ceases could be

related to a very high concentration of carbon dioxide or a very low concentration of solute.

Calculating the solvent/antisolvent concentration profile in conjunction with the nucleation rate would provide insight into particle formation during the supercritical antisolvent precipitation process. Specifically it may provide some insight into whether nucleation occurs in a droplet or in the bulk fluid when operating at a temperature and pressure slightly above the mixture critical point. The connection between the saturation point and particle size could also be studied. Studying these factors would assist with scale up of the SAS precipitation process.

Figures
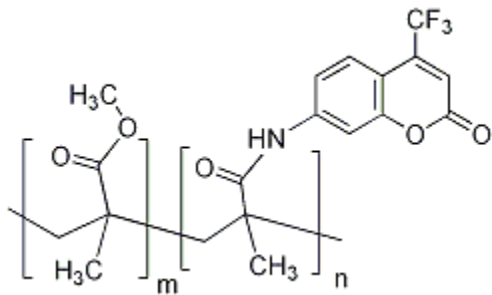
Figure A.1 Chemical structure of the fluorescent copolymer poly[methylmethacrylate-co-

(7-(4-trifluoromethyl)coumarin methacrylamide)].
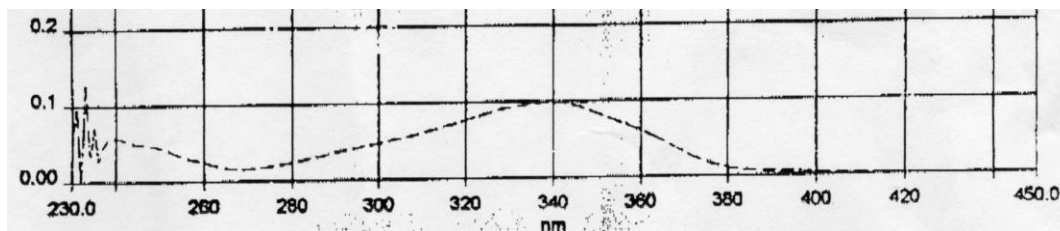
Figure A.2 Absorbance spectrum of poly[methylmethacrylate-co-(7-(4-

trifluoromethyl)coumarin methacrylamide)] supplied by Sigma-Aldrich.
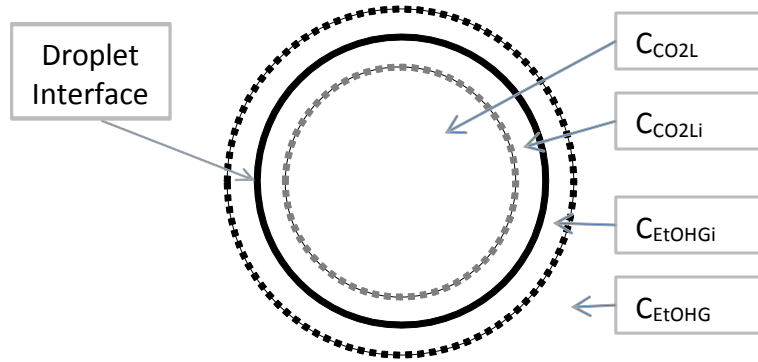
Figure A.3 Cartoon detailing a core-shell droplet where C_{CO2L} is the concentration of CO_2 in the bulk of the liquid droplet, C_{CO2Li} is the concentration of CO_2 at the interface of the liquid droplet, C_{EtOHGi} is the concentration of solvent at the interface of the bulk gaseous phase, and C_{EtOHG} is the concentration of solvent in the bulk gaseous phase.

Appendix B – Supplemental Studies Pertaining to Chapter 4

Solubility Parameters

The miscibility of a polymer and solvent can be predicted by comparing their Hildebrand solubility parameters,

$$\delta = \left(\frac{-U}{V}\right)^{1/2} = c^{1/2} \tag{B.1}$$

where δ is the Hildebrand solubility parameter, U is the molar internal energy, V is the molar volume, and c is the cohesive energy density (Barton 1991). A solute should be soluble in organic solvents with similar solubility parameters, but the solubility parameter is not a definitive indicator of solubility. The solubility parameter of a copolymer can be roughly estimated by assuming that it varies like the solubility parameter of a solution,

$$^{c}\delta = \frac{^{a}\delta\,^{a}\phi + ^{b}\delta\,^{b}\phi}{^{a}\phi + ^{b}\phi} \tag{B.2}$$

where $^{c}\delta$ is the solubility parameter of the copolymer, $^{a}\delta$ is the solubility parameter of component a, $^{b}\delta$ is the solubility parameter of component b, $^{a}\Phi$ is the volume fraction of component a, and $^{b}\Phi$ is the volume fraction of component b (Barton 1991). The volume fractions are directly related to the component ratio by

$$r = \frac{^{a}n}{^{b}n} = \frac{^{a}\phi\,^{b}V}{^{b}\phi\,^{a}V} \tag{B.3}$$

where ^{a}V is the volume per unit of component a, ^{b}V is the volume per unit of component b, ^{a}n is the number of units of component a, ^{b}n is the number of units of component b,

and r is the component ratio. If component a is highly solvent-philic and b is solvent-phobic, increasing the component ratio, r, of the copolymer will increase the solute solubility in an organic solvent with minor changes to the solute.

The polymers discussed in Chapter 4 were chosen based on their solubility parameters relative to ethanol which has a Hildebrand solubility parameter of 26.0 MPa$^{1/2}$ (Barton 1991). For poly(methyl methacrylate) (PMMA) a solubility parameter of 19.0 MPa$^{1/2}$ is suggested. Poly(vinyl pyrrolidone) (PVP) has a suggested solubility parameter near 25 MPa$^{1/2}$ (Barton 1990). From these solubility parameters and experimental results it can be shown that PMMA is just slightly soluble in ethanol while PVP is very soluble in ethanol.

FTIR Data Collection

Transmission Fourier Transform Infrared (FTIR) spectroscopy was performed to characterize the monomer ratio in the synthesized copolymers (Figure B.1). A FTIR sample was prepared by mixing 0.001 g of the polymer with 0.1 g of KBr with a mortar and pestle. This solid mixture was then pressed between two screws in a FTIR cell to form a salt disk. The cell and disk was then placed in a Nicolet Avatar 360 FTIR spectrometer. The spectrometer was purged with nitrogen to remove water vapor. The spectrometer was then started to collect the transmission spectra. Sixty-four scans of wavelengths 400 to 4000 cm^{-1} were performed then averaged to obtain the spectra for the polymers except PMMAVP4 for which 30 scans were performed.

The monomer ratio of the copolymers was estimated by comparing the relative intensity of peaks which are specific for methyl methacrylate to those of vinyl

pyrrolidone using least-squares analysis. This method of analysis was performed by

using the following matrix algebra equations:

$$A=K*C+E \tag{B.4}$$

$$K=A*C'*(inv(C*C')) \tag{B.5}$$

$$C_{copolymer}=inv(K'*K)*K'*A_{copolymer} \tag{B.6}$$

where A is absorbance of the homopolymers, K is the combined path length and

absorptivity, C is concentration of a given component, E is an error term which is

assumed to be 0, $C_{copolymer}$ is the concentration of each monomer in the tested copolymer,

$A_{copolymer}$ is the absorbance from the copolymers, and ' indicates a transposed matrix

(Koenig 1992). The variables in this set of equations represent matrices. A and K are

3736x2 matrices where the two columns represent the homopolymers and the 3736 rows

represent the intensity at each wavelength. C is a 2x2 matrix where the column

represents each polymer and the rows represent the concentration of each monomer in a

sample. Similarly $A_{copolymer}$ and $C_{copolymer}$ are 3736x7 and 2x7 matrices where 7 is the

number of copolymer samples and the 2 columns in $C_{copolymer}$ represent the concentration

of each monomer in the samples.

First in least-squares analysis, K is calculated from the absorbance of the

polyvinyl pyrrolidone and polymethyl methacrylate and the concentration of each

monomer in the homopolymers.

$$K=A*C'*(inv(C*C')) \tag{B.7}$$

C is then a matrix of [(1 0)(0 1)] since each homopolymer contains only one monomer.

This K represents the absorptivity of the individual homopolymers at each wavelength at

a specified concentration. By dividing the spectra of the copolymers, $A_{copolymer}$, by K the

concentration of each monomer is calculated as

$$C_{copolymer}=inv(K'*K)*K'*A_{copolymer}. \qquad (B.8)$$

Since the path length for each salt disk and the overall concentration of polymer is

different in each case, the calculated concentration of the components is a rough

estimation of the monomer content in the copolymers.

The absorbance spectra of the homopolymers and each copolymer were obtained

from 400 to 4000 cm^{-1} (Figure B.1). The ratio of methyl methacrylate groups to vinyl

pyrrolidone was calculated by analyzing portions of the IR spectra through least-squares

analysis. The monomer contribution to the spectra was analyzed over two wavelength

ranges (700 to 1200 cm^{-1}, 1250 to 1400 cm^{-1}) (Table B.1). The calculated monomer

ratios (MMA/VP) are for PMMAVP1 (0.27, 0.65), for PMMAVP3 (0.86, 0.98; 0.58,

0.98) , and for PMMAVP4 (0.80, 0.98; 0.78,1.07) (Table B.1). Thus, PMMAVP3 and

PMMAVP4 contained a significantly larger amount of MMA when compared to

PMMAVP1.

Statistical Analysis of SAS Particle Characteristics

Statistical analysis was performed on the polymer particle data to determine with

what confidence the analyzed particles are representative of the produced particles. A Z-

test was performed to determine the upper and lower range in which one can say that the

average will fall within a percent confidence when there is a known standard deviation.

The Z-test is performed by assigning a Z-score (Z_{score}) based on the percent confidence.

The Z_{score} is then used to calculate the confidence range with the following equation:

$$d_{p\pm} = d_p \pm \left(Z_{score} \frac{\sigma}{\sqrt{n}} \right) \qquad\qquad (B.9)$$

where $d_{p\pm}$ is the upper (+) or lower (-) limit of the confidence interval of the average particle diameter, d_P is the average particle diameter, σ is the standard deviation, and n is number of particles counted (Diamond and Jefferies 2002). A small confidence interval indicates that the analyzed particles are representative of the produced particles.

The Z-test was performed on polymer particle sample data to analyze how representative the sample data is of all particles produced (Table B.2). Since a bimodal distribution was observed at several conditions, the Z-test was performed on three particle size ranges for each sample: the whole sample, particles less than 6.5 μm, and particles equal to or greater than 6.5 μm. The confidence interval when considering the whole sample ranged from 0.04 μm to 1.54 μm. The 95% confidence interval when considering particles below 6.5 μm ranged from 0.04 μm to 0.24 μm. The confidence interval when considering particles equal to or greater than 6.5 μm ranged from 0.36 μm to 20.73 μm. When the confidence intervals are converted into the percent of the average, the confidence intervals for the whole sample range from ±1.02% to ±23.57%, for the particles less than 6.5 μm range from ±1.01% to ±7.72%, and for particles equal to or greater than 6.5 μm range from ±1.92% to ±55.05%.

Table B.2 shows the confidence of each sample set. The confidence intervals for particles below 6.5 μm were below 8% in all cases due to the large number of particles analyzed from each sample. In all cases the confidence interval when considering particles less than 6.5 μm was equal to or less than the coinciding confidence interval when considering all particles. The confidence intervals for particles equal to or greater than 6.5 μm occurred over a wide range due to the limited number of large particles

163

present in some samples and the wide range of particle diameters measured that are above

6.5 μm. Due to this statistical analysis it can be confidently stated that there is a bimodal

distribution when processing PVP and PMMAVP via the SAS precipitation process at

conditions near the transition from a two-phase subcritical system to a one-phase

supercritical system.

Tables and Figures
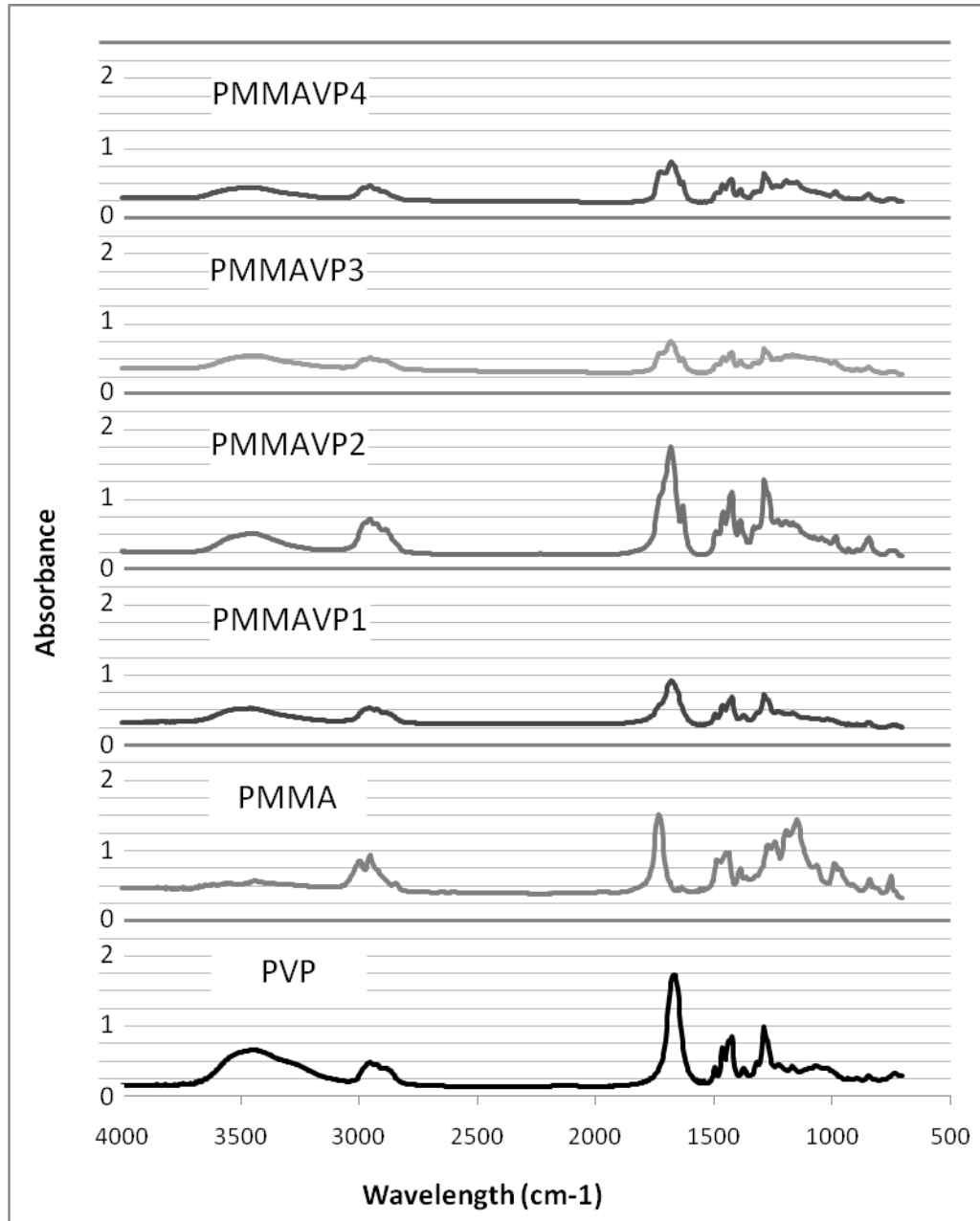
Figure B.1 Plot of the FTIR data obtained for polyvinyl pyrrolidone, poly(methyl methacrylate-vinyl pyrrolidone), and polymethyl methacrylate.

Polymer	700-1200			1250-1400		
	MMA	VP	MMA/VP	MMA	VP	MMA/VP
PMMAVP1	0.18	0.65	0.27	0.29	0.45	0.65
PMMAVP3 A	0.34	0.39	0.86	0.32	0.33	0.98
PMMAVP3 B	0.28	0.48	0.58	0.35	0.36	0.98
PMMAVP4 A	0.30	0.37	0.80	0.35	0.35	0.98
PMMAVP4 B	0.27	0.36	0.78	0.31	0.29	1.07

Table B.1 Molar ratio of methyl methacrylate and vinyl pyrrolidone in synthesized

PMMAVP calculated by least-squares analysis based on FTIR data.

PMMAVP4	PMMAVP4	PMMAVP4	PMMAVP4	PVP	PVP	PVP	PVP	PVP	PMMAVP1	PMMAVP3	Polymer	
84	94	101	111	84	94	101	104	111	84	84	Pressure (bar)	
5.3	1.8	5.8	3.8	0.0	13.2	7.9	0.6	0.4	20.7	3.8	Interval	Above and equal to 6.5 µm
17.7	5.7	30.2	22.2	0.0	55.1	29.6	3.6	1.9	52.3	9.6	Interval in Percent of Average	
17.4	16.4	12.5	10.4	0.0	18.6	17.2	7.9	9.5	30.2	21.7	+ confidence limit	
12.2	14.7	6.7	6.6	0.0	5.4	9.4	7.4	9.1	9.4	17.9	-confidence limit	
14.8	15.5	9.6	8.5	0.0	12.0	13.3	7.7	9.3	19.8	19.8	Average	
22.9	14.6	3.6	2.7	0.0	14.3	7.2	0.4	2.8	24.2	18.6	Stdev	
293	1035	6	8	0	18	13	9	946	21	365	Count	
0.1	0.1	0.2	0.0	0.2	0.2	0.1	0.1	0.1	0.2	0.2	Interval	Below 6.5 µm
2.3	2.2	7.0	1.0	4.2	5.9	7.7	3.1	2.2	5.6	5.5	Interval in Percent of Average	
2.0	1.6	1.2	2.1	2.1	2.1	0.9	2.0	2.5	2.1	1.5	+ confidence limit	
1.9	1.5	1.0	2.1	2.0	1.9	0.8	1.8	2.4	1.9	1.4	-confidence limit	
1.9	1.6	1.1	2.1	2.1	2.0	0.9	1.9	2.5	2.0	1.5	Average	
1.2	1.1	0.7	1.1	0.9	1.2	1.0	1.1	1.6	1.1	1.2	Stdev	
3075	4047	304	9761	427	402	815	1339	3383	359	807	Count	
0.5	0.5	0.3	0.0	0.2	0.7	0.3	0.1	0.2	1.4	1.5	Interval	1 Mode
8.6	5.4	12.6	1.0	4.2	14.6	13.1	3.3	2.6	23.6	10.7	Interval in Percent of Average	
3.3	4.7	1.4	2.1	2.1	2.8	1.2	2.0	4.1	3.7	7.9	+ confidence limit	
2.8	4.2	1.1	2.1	2.0	2.1	0.9	1.9	3.9	2.3	6.4	-confidence limit	
3.1	4.4	1.3	2.1	2.1	2.4	1.0	1.9	4.0	3.0	7.2	average	
7.8	8.7	1.4	1.1	0.9	3.7	2.0	1.2	3.4	7.0	13.4	stdev	
3368	5082	310	9769	427	420	828	1348	4329	380	1172	Count	
293	1035	6	8	0	18	13	9	946	21	365	>= 6.5 µm	Count
494	401	10	1792	63	75	38	186	977	45	86	3 µm to 6.5 µm	
2581	3646	294	7969	364	327	777	1153	2406	314	721	<= 3 µm	
0.2	0.2	0.2	0.2	0.2	0.4	0.1	0.2	0.3	0.6	0.2	min	
241.8	175.0	16.4	14.1	6.3	68.8	31.5	8.3	38.0	95.2	118.0	max	

Table B.2 95% confidence interval of average polymer particle diameter using the Z-test.

Appendix C – Background on Modeling of the SAS Precipitation Process

Several models of the SAS precipitation process have been developed. The goal of these models has been to relate the particle characteristics to the operating parameters. Several studies have concentrated on the rate at which the solvent and carbon dioxide antisolvent diffuse into and out of droplets (Lora et al. 2000, Werling and Debenedetti 1999, Pérez De Diego et al. 2006). The rate of diffusion was also considered for pseudo-droplets at supercritical conditions (Werling and Debenedetti 2000). The heat of evaporation and dissolution effects on the supersaturation was also considered (Mukhopadhyay and Dalvi 2004). To understand the controlling mechanism of SAS the time scales of jet break up, mass transfer, and nucleation have been compared (Chavez et al. 2003). Also, the concentration profile of solvent and solute in the precipitation chamber when SAS is operated at supercritical conditions was calculated in an attempt to relate classical nucleation theory to particles during the SAS precipitation process (Martín and Cocero 2004).

Lora, Bertucco and Kikic Model

One of the earliest models of SAS was developed by Lora, Bertucco, and Kikic (Lora et al. 2000). The mass transfer rates were calculated between a droplet and the bulk fluid and for a full section of the spray. This model assumed that the mass transfer into the droplet was driven by molecular diffusion. Isothermal conditions and equilibrium at the interface were assumed to simplify calculations. Droplets were

assumed to form at the nozzle exit and to be the diameter of the nozzle. The bulk viscosity and density were assumed to be constant and calculated from correlations given in Reid et al. (1988). The droplet properties (e.g. density and diameter) were calculated as carbon dioxide and solvent diffused. Internal mechanical mixing of droplets was assumed to not occur. The system was analyzed in a subcritical regime. These assumptions lead to a simple model which future models improve upon.

The driving force of mass transfer was shown by a thermodynamic model, and the Peng-Robinson equation of state was used to calculate the equilibrium conditions. The solubility of carbon dioxide in the solvent was calculated from the bubble point, and the solubility of the solvent in carbon dioxide was calculated from the dew point. Typically in SAS the solubility of the solvent in carbon dioxide was much lower than the solubility of carbon dioxide in the solvent. The solubility of the solute was neglected when determining the mass transfer of solvent and antisolvent.

Precipitation was determined by the thermodynamic properties of the solute. The solid state fugacity was estimated from a known liquid state and related by the heat of fusion as described by Kikic et al. (1997). The solute was assumed to precipitate when the solid state fugacity was lower than the liquid state fugacity.

To understand how mass transfer affects the droplet diameter an estimation based on density was proposed. The diameter of the droplet was calculated from

$$d = \left(\frac{L * \rho_{Lo}}{L * \rho_L} \right)^{1/3} * d_o \tag{C.1}$$

where subscript O in this equation designates the initial values of the droplet, L is liquid molar flow rate, d is droplet diameter, and ρ_L is the density of fluid within a droplet. The momentum of a droplet was calculated from

$$\frac{dv}{dh} = \frac{\rho_L - \rho_G}{\rho_L} * \frac{g}{u} - \frac{18 * \mu_G}{\rho_L * d^2} \tag{C.2}$$

where h is height, ρ_G is the bulk fluid density, u is the droplet velocity, g is the acceleration due to gravity, and μ_G is the bulk fluid viscosity. The surface area between liquid and the bulk solution was calculated by estimating the number of drops in some incremental height and multiplying by the surface area of one droplet. This can be represented by

$$\frac{dA}{dh} = \pi * d^2 * \left(\frac{6 * L_o}{\pi * \rho_{LO} * d_o^3 * v} \right) \tag{C.3}$$

where A is surface area. These three equations allow for diameter, velocity, and surface area of a droplet to be calculated.

The mass transfer of the process is modeled by the following molar flux equations:

$$N_{AL} = x_A^e (N_{AL} + N_{BL}) - k_L (x_A^e - x_A) = y_A^e (N_{AG} + N_{BG}) - k_G (y_A - y_A^e) = N_{AG} \tag{C.4}$$

$$N_{BL} = x_B^e (N_{AL} + N_{BL}) + k_L (x_B - x_B^e) = y_B^e (N_{AG} + N_{BG}) - k_G (y_B^e - y_B) = N_{BG} \tag{C.5}$$

where N is molar flux, x is mole fraction in the droplet, y is mole fraction in the bulk fluid, and k is the mass transfer coefficient. In these equations subscript B represents solvent, A represents carbon dioxide, L represents the liquid drop, and G represents the bulk fluid. A superscript e represents the equilibrium values which have been calculated from the Peng-Robinson equation of state. These equations provide the basis for calculations of the amount of carbon dioxide and solvent transferring across the phase

170

interface. To calculate the bulk fluid mass transfer coefficient the Hughmark equation (Hughmark 1967) is utilized:

$$Sh = 2 + 0.0187 * \mathrm{Re}^{0.779} * Sc^{0.546} * \left(dg^{0.333} * D_G^{0.667}\right)^{0.116} \tag{C.6}$$

where Sh is the Sherwood number, Re is the Reynolds number, Sc is the Schmidt number, and D_G is the solvent diffusion coefficient in the bulk fluid. The Hughmark equation can be rearranged to give the bulk fluid mass transfer coefficient directly as

$$k_G = \frac{D_G}{d}(2 + 0.00187 * \mathrm{Re}^{0.779} Sc^{0.546}(dg^{0.333}D_G^{-0.667})^{0.116} \tag{C.7}$$

(Mukhopadhyay and Dalvi 2004). The Schmidt number is given as

$$Sc = \frac{\mu_G}{\rho_G D_G}. \tag{C.8}$$

The liquid mass-transfer coefficient, k_L, can be calculated by

$$k_L = \frac{2 * \rho_L * D_L}{d}. \tag{C.9}$$

The diffusion coefficient of antisolvent in the droplet was calculated by averaging the infinite-dilution values using the Vignes method (Vignes 1966).

This model was evaluated by examining a carbon dioxide–toluene system and then analyzing this system at 315.15 K and 83.4 bar with naphthalene and phenanthrene as solutes. At these operating conditions, the carbon dioxide concentrations at equilibrium are

$$x_A = 0.911, \, y_A = 0.990 \tag{C.10}$$

where x_A is inside the droplet and y_A is the bulk liquid. The modeling results show that the carbon dioxide rapidly diffuses into the droplet until nearing equilibrium. The mole fraction is then kept approximately constant as the droplet continues to travel away from

the nozzle. The initial droplet velocity slightly affects the molar liquid flow rate as droplets travel away from the nozzle. As the ratio of gas to liquid initial flow rate is decreased, the moles in the liquid phase are more likely to decrease after the carbon dioxide-solvent equilibrium is neared. Increasing the initial droplet diameter decreases the time needed to reach the equilibrium mole fractions, but smaller drops should decrease the time for supersaturation to be reached when a solute is considered. Also shown is when a solute is added the mole fraction of the droplet needs to reduce below the supersaturation point of the solid. If it does not, the antisolvent will not cause the precipitation of the solute. The time needed for precipitation to occur is linked directly with the amount of antisolvent diffusing across the interface into the droplet by this model, but, as noted in Werling and Debenedetti (1999), this model does not look at internal droplet mass transfer.

Werling and Debenedetti Model

Another key SAS model dealing with mass transfer between the droplets and bulk fluid in subcritical conditions was published by Werling and Debenedetti (1999) and was later extended to miscible conditions (Werling and Debenedetti 2000). A subcritical condition was defined as a pressure above the system critical pressure and a temperature below the system critical temperature but above the bulk fluid critical temperature. This model examined the mass flux between a single droplet of organic solvent and a bulk fluid of carbon dioxide antisolvent. Mixing inside the droplets was assumed to be due to convective motion. This model allowed the droplet size and solvent concentration to be estimated relative to the lifetime of the droplet.

First, the equations for subcritical conditions are presented (Werling and Debenedetti 1999). The model was set up by assuming the flux of carbon dioxide follows Fick's Law and the diffusion coefficient was related to the chemical potential gradient:

$$N_A = -\rho * D' * \nabla x_A + x_A N \tag{C.11}$$

$$D'_L = D_L \left(1 + \left(\frac{d \ln \Phi_A^L}{d \ln x_A}\right)\right) \tag{C.12}$$

$$D'_G = D_G \left(1 + \left(\frac{d \ln \Phi_A^G}{d \ln y_A}\right)\right) \tag{C.13}$$

where N_A is molar flux of antisolvent, D' is the modified diffusion coefficient, N is the total molar flux, D is the diffusion coefficient, Φ is the fugacity coefficient, G represents the gaseous bulk phase, and L represents the liquid droplet. The CO_2 mole fraction inside the droplet was determined from

$$\frac{d}{dt}\left(\rho_L x_A\right) + \nabla \bullet \left(-\rho_L D'_L \nabla x_A + x_A N_L\right) = 0. \tag{C.14}$$

A similar equation was used for the solvent mole fraction outside the drop. The continuity equation

$$\frac{d\rho_L}{dt} + \nabla \bullet N_L = 0 \tag{C.15}$$

was used to calculate the density inside the droplet. Equation C.16 was used to solve for the change of the radius, R, through a molar balance on a droplet:

$$\frac{dR}{dt} = \frac{-1}{R^2 * \rho_L^e} \int_o^R r^2 \frac{d\rho_L}{dt} dr - \frac{\tilde{N}}{\rho_L^e}. \tag{C.16}$$

The interfacial flux, $\tilde{N}$, was represented by

$$\tilde{N} = \left(\frac{\rho_G^e D_G'^e}{x_A^e * y_B^e - 1} \right) \frac{dy_B}{dr} \bigg|_{r=R} + \left(\frac{\rho_L^e D_L'^e}{x_A^e * y_B^e - 1} \right) \frac{dx_A}{dr} \bigg|_{r=R} . \tag{C.17}$$

The interfacial flux calculations use the assumption that the interface is at equilibrium conditions. These equations set up a model which allows the examination of the local concentrations of solvent and antisolvent inside the droplets.

This model was modified for mixture supercritical conditions (Werling and Debenedetti 2000). There is no phase interface, so the mass transfer was defined in one equation. An arbitrary droplet radius was chosen at 33% of the difference between solvent and bulk fluid density. Flux and diffusivity were again defined using

$$N_A = -\rho * D' * \nabla x_A + x_A N \tag{C.18}$$

$$D' = D \left(1 + \left(\frac{d \ln \Phi_A}{d \ln x_A} \right) \right) . \tag{C.19}$$

Note however that the diffusivity does not include subscripts to denote a phase. To define the concentration profile, only the mass balance and continuity equation were necessary:

$$\frac{d}{dt} (\rho x_A) + \nabla \bullet (-\rho D' \nabla x_A + x_A N) = 0 \tag{C.20}$$

$$\frac{d\rho}{dt} + \nabla \bullet N = 0 . \tag{C.21}$$

The Peng-Robinson equation was used to define the nonideal change in density of the droplet. The Vignes method was again used to calculate the local diffusivities of the system during mixing.

The results for the subcritical conditions (Werling and Debenedetti 1999) generally agree with the model by Lora et al. (2000). The carbon dioxide initially

dominates the mass transfer by diffusing into the droplet. The interfacial flux between the droplet and bulk fluid approaches zero when the rate of mass transfer of antisolvent into the droplet approaches the rate of mass transfer of solvent and antisolvent out of the droplet. Then, the rate of mass transfer out of the droplet controls the interfacial flux. Raising the pressure increases the maximum size of the droplet but decreases the time for the droplet to be indistinguishable from the bulk. The maximum lifetime was predicted to be slightly above the mixture critical point. Surprisingly, the droplets which reach saturation the fastest were not predicted to have the shortest lifetimes.

When droplets were far above the mixture critical point there were several different behaviors (Werling and Debenedetti 2000). Droplets shrank when the solvent density was below the bulk fluid density and swelled when the density was greater in the droplet. When there were similar densities, the droplets were undefined. Increasing temperature reduced the lifetime of droplets. When carbon dioxide had a higher initial density, droplet lifetime increased with pressure. Droplet lifetime decreased with pressure when the solvent had the higher initial density. Droplet lifetime also was shorter in supercritical conditions than in subcritical conditions.

Mukhopadhyay and Dalvi Model

Mukhopadhyay and Dalvi introduced a nonisothermal model of the SAS precipitation process (Mukhopadhyay and Dalvi 2004). A droplet was modeled as having a well mixed core surrounded by a film at the phase interface. Mass transfer between the droplet core and the bulk fluid was assumed to occur at the phase interface

which was at equilibrium. Heat transfer into the droplet was assumed to occur from the evaporation of solvent and dissolution of carbon dioxide at the interface.

The model presented by Mukhopadhyay and Dalvi followed a similar logic as previous models. The initial droplet diameter was approximated using Mugele's method which was presented in Wubbolts et al. (1999) as

$$d_o = 5 * d_n \left(\frac{d_n \rho_B^L u_o}{\mu_B^L} \right)^{-0.35} \left(\frac{\mu_B^V u_o}{\sigma_B} \right)^{-0.2} \qquad (C.22)$$

where μ_B^L is the viscosity of the solvent in the droplet, μ_B^V is the viscosity of the solvent in the bulk fluid, and σ_B is the interfacial surface tension. The velocity of the droplet was assumed to be affected by the three forces which act on the droplet (gravity, buoyancy, and drag [shear stress]) by

$$\frac{dh}{dt} = t \left(\frac{g(\rho_L - \rho_G)}{\rho_L} - \frac{3C_D}{4d} \left[\frac{dh}{dt} \right]^2 \frac{\rho_G}{\rho_L} \right) + u_o . \qquad (C.23)$$

C_D is a function of the Reynolds number as

$$C_D = 1.355 - 0.806 \log(\text{Re}) + 0.0817 (\log(\text{Re}))^2 \qquad (C.24)$$

with the Reynolds number being calculated as

$$\text{Re} = \frac{d * u * \rho_L}{\mu_L} . \qquad (C.25)$$

The instantaneous droplet diameter was calculated from the density of the liquid, total moles in the droplet, and the equation for a sphere's volume.

The driving force of carbon dioxide flux was the concentration of carbon dioxide in the core of the droplet compared to the interface concentration at equilibrium as

$$N_A = k_L \left(\rho_L^e * x_A^e - \rho_L * x_A \right). \qquad (C.26)$$

The liquid mass transfer coefficient can be calculated by

$$k_L = \sqrt{\frac{4 * D_L * u}{\pi * d}} \qquad (C.27)$$

which is derived from penetration theory. The mass transfer of solvent to the bulk fluid is estimated from the equilibrium concentration, $\rho_G{}^e y_B{}^e$, and bulk fluid concentration, $\rho_G y_B$ as

$$N_B = k_G \left(\rho_G^e * y_B^e - \rho_G * y_B \right). \qquad (C.28)$$

The gas mass transfer coefficient of solvent in the bulk fluid, k_G, was assumed to be derived from the Hughmark equation (Hughmark 1967) as in Lora et al. (2000).

Heat transfer was incorporated into this model to calculate how temperature changed the supersaturation conditions. The temperature of the droplet was calculated from equating the heat produced by dissolution and evaporation with the heat transfer inside the droplet as

$$Q_h = h_L \left(T_d - T \right) \pi * d^2 = \left(\Delta h_{diss} N_A - \Delta h_{evap} N_B \right) \pi * d^2 * \Delta t \qquad (C.29)$$

where Q_h is the heat flux, h_L is the liquid film heat transfer coefficient, T_d is the bulk temperature of the droplet, Δh_{diss} is the heat of dissolution, and Δh_{evap} is the heat of evaporation. The heat of dissolution and evaporation are simply the change in partial molar enthalpy between the two phases. The heat transfer coefficient was estimated using film theory and the thermal conductivity, K, with

$$h_L = \frac{2K}{d}. \qquad (C.30)$$

This model gives an approximation of how the supersaturation level changes with time due to heat and mass transfer.

There are several conclusions which were drawn in this paper. The proximity to the mixture critical point was the determining factor of the change in droplet diameter, specifically after the initial swelling whether the droplets swell or continue to shrink. Shrinking of the droplet was calculated to occur when the bulk conditions were close to the mixture critical point. Swelling of the droplet was calculated when the flow rate of carbon dioxide was increased. Particle morphology was speculated to depend on the possibility of shrinking or swelling. Shrinking was speculated to result in small, solid particles while swelling was speculated to result in large, hollow particles. The temperature effect of evaporation and dissolution seemed to have a small effect on the droplet shrinking and swelling. The temperature of the droplet initially reduced between 1 and 3 K before stabilizing. This model showed that temperature change due to dissolution and evaporation should be considered when modeling the SAS precipitation process.

Pérez de Diego, Wubbolts, and Jansens Model

Another model to look at SAS was pursued by Pérez de Diego et al. (2006). Mass transfer was modeled using the Maxwell-Stefan equation by a finite-difference approximation instead of diffusion by Fick's Law. The droplets were modeled using a core-shell model with equilibrium at the interface assumed. It was assumed that there was no accumulation of either species in the shell. The driving force, F, of mass transfer for a species, i, was modeled using the difference of chemical potential, μ, over a distance, z, as shown

$$F_i = \frac{d\mu_i}{dz} .$$

(C.31)

Using the Maxwell-Stefan equations this driving force was also equaled to the friction

between species i and j as

$$F_i = \frac{RT}{D_{ij}} x_j \left(u_i - u_j \right) \qquad (C.32)$$

where R is the ideal gas constant, T is the temperature, D_{ij} is the diffusion coefficient, x_j is

the mole fraction of species j, u_i is the velocity of species i, and u_j is the velocity of

species j. Mass transfer coefficient in the liquid phase, k_{ij}^l, was obtained from the

Maxwell-Stefan diffusion coefficients

$$k_{ij}^l = \left(\left(1.13 \sqrt{\frac{D_{ij}^l}{t}} \right)^2 + \left(6.58 \frac{D_{ij}^l}{d} \right)^2 \right) \qquad (C.33)$$

where t is time and d is diameter. The bulk (gas) phase mass transfer coefficient, k_{ij}^g, was

obtained from the Hughmark equation. The velocity of droplets was estimated by

calculating the change in velocity caused by gravity, buoyancy, and drag as in

Mukhopadhyay and Dalvi (2004). The infinite dilution Maxwell-Stefan diffusivities

were estimated from

$$D_{ij,\infty}^l = 1.55*10^{-8} \frac{T^{1.29}\left(\dfrac{P_j^{0.5}}{P_i^{0.5}} \right)}{\mu_j^{0.92} v_j^{0.23}} \qquad (C.34)$$

where P_i is the Parachor parameter of species i, P_j is the Parachor parameter of species j,

and v_j is the velocity of species j (Hayduk and Minhas 1982, Quayle 1953). The infinite

dilution Maxwell-Stefan diffusivities were then combined using the Vignes equation

$$D_{ij}^l = \left(D_{ij,\infty}^l \right)^{x_j} \left(D_{ji,\infty}^l \right)^{x_i}. \qquad (C.35)$$

to calculate the diffusion coefficient. The density of the bulk phase was assumed to be constant as that of the pure carbon dioxide, and the droplet phase density was calculated using the Peng-Robinson equation of state. The numerical calculations were carried out using the Runge-Kutta method.

The solvent and antisolvent examined using the above model was methylene chloride and carbon dioxide. The behavior of droplets was examined for conditions ranging from 40 to 75 bar and 308 K to 328 K. The maximum droplet diameter was estimated to be achieved at 75 bar and 308 K. The mole fraction of carbon dioxide was calculated to rapidly increase until the maximum diameter was reached and then remained approximately constant. The maximum droplet diameter and the time to reach the maximum droplet diameter decreased when either temperature or pressure was increased. The lifetime of droplets was predicted to depend on the temperature or pressure, but the dependence is nonlinear.

Chávez, Debenedetti, Luo, Dave, and Pfeffer Model

Chávez et al. (2003) modeled jet break up, mass transfer, and nucleation to determine the dominant phenomena on the basis of the time scales for each to occur. A subcritical system of carbon dioxide and ethanol was examined using a binary interaction parameter, k_{ij}, of 0.0795. The jet break up length and time were calculated using a method which was previously applied to SAS (Lengsfeld et al. 2000). Parachor parameters were used to calculate the surface tension between the solution and carbon dioxide. The initial droplet diameter was calculated by assuming that a droplet had the same volume as a length of the jet. The jet break up time was calculated for Weber

numbers ranging from 1 to 40 at different temperatures. From these calculations the maximum jet break up time was on the order of 10^{-3}s. The time for diffusion of mass into a droplet was calculated from

$$\tau_D = r^2 / D_{AB} \tag{C.36}$$

where r is droplet radius and D_{AB} is mixture diffusion coefficient. The mixture diffusion coefficient was calculated in the same manner as in the Werling and Debenedetti (1999). Using this model the time for diffusion to occur was two orders of magnitude larger than jet breakup time. Nucleation was modeled using classical nucleation theory. The steady state rate of nucleation, J_o, was represented by

$$J_o = \omega^* * Z * N(n^*) \tag{C.37}$$

where w^* is the frequency which molecules attach to a nucleus of critical size, Z is the Zeldovich nonequilibrium factor, and $N(n^*)$ is the equilibrium concentration of critical nuclei. Before a steady state of nucleation there is an induction time which occurs. The induction time for one critical nucleus to form inside a droplet was calculated using J_o, Z and w^* which results in

$$\tau_I = \frac{16}{\pi} \frac{\sigma_c}{k_B * T (\ln s)^2 C * v * \lambda_o} e^{\Delta U / k_B T} \tag{C.38}$$

where σ_c is surface tension between crystal and fluid, k_B is Boltzmann's constant, ΔU is the desolvation energy, and s is supersaturation. The variables which were seen to have the greatest effect on the induction time were desolvation energy and supersaturation. At low supersaturation and high desolvation energy, the nucleation time was large. However, the diffusion time was typically several orders of magnitude larger than the nucleation time. A diffusion-limited system was predicted to result from a low

desolvation energy, low interfacial tension, and large supersaturation levels. A nucleation-limited system was predicted to result from small droplets, high interfacial tension, high desolvation energy, low solute concentration, and low supersaturation levels.

Martín and Cocero Model

A model looking at the solvent and solute concentration throughout a single phase spray was developed (Martín and Cocero 2004). This model attempted to predict the spray of solution as a gas-like plume instead of droplets to further the understanding of the SAS precipitation process in a supercritical regime. The continuity equation was applied with a variable density. The equation of motion in the radial direction was neglected while the equation of motion in the axial direction was utilized. Since the flow was turbulent, the velocity was time-smoothed using the Launder-Sharma model. The turbulent diffusivity was a factor of the flow and not the species. This allowed density to be constant in the continuity equation while the diffusive flux was assumed to obey Fick's law. The rate of generation and destruction also was present in the continuity equation. The amount of solvent was assumed to be constant while the solute was modeled to leave and enter the fluid through nucleation and condensation. One of the goals of this model was to predict what size particles may form depending on their location in the spray.

The size of particles was modeled as a factor of nucleation, coagulation, and condensation. This method of calculation identified that particle size also was a factor of location within the jet. The interfacial tension between the solute and fluid was predicted

182

to have a large effect on the particle size. A large interfacial tension was shown to result in slower nucleation which allowed for more coagulation and resulted in larger particles. The results from this model suggest that modifying temperature and pressure to induce supersaturation faster will produce smaller particles.

Appendix D – Supplemental Material

Video Name	Carbon Dioxide Conditions				Measured distance from the nozzle	Excel Sheet
	Temperature (K)	Pressure (bar)	Solution Flow Rate (mL/min)	Solution		
06-01-04 L-PLA 1wt%,MC, CO2, 1200psig,40C,0mm,-9sccm.mpg	313	84	0.9	1wt% PLA in methylene chloride	0	isochoric dropletsizes.xls
06-02-04 L-PLA 1wt%,MC, CO2, 1200psig,40C,7mm,-9sccm	313	84	0.9	1wt% PLA in methylene chloride	7	NA
06-02-04 L-PLA 1wt%,MC, CO2, 1200psig,40C,14mm,-9sccm	313	84	0.9	1wt% PLA in methylene chloride	13	NA
06-03-04 L-PLA 1wt%,MC, CO2, 1200psig,40C,24mm,-9sccm	313	84	0.9	1wt% PLA in methylene chloride	23	NA
06-03-04 L-PLA 1wt%,MC, CO2, 1200psig,40C,24mm,-9sccm B	313	84	0.9	1wt% PLA in methylene chloride	23	NA
06-04-04 L-PLA 1wt%,MC, CO2, 1200psig,40C,44mm,-9sccm	313	84	0.9	1wt% PLA in methylene chloride	43	NA
06-09-04 L-PLA 1wt%,MC, CO2, 1277psig,45C,0mm,-9sccm	318	89	0.9	1wt% PLA in methylene chloride	0	isochoric dropletsizes.xls
06-16-04 L-PLA 1wt%,MC, CO2, 1277psig,45C,7mm,-9sccm	318	89	0.9	1wt% PLA in methylene chloride	7	NA
06-16-04 L-PLA 1wt%,MC, CO2, 1277psig,45C,7mm,-9sccm ----	318	89	0.9	1wt% PLA in methylene chloride	7	NA

Table D.1 Videos used as raw data in Chapter 3.

	Carbon Dioxide Conditions					
Video Name	Temperature (K)	Pressure (bar)	Solution Flow Rate (mL/min)	Solution	Measured distance from the nozzle	Excel Sheet
06-17-04 L-PLA 1wt%,MC, CO2, 1277psig,45C,14mm,-9sccm	318	89	0.9	1wt% PLA in methylene chloride	13	NA
06-18-04 L-PLA 1wt%,MC, CO2, 1277psig,45C,24mm,-9sccm	318	89	0.9	1wt% PLA in methylene chloride	23	NA
06-21-04 L-PLA 1wt%,MC, CO2, 1277psig,45C,24mm,-9sccm	318	89	0.9	1wt% PLA in methylene chloride	23	NA
06-22-04 L-PLA 1wt%,MC, CO2, 1277psig,45C,44mm,-9sccm	318	89	0.9	1wt% PLA in methylene chloride	43	NA
06-23-04 L-PLA 1wt%,MC, CO2, 1353psig,50C,0mm,-9sccm	323	94	0.9	1wt% PLA in methylene chloride	0	isochoric dropletsizes.xls
06-23-04 L-PLA 1wt%,MC, CO2, 1353psig,50C,7mm,-9sccm	323	94	0.9	1wt% PLA in methylene chloride	7	NA
06-23-04 L-PLA 1wt%,MC, CO2, 1353psig,50C,14mm,-9sccm	323	94	0.9	1wt% PLA in methylene chloride	13	NA
06-24-04 L-PLA 1wt%,MC, CO2, 1353psig,50C,24mm,-9sccm	323	94	0.9	1wt% PLA in methylene chloride	23	NA
06-28-04 L-PLA 1wt%,MC, CO2, 1353psig,50C,44mm,-9sccm	323	94	0.9	1wt% PLA in methylene chloride	43	NA
06-29-04 L-PLA 1wt%,MC, CO2, 1353psig,50C,7mm,-9sccm	323	94	0.9	1wt% PLA in methylene chloride	7	NA

Table D.2 Videos used as raw data in Chapter 3.

Video Name	Carbon Dioxide Conditions				Measured distance from the nozzle	Excel Sheet
	Temperature (K)	Pressure (bar)	Solution Flow Rate (mL/min)	Solution		
07-11-05 1200psig 50C 1wtpla mc into co2 1-6sccm 44mm	323	84	1.6	1wt% PLA in methylene chloride	44	1200psig 50C.xls
07-12-05 1200psig 50C 1wtpla mc into co2 1-6sccm 44mm	323	84	1.6	1wt% PLA in methylene chloride	44	NA
07-13-05 1200psig 50C 1wtpla mc into co2 1-6sccm 0mm	323	84	1.6	1wt% PLA in methylene chloride	0	1200psig 50C.xls
01-09-05 1353psig 50C 1wtpla mc into co2 0mm	323	94	1.6	1wt% PLA in methylene chloride	0	NA
01-13-05 1353psig 50C 1wtpla mc into co2 3mm	323	94	1.6	1wt% PLA in methylene chloride	3	NA
01-18-05 1353psig 50C 1wtpla mc into co2 14mm	323	94	1.6	1wt% PLA in methylene chloride	14	NA
03-13-05 1277psig 50C 1wt%pla mc 24mm 1-6sccm	323	89	1.6	1wt% PLA in methylene chloride	24	NA
03-17-05 1200psig 50C 1wt%pla mc 0mm 1-6sccm	323	84	1.6	1wt% PLA in methylene chloride	0	1200psig 50C.xls
03-21-05 1200psig 50C 1wt%pla mc 14mm 1-6sccm	323	84	1.6	1wt% PLA in methylene chloride	14	NA
03-22-05 1200psig 50C 1wt%pla mc 14mm 1-6sccm	323	84	1.6	1wt% PLA in methylene chloride	14	1200psig 50C.xls
03-23-05 1200psig 50C 1wt%pla mc 24mm 1-6sccm	323	84	1.6	1wt% PLA in methylene chloride	24	NA
03-24-05 1200psig 50C 1wt%pla mc 3mm 1-6sccm	323	84	1.6	1wt% PLA in methylene chloride	3	1200psig 50C.xls
04-15-05 1353psig 50C 1wtpla mc into co2 1-6sccm 24mm	323	94	1.6	1wt% PLA in methylene chloride	24	NA
04-16-05 1353psig 50C 1wtpla mc into co2 1-6sccm 34mm	323	94	1.6	1wt% PLA in methylene chloride	34	NA
04-17-05 1200psig 50C 1wtpla mc into co2 1-6sccm 34mm	323	84	1.6	1wt% PLA in methylene chloride	34	NA

Table D.3 Videos used as raw data in Chapter 3.

	Carbon Dioxide Conditions					
Video Name	Temperature (K)	Pressure (bar)	Solution Flow Rate (mL/min)	Solution	Measured distance from the nozzle	Excel Sheet
04-20-05 1277psig 50C 1wtpla mc into co2 1-6sccm 34mm	323	89	1.6	1wt% PLA in methylene chloride	34	1277psig 50C.xls
04-23-05 1200psig 50C 1wtpla mc into co2 1-6sccm7mm	323	84	1.6	1wt% PLA in methylene chloride	7	NA
06-03-05 1277psig 50C 1wtpla mc into co2 1-6sccm 7mm	323	89	1.6	1wt% PLA in methylene chloride	7	NA
06-04-05 1200psig 50C 1wtpla mc into co2 1-6sccm 7mm	323	84	1.6	1wt% PLA in methylene chloride	7	NA
06-08-05 1200psig 50C 1wtpla mc into co2 1-6sccm 7mm	323	84	1.6	1wt% PLA in methylene chloride	7	NA
06-09-05 1200psig 50C 1wtpla mc into co2 1-6sccm 14mm	323	84	1.6	1wt% PLA in methylene chloride	14	NA
06-10-05 1353psig 50C 1wtpla mc into co2 1-6sccm 7mm	323	94	1.6	1wt% PLA in methylene chloride	7	NA
06-13-05 1200psig 50C 1wtpla mc into co2 1-6sccm 3mm	323	84	1.6	1wt% PLA in methylene chloride	3	NA
06-14-05 1200psig 50C 1wtpla mc into co2 1-6sccm 34mm	323	84	1.6	1wt% PLA in methylene chloride	34	NA
06-24-05 1200psig 50C 1wtpla mc into co2 1-6sccm 3mm	323	84	1.6	1wt% PLA in methylene chloride	3	NA
11-30-04 1277psig 50C 1wtpla mc into co2 0mm	323	89	1.6	1wt% PLA in methylene chloride	0	NA
12-01-04 1277psig 50C 1wtpla mc into co2 3mm	323	89	1.6	1wt% PLA in methylene chloride	3	NA
12-02-04 1277psig 50C 1wtpla mc into co2 7mm	323	89	1.6	1wt% PLA in methylene chloride	7	NA
12-03-04 1277psig 50C 1wtpla mc into co2 14mm	323	89	1.6	1wt% PLA in methylene chloride	14	NA

Table D.4 Videos used as raw data in Chapter 3.

Video Name	Carbon Dioxide Conditions			Solution	Measured distance from the nozzle	Excel Sheet
	Temperature (K)	Pressure (bar)	Solution Flow Rate (mL/min)			
08-09-06 1200psig 50C 1wt% PVP ethanol into co2 1-6 sccm 3mm	323	84	1.6	1wt% PVP in ethanol	3	polyvinylpyrroli done sizing Droplets.xls
08-10-06 1200psig 50C 1wt% PVP ethanol into co2 1-6 sccm 7mm	323	84	1.6	1wt% PVP in ethanol	7	polyvinylpyrroli done sizing Droplets.xls
08-11-06 1200psig 50C 1wt% PVP ethanol into co2 1-6 sccm 14mm	323	84	1.6	1wt% PVP in ethanol	14	polyvinylpyrroli done sizing Droplets.xls
08-15-06 1200psig 50C 1wt% PVP ethanol into co2 1-6 sccm 44mm	323	84	1.6	1wt% PVP in ethanol	44	polyvinylpyrroli done sizing Droplets.xls
08-16-06 1200psig 50C 1wt% PVP ethanol into co2 1-6 sccm 74mm	323	84	1.6	1wt% PVP in ethanol	74	polyvinylpyrroli done sizing Droplets.xls
08-18-06 1353psig 50C 1wt% PVP ethanol into co2 1-6 sccm 0mm	323	94	1.6	1wt% PVP in ethanol	0	polyvinylpyrroli done sizing Droplets.xls
08-22-06 1353psig 50C 1wt% PVP ethanol into co2 1-6 sccm 3mm	323	94	1.6	1wt% PVP in ethanol	3	polyvinylpyrroli done sizing Droplets.xls
08-23-06 1353psig 50C 1wt% PVP ethanol into co2 1-6 sccm 7mm	323	94	1.6	1wt% PVP in ethanol	7	polyvinylpyrroli done sizing Droplets.xls
10-16-06 1353psig 50C 1wt% PVP ethanol into co2 1-6 sccm 14mm	323	94	1.6	1wt% PVP in ethanol	14	polyvinylpyrroli done sizing Droplets.xls
11-27-07 1600psig 50C 1wt% PVP ethanol into co2 1-6 sccm 0mm.mpg	323	111	1.6	1wt% PVP in ethanol	0	polyvinylpyrroli done sizing Droplets.xls
11-26-07 1600psig 50C 1wt% PVP ethanol into co2 1-6 sccm 0mm.mpg	323	111	1.6	1wt% PVP in ethanol	0	polyvinylpyrroli done sizing Droplets.xls
11-21-07 1500psig 50C 1wt% PVP ethanol into co2 1-6 sccm 0mm.mpg	323	104	1.6	1wt% PVP in ethanol	0	polyvinylpyrroli done sizing Droplets.xls
10-08-07 1500psig 50C 1wt% PVP ethanol into co2 1-6 sccm 0mm.mpg	323	104	1.6	1wt% PVP in ethanol	0	polyvinylpyrroli done sizing Droplets.xls

Table D.5 Videos used as raw data of PVP in Chapter 4.

	Carbon Dioxide Conditions					
Video Name	Temperature (K)	Pressure (bar)	Solution Flow Rate (mL/min)	Solution	Measured distance from the nozzle	Excel Sheet
10-24-06 1200psig 50C 1wt% P(MMA-VP) ethanol into co2 1-6 sccm 0mm	323	84	1.6	1 wt% PMMAVP1 in ethanol	0	PMMAVP1 sizing 1200psig 50C.xls
10-26-06 1200psig 50C 1wt% P(MMA-VP) ethanol into co2 1-6 sccm 3mm	323	84	1.6	1 wt% PMMAVP1 in ethanol	3	PMMAVP1 sizing 1200psig 50C.xls
10-27-06 1200psig 50C 1wt% P(MMA-VP) ethanol into co2 1-6 sccm 7mm	323	84	1.6	1 wt% PMMAVP1 in ethanol	7	PMMAVP1 sizing 1200psig 50C.xls
10-28-06 1200psig 50C 1wt% P(MMA-VP) ethanol into co2 1-6 sccm 14mm	323	84	1.6	1 wt% PMMAVP1 in ethanol	14	PMMAVP1 sizing 1200psig 50C.xls
10-30-06 1200psig 50C 1wt% P(MMA-VP) ethanol into co2 1-6 sccm 44mm	323	84	1.6	1 wt% PMMAVP1 in ethanol	44	PMMAVP1 sizing 1200psig 50C.xls
10-29-06 1200psig 50C 1wt% P(MMA-VP) ethanol into co2 1-6 sccm 74mm	323	84	1.6	1 wt% PMMAVP1 in ethanol	74	PMMAVP1 sizing 1200psig 50C.xls
12-08-06 1353psig 50C 1wt% P(MMA-VP) ethanol into co2 1-6 sccm 0mm	323	94	1.6	1 wt% PMMAVP1 in ethanol	0	PVPMMA1 1353psig 50C.xls
01-09-07 1353psig 50C 1wt% P(MMA-VP) ethanol into co2 1-6 sccm 3mm	323	94	1.6	1 wt% PMMAVP1 in ethanol	3	PVPMMA1 1353psig 50C.xls
01-10-07 1353psig 50C 1wt% P(MMA-VP) ethanol into co2 1-6 sccm 7mm	323	94	1.6	1 wt% PMMAVP1 in ethanol	7	PVPMMA1 1353psig 50C.xls
01-11-07 1353psig 50C 1wt% P(MMA-VP) ethanol into co2 1-6 sccm 14mm	323	94	1.6	1 wt% PMMAVP1 in ethanol	14	PVPMMA1 1353psig 50C.xls
01-17-07 1353psig 50C 1wt% P(MMA-VP) ethanol into co2 1-6 sccm 44mm	323	94	1.6	1 wt% PMMAVP1 in ethanol	44	PVPMMA1 1353psig 50C.xls

Table D.6 Videos used as raw data of PMMAVP1 in Chapter 4.

	Carbon Dioxide Conditions					
Video Name	Temperature (K)	Pressure (bar)	Solution Flow Rate (mL/min)	Solution	Measured distance from the nozzle	Excel Sheet
01-18-07 1353psig 50C 1wt% P(MMA-VP) ethanol into co2 1-6 sccm 74mm	323	94	1.6	1 wt% PMMAVP1 in ethanol	74	PVPMMA1 1353psig 50C.xls
01-22-07 1450psig 50C 1wt% P(MMA-VP) ethanol into co2 1-6 sccm 0mm	323	101	1.6	1 wt% PMMAVP1 in ethanol	0	PVPMMA1 1450psig 50C.xls
01-24-07 1450psig 50C 1wt% P(MMA-VP) ethanol into co2 1-6 sccm 3mm	323	101	1.6	1 wt% PMMAVP1 in ethanol	3	PVPMMA1 1450psig 50C.xls
01-25-07 1450psig 50C 1wt% P(MMA-VP) ethanol into co2 1-6 sccm 14mm	323	101	1.6	1 wt% PMMAVP1 in ethanol	14	PVPMMA1 1450psig 50C.xls
01-26-07 1450psig 50C 1wt% P(MMA-VP) ethanol into co2 1-6 sccm 44mm	323	101	1.6	1 wt% PMMAVP1 in ethanol	44	PVPMMA1 1450psig 50C.xls
02-06-07 1450psig 50C 1wt% P(MMA-VP) ethanol into co2 1-6 sccm 74mm	323	101	1.6	1 wt% PMMAVP1 in ethanol	74	PVPMMA1 1450psig 50C.xls

Table D.7 Videos used as raw data of PMMAVP1 in Chapter 4.

	Carbon Dioxide Conditions					
Video Name	Temperature (K)	Pressure (bar)	Solution Flow Rate (mL/min)	Solution	Measured distance from the nozzle	Excel Sheet
03-15-07 1200psig 50C 1wt% PMMAVP4 ethanol into co2 1-6 sccm 0mm	323	84	1.6	1 wt% PMMAVP4 in ethanol	0	PVPMMA4 1200psig 50C.xls
04-02-07 1200psig 50C 1wt% PMMAVP4 ethanol into co2 1-6 sccm 3mm	323	84	1.6	1 wt% PMMAVP4 in ethanol	3	PVPMMA4 1200psig 50C.xls
04-03-07 1200psig 50C 1wt% PMMAVP4 ethanol into co2 1-6 sccm 14mm	323	84	1.6	1 wt% PMMAVP4 in ethanol	14	PVPMMA4 1200psig 50C.xls
04-04-07 1200psig 50C 1wt% PMMAVP4 ethanol into co2 1-6 sccm 44mm	323	84	1.6	1 wt% PMMAVP4 in ethanol	44	PVPMMA4 1200psig 50C.xls
04-05-07 1200psig 50C 1wt% PMMAVP4 ethanol into co2 1-6 sccm 74mm x	323	84	1.6	1 wt% PMMAVP4 in ethanol	74	PVPMMA4 1200psig 50C.xls
4-24-07 1450psig 50C 1wt% PMMAVP4 ethanol into co2 1-6 sccm 0mm	323	101	1.6	1 wt% PMMAVP4 in ethanol	0	PVPMMA4 1450psig 50C.xls
04-25-07 1450psig 50C 1wt% PMMAVP4 ethanol into co2 1-6 sccm 3mm	323	101	1.6	1 wt% PMMAVP4 in ethanol	3	PVPMMA4 1450psig 50C.xls
04-26-07 1450psig 50C 1wt% PMMAVP4 ethanol into co2 1-6 sccm 14mm	323	101	1.6	1 wt% PMMAVP4 in ethanol	14	PVPMMA4 1450psig 50C.xls
05-04-07 1450psig 50C 1wt% PMMAVP4 ethanol into co2 1-6 sccm 44mm	323	101	1.6	1 wt% PMMAVP4 in ethanol	44	PVPMMA4 1450psig 50C.xls
05-07-07 1450psig 50C 1wt% PMMAVP4 ethanol into co2 1-6 sccm 74mm	323	101	1.6	1 wt% PMMAVP4 in ethanol	74	PVPMMA4 1450psig 50C.xls

Table D.8 Videos used as raw data of PMMAVP4 in Chapter 4.

	Carbon Dioxide Conditions					
Video Name	Temperature (K)	Pressure (bar)	Solution Flow Rate (mL/min)	Solution	Measured distance from the nozzle	Excel Sheet
04-10-07 1353psig 50C 1wt% PMMAVP4 ethanol into co2 1-6 sccm 0mm	323	94	1.6	1 wt% PMMAVP4 in ethanol	0	PVPMMA4 1353psig 50C.xls
04-11-07 1353psig 50C 1wt% PMMAVP4 ethanol into co2 1-6 sccm 3mm	323	94	1.6	1 wt% PMMAVP4 in ethanol	3	PVPMMA4 1353psig 50C.xls
04-17-07 1353psig 50C 1wt% PMMAVP4 ethanol into co2 1-6 sccm 14mm	323	94	1.6	1 wt% PMMAVP4 in ethanol	14	PVPMMA4 1353psig 50C.xls
04-19-07 1353psig 50C 1wt% PMMAVP4 ethanol into co2 1-6 sccm 44mm	323	94	1.6	1 wt% PMMAVP4 in ethanol	44	PVPMMA4 1353psig 50C.xls
04-23-07 1353psig 50C 1wt% PMMAVP4 ethanol into co2 1-6 sccm 74mm	323	94	1.6	1 wt% PMMAVP4 in ethanol	74	PVPMMA4 1353psig 50C.xls
03-28-08 1600psig 50C 1wt% PMMAVP4 ethanol into co2 1-6 sccm 0mm	323	111	1.6	1 wt% PMMAVP4 in ethanol	0	PVPMMA4 1600psig 50C.xls
03-27-08 1600psig 50C 1wt% PMMAVP4 ethanol into co2 1-6 sccm 0mm	323	111	1.6	1 wt% PMMAVP4 in ethanol	0	PVPMMA4 1600psig 50C.xls

Table D.9 Videos used as raw data of PMMAVP4 in Chapter 4.